IMPERIAL COLLEGE LONDON

Advanced Lithium-ion Battery Modelling for Automotive Applications

Marie-Therese von Srbik

A thesis submitted in partial fulfilment for the

degree of Doctor of Philosophy

in the

Faculty of Engineering

Department of Mechanical Engineering

Supervisors:
Professor Ricardo F. Martinez-Botas   Mechanical Engineering
Dr. Gregory J. Offer   Mechanical Engineering

March 2015

Declaration of Originality

I hereby declare that this thesis and the work presented herein is my own work except where appropriately referenced or acknowledged.

Signed: Marie-Therese v. Srbik

Date: 1st August 2015

The contents of this thesis are to remain confidential for a period of two years (until 01/04/2017) unless it is revoked by the author prior to that date.

Abstract

A novel electrical circuit analogy is proposed to model electrochemical systems under realistic automotive operation conditions. The model is developed for a lithium ion battery and is based on a pseudo 2D electrochemical model. It calculates the evolution of species concentration distribution and diffusion for a given current load, as a result of electrochemical reactions. The application example is an automotive system, in which results are obtained at a rate faster than real-time and well within the accuracy requirements of a typical Battery Management System (BMS). This is the first Equivalent Circuit Network (ECN)-type model that tracks directly the evolution of species inside the cell, and includes implementation of complex electrochemical phenomena usually omitted such as double layer capacitance and overpotentials due to mass transport limitations in the electrode host material. Three networks, one for each of the three species present, electrons, Li ions, and intercalated Li atoms, are connected through a triple species element, which governs the conversion between species at the resulting activation, diffusion and passivating layer overpotentials. The link between the three networks is an important feature of this model, coupling information of each of the three joining circuit networks at this node. The model is fully thermally coupled and can account for capacity fade via a decrease in the amount of active species and for power fade via an increase in a resistive solid electrolyte inter-phase layer at both electrodes. The model's capability to simulate cell behaviour under dynamic events from 0% to 100% State-of-Charge (SoC) conditions is demonstrated with various test procedures. Examples for model output are given for various standard battery testing load cycles as well as realistic automotive drive cycle loads. Although cast in the framework familiar to application engineers, the model is essentially an electrochemical battery model: all variables have a direct physical interpretation and there is direct access to all states of the cell via the model variables (species concentrations, potentials) for the later purpose of control systems design. Further model extensions are easily implemented atop the current framework. The presented methodology is further applicable for electrochemical system performance evaluation and prediction of battery performance in any kind of portable battery-powered electronic device and application with low computational power availability and online solution requirements.

Contents

List of Figures

List of Tables

Definitions

Several terms used in describing batteries and electrochemical processes are defined here for the reader's convenience [4].

Energy density: the volumetric energy storage density of a battery, expressed in Watt-hours per litre [$\mathrm{Wh\,L^{-1}}$]

Power density: the volumetric power density of a battery, expressed in Watts per litre [$\mathrm{W\,L^{-1}}$]

Capacity: the total charge that can be obtained from a fully charged battery under specified discharge conditions, expressed in Ampere-hours [Ah]

Specific energy: the gravimetric energy storage density of a battery, expressed in Watt-hours per kilogram [$\mathrm{Wh\,kg^{-1}}$]

Specific power: the gravimetric power density of a battery, expressed in Watt per kilo-gram in [$\mathrm{W\,kg^{-1}}$]

C-rate: the charge or discharge current equal in Amperes to the rated capacity in Ah. For example, the C-rate for a 3Ah cell is 3A, whilst the 3C and C/3-rates are 9 A and 1 A, respectively

Cycle life: the number of cycles that a cell or battery can be charged and discharged before the available capacity in [Ah] falls below specific performance criteria (commonly defined as 80% rated capacity).

Cut-off voltage: the battery voltage at which the discharge is terminated; commonly referred to as End-of-Discharge voltage, expressed in [V]

Self-discharge: the recoverable loss of capacity of a cell or battery, usually expressed as a percentage of rated capacity lost per month at certain storage conditions.

Resistance: a quantity that describes the relationship between battery voltage and current, expressed in Ohms [Ω]

Capacitance: a quantity that describes the relationship between battery voltage and charge, expressed in Ohms [F]

Impedance: a frequency-dependent complex quantity that describes the relationship between battery voltage and current, with the real and imaginary components expressed in Ohms [Ω]

SoC: state-of-charge can be expressed in [%] of the maximum possible charge, for example, 100% reflects a fully-charged battery and 0% reflects a fully discharged battery

SoH: state-of-health indicates the current (diagnostic) and future (prognostic) ability of the battery to perform work

SoF: state-of-function indicates the cells ability to deliver a certain amount of energy or power under the prevailing operating conditions

RuL: Remaining-useful-life refers to remaining live-time of the battery under the current operating conditions

Nomenclature

EC   Ethylene Carbonate

BCU   Battery Control Unit

BEV   Battery Electric Vehicle

BMU   Battery Management Unit

BP   Back Probagation

CAN   Controller Area Network

CC   Constant Current

CV   Constant Voltage

ECN   Equivalent Circuit Network

EIS   Electrochemical Impedance Spectroscopy

EKF   Extended Kalman Filter

EMF   Electro- Motive Force

EoL   End of Life

ESS   Energy Storage System

EV   Electric Vehicle

HPPC Hybrid Pulse PPower Characterisation

IEC   International Electrotechnical Commission

IHP   Inner Helmholtz Plane

MP   Multiple Particle (model)

MQB   Modularer Querbaukasten (eng. Modular Tranversal Toolkit)

NEDC New European Driving Cycle

OCV   Open Circuit Voltage

OEM   Original Equipment Manufacturer

OHP   **O**uter **H**elmholtz **P**lane

PHEV   **P**lug-in **H**ybrid **E**lectric **V**ehicle

PP   **P**olynomial approximation **P**article (model)

PU   **P**er **U**nit

RBF   **R**adial **B**asis **F**unction

RC   **R**esistor **C**apacitor (battery model)

REGEN   **REGEN**erative braking

RINT   **R**esistance (**INT**ernal) (battery model)

RUL   **R**emaining **U**seful **L**ife

SAO   **S**afe **O**perating **A**rea

SoF   **S**tate **of** **F**unction

SoH   **S**tate **of** **H**ealth

SP   **S**ingle **P**article (model)

$\triangle G_i$ Change in free energy of a reaction $[\mathrm{J\,mol^{-1}}]$

$\triangle \bar{G}_i$ Change in free electrochemical energy of a reaction $[\mathrm{J\,mol^{-1}}]$

A_{if} Interface contact area $[\mathrm{m^2}]$

A_{o} Convective area $[\mathrm{m^2}]$

A_{s} Particle shell surface $[\mathrm{m^2}]$

a_{s} Electrode active surface $[\mathrm{m^{-1}}]$

a_i Chemical activity of species i $[\mathrm{mol\,m^{-3}}]$

C_{p} Specific heat capacity $[\mathrm{J\,kg^{-1}\,K^{-1}}]$

c_i Concentration of species i $[\mathrm{mol\,m^{-3}}]$

$D_{\mathrm{Li+}}$ Electrolyte diffusion coefficient $[\mathrm{m^2\,s^{-1}}]$

E^0 Standard redox potential of an electrode $[\mathrm{V}]$

E^{eq} Equilibrium electrical potential of an electrode $[\mathrm{V}]$

$E^{\mathrm{eq*}}_{\mathrm{Li}i}$ Apparent electrode equilibrium potential $[\mathrm{V}]$

h Convective heat transfer coefficient $[\mathrm{W\,m^{-2}\,K^{-1}}]$

i^0 Exchange current density $[\mathrm{A\,m^{-2}}]$

I_{bat} Net reaction current at electrode $[\mathrm{A}]$

i_{Ox} Anodic/oxidation current [A]

i_{Red} Cathodic/reduction current [A]

J^{ch} Chemical species flux $[\mathrm{mol\,s^{-1}}]$

k Charge transfer reaction rate $[\mathrm{m\,mol^{-0.5}\,s^{-1}}]$

m_i Molar amount of species i $[\mathrm{mol\,m^{-3}}]$

n Number of electrons participating in a reaction $[\mathrm{mol\,s^{-1}}]$

q_{c} Ohmic heat $[J]$

q_{e} Entropic heat [J]

q_{j} Joule heat $[J]$

q_{r} Reaction heat [J]

R_{if} Interface contact resistance $[\Omega]$

r_{s} Particle radius $[m]$

T Temperature [K]

t_{+}^{0} Ion transport number or transference number

V_i Volume occupied by species i $[\mathrm{mol\,m^{-3}}]$

$x_{\mathrm{Li}i}$ Stoichiometry / molar fraction of speices i $[-]$

z_i Valence of a species i [V]

C_6 Carbon

CoO_2 Cobalt Oxide (cathode electrode)

$Li\,C_6$ Carbon (anode electrode)

$LiCoO_2$ Lithium Cobalt Oxide (cathode electrode)

$LiFePO_4$ Lithium Nickel Cobalt Manganese Oxide (cathode electrode)

$LiMO_2$ Lithium Metal Oxide (cathode electrode)

$LiNi_xCo_yAl_zO_2$ Lithium Nickel Cobalt Aluminium Oxide (cathode electrode)

$LiNi_xCo_yMn_zO_2$ Lithium Nickel Cobalt Manganese Oxide (cathode electrode)

$LiNiO_2$ Lithium Nickel Oxide (cathode electrode)

$LiTi_4O_5$ Lithium Titanate Oxide (cathode electrode)

MO_2 Metal Oxide M=Al,Mn,Co,Ni,etc.

NiMH   Nickel Manganese Hydride

$\mathrm{Zn-Air}$ Zinc-Air

ZnC Zinc-Carbon

F Faraday constant [$\mathrm{C\,mol^{-1}}$]

R Gas constant [$\mathrm{J\,mol^{-1}K^{-1}}$]

α Anodic/cathodic transfer coefficient (symmetry factor) [-]

$\bar{\mu}_i$ Electrochemical potential of species i [$\mathrm{J\,mol^{-1}}$]

δ Domain thickness [m]

η Overpotential [V]

$\eta_{\mathrm{Li}i}^{\mathrm{d}}$ Diffusion overpotential in the electrode [V]

γ Activity coefficient

κ Lithium ionic conductivity in the bulk electrolyte [$\mathrm{S\,m^{-1}}$]

λ Debye length [m]

$\mu_{e,i}$ Electrostatic potential of species i [$\mathrm{J\,mol^{-1}}$]

μ_i Chemical potential of species i [$\mathrm{J\,mol^{-1}}$]

μ_i^0 Standard electrochemical potential at reference conditions [$\mathrm{J\,mol^{-1}}$]

ϕ_i Electrical potential of a species i [V]

ρ Density [$\mathrm{kg\,m^{-3}}$]

ε_0 Permittivity of free space [$\mathrm{F\,m^{-1}}$]

ε_{r} Dielectric constant [$\mathrm{Fm^{-1}}$]

ε_{s} Active material volume fraction [$-$]

Ψ Model parameter affected by changes in temperature

ζ_i Stoichiometry-dependent interaction energy coefficient of electrode i [-]

0 standard condition

amb ambient

a anode

bat battery

b domain bulk property

ch chemical

ct charge transfer

c	cathode
dl	double layer
d	diffusion
e^-	electron
eff	effective
el	electric
eq	equilibrium
eq*	apparent (equilibrium potential)
ic	interface contact
int	intercalation
Li^+	lithium-ion
l	liquid (electrolyte)
oc	open circuit
pl	passivating layer
ref	reference
s	solid (electrode)
t	total
i	chemical species, electrode or modelling domain
Ox	Oxisised species in a reaction process
Red	Reduced species in a reaction process

Chapter 1

Introduction

1.1 Will electric vehicles win the race?

> 'The market is approaching a tipping point, where battery power will become as normal as petrol or diesel. If you look back over the past three years, the electric car market has multiplied by a factor of 25.' - Ian Robertson, BMW's global marketing chief - 2014. [13]

Vehicle electrification and emission reduction of passenger transport is an exciting trend which continues to demand great attention from vehicle manufacturers, researchers, investors and customers. Higher fuel efficiency, improved power performance [14] and reduced emissions [15] are some of the many benefits associated with hybridisation of the power train. These factors have already enabled a growing market penetration over the past years.

Current market data of electric vehicle sales indicates the beginning of a significant market uptake in the last three years 2012 (120,000 PHEV/BEV), 2013 (200,000 PHEV/BEV) and 2014 (300,000 PHEV/BEV) [16]. Extrapolation of these sales statistics results in sales predictions in agreement with major market prognoses by ABB and Avicenne which predict sales of $6\,m$ electrified vehicles (amongst which $1-1.5\,m$ PHEV and BEV) by 2020 [17, 18]. These predictions are conservative, with other market analyses predicting sales of up to $2\,m$ PHEVs and BEVs by 2020 [19]. Battery sales predictions are closely related to these statics, which are estimated to be $20-50\,GWh$ by 2020 and even $75-200\,GWh$ by 2025. The reason of these wide prediction ranges are uncertainties in the speed of market uptake in different uptake scenarios.

The uptake of vehicle electrification has been reflected in the production portfolios of international Original Equipment Manufacturers (OEMs), most of whom are offering one or several electrified vehicle options. The automotive sector is notoriously competitive, leading to OEM's offering a broad range of vehicles which are targeted at specific customer's requirements [20]. Computer aided design, advanced forms of prototyping (e.g. 3D rapid prototyping) and modifiable full-size prototypes (e.g. the MQB platform by VW [21]) have facilitated a cheaper and wider diversification of vehicle sales portfolios [22].

Shorter vehicle development cycles and the introduction of the 'mid-cycle refresh' increase product desirability, hence ensuring that customers continuously remain enticed to upgrade or change their vehicles [23]. The phenomenon of this effectively shortened life-cycle was first harnessed as a deliberate production planning strategy by Alfred P. Sloan jr., then head of General Motors, at a period of automobile market saturation around 1924 [24]. This diversification following customer interest, as well as favourable socio-economic and environmental conditions paved the way towards electrification of passenger vehicles.

Many economic drivers will determine the financial success of battery powered vehicles. Firstly, the demand for vehicles in general which is highly dependent on an economy's financial prosperity. At times of economic uncertainty, customers are less inclined to invest in a new vehicle, especially a novel technology type, while at times of prosperity they will be more likely to do so. Elon Musk, CEO of Tesla Motors, noted recently that EV's 'true competition is not the small trickle of other (non-Tesla) electric cars being produced, but rather the enormous flood of gasoline cars pouring out of the world's factories every day' [25]. It can be inferred that, although demand for vehicles worldwide might be growing, the success of battery powered vehicles is mostly depending upon their value proposition in comparison to conventional vehicles [26]. As such, the biggest hurdles to be overcome are cost and the concept of range anxiety. Customers do not trust that the battery capacity provided will suffice for them to reach their destination. The concept of innovation adoption life cycle is particularly applicable here. Why should you dare to invest in a novel car where you cannot be sure about its range and lifespan? Why not rather wait until an upgrade is developed or the success of such a vehicle is demonstrated in-use by others?

From the perspective of customers, important aspects when considering whether to buy an (electric) car are initial vehicle purchase price, running costs, the ability to deliver on what is promised (range, lifetime, style, performance, safety etc.), available financing options and regulatory incentives/constraints. Thorough comparative studies of these aspects have been carried out by McKinsey & Co., Ricardo-AEA plc. and Element Energy ltd. [19, 27, 28]. These studies agree that battery powered vehicles could overtake internal combustion vehicles at some point in the future given good market adoption, financial incentives and environmental policies (such as zero emission policies in cities). The reports conclude that the high purchasing price, doubts over performance and safety concerns currently hinder their uptake. A significant factor of uncertainty in their analysis is the anticipated cost reduction of low-emission vehicles and the battery technology at their core; the battery cost to the OEM is a key component of this and accounts for the majority cost component of an electric vehicle to a car manufacturer [29]. As batteries are commonly purchased from third party manufacturers by the OEM, this cost component tends to be passed on to the end car buyer, resulting in non-competitive market prices of vehicles.

The pricing power, development and intellectual property in the relatively small battery market of 74 bn is held mainly by Japanese (57%), South Korean (17%) and Chinese (13%) manufacturers [30]. In moving forward, OEMs will benefit from forming strategic alliances with such companies. By ultimately vertically integrating the production of their battery cells, a full understanding of the complex processes involved may be obtained and the dependency on the cell manufacturer as a third party be avoided. Internalising sectors of another industry has not been necessary to this extent in the automotive industry since

the commercialisation of internal combustion engines (e.g. industrial engine manufacturer Rapp Motorwerke merging with vehicle manufacturer Fahrzeugfabrik Eisenach to become an internal combustion vehicle manufacturer Bayrische Motor Werke - BMW). Only by internalising the development and manufacturing of batteries specifically for automotive applications will OEMs be able to internalise the profit currently made by battery manufacturers and offer electric vehicles at competitive prices.

Safety has become paramount in new designs which incorporate ever more energy dense batteries. Due to a lack of understanding of the underlying electrochemical processes and degradation phenomena, battery packs are commonly oversized and underutilized to ensure longevity and robust operation, leading to unnecessarily high costs. This excess capacity provided to the user ensures that the ratings provided by the manufacturer in terms of durability, range and life are provided by the vehicle under commonly encountered operating conditions. More specifically, the battery packs tend to have an operational State of Charge (SoC) window of 70% (10% at the top-end of the SoC range and 20% at the bottom-end of the SoC range remain unused) [31].

When aiming to minimise over-specification, complexity, cost and size of batteries, while adhering to safety regulations, it is essential to improve the performance prediction capability of the Battery Management System (BMS). This in turn necessitates a fundamental understanding of the electrochemical processes occurring inside the battery cells. Many researchers have in the past aimed to build models which account for these complex phenomena under a wide variety of operating conditions. There is a large range of battery models of which the most complex incorporate equations describing the electrochemical processes on the basis of fundamental principles. These computationally demanding models are unsuitable for in-situ implementation into a battery state observer as they are too complex in nature for on-board evaluation. At the other extreme stands the too often taken approach of treating the electrochemical storage device as a "black box". The algorithms inherent to this approach tend to be derived from extensive battery testing of an implemented prototype system under various expected operating conditions. This kind of system learning is time consuming. Furthermore, order-reduction methods lead only to empirical models which are only accurate under the previously parametrised (laboratory) operating conditions [32]. In answer to these two extremes, electrical engineers have developed equivalent circuit networks, which replicate the behaviour of a cell (essentially by curve-fitting); however, not reflecting the true understanding of processes occurring inside the cell either and only attempting to replicate the capacitative and resistive processes.

The demand for a more sophisticated battery performance predictor gives rise to the need for a phenomenological approach in equivalent circuit modelling which can run at the low computational power available on vehicles. This aspect of on-line battery performance prediction therefore requires further development and is the main focus of this thesis.

1.2   Optimising the energy chain - why we need battery performance prediction

When evaluating the performance of the on-board energy storage system (ESS) of a battery powered vehicle, it is useful to visualise the various steps of energy conversion
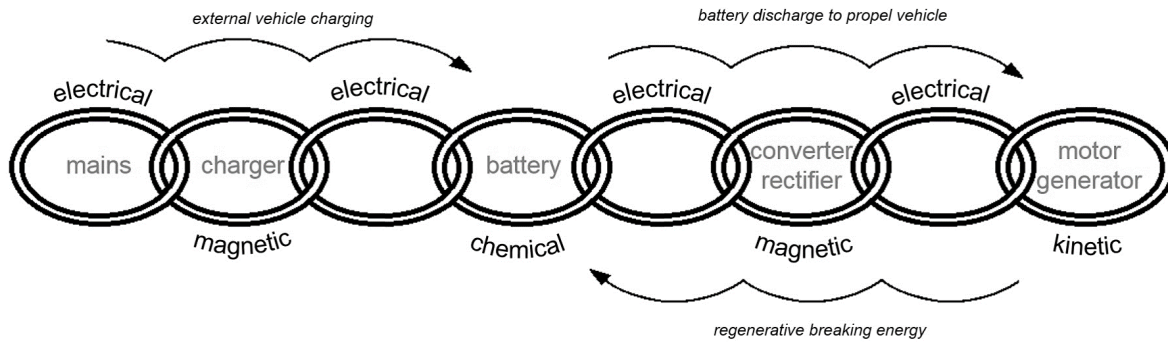
Figure 1.1: Energy chain symbolising the conversion of energy from mains to finally being applied to the motor to propel the vehicle

from electrical energy provided from the grid to the vehicle, up to the ultimate load in form of battery discharge (Figure 1.1). Electric energy is initially supplied to the vehicle via a charger and is stored chemically in the battery. When driving , the chemical energy stored in the battery is converted into electric energy and supplied to the motor propelling the vehicle. During regenerative braking, kinetic energy is recovered back into electric energy, rectified and stored as chemical energy in the battery for later use in propelling the vehicle.

In order to maximise the use of the energy in the battery pack, all energy links in this chain have to be well understood, monitored and controlled. Up to this day, the battery pack inside vehicles is too often regarded as a "black box" with empirically predicted behaviour in its control software. Moving forwards, a more detailed performance prediction is required in order to account for phenomena which will ultimately lead to a degradation of battery performance.

The following prediction, monitoring and control tasks aim to regulate the battery and are integral to commercial Battery Management Systems:

- Provide information on battery State of Charge (SoC), State of Health (SoH), State of Function (SoF) and Remaining Useful Life (RUL).

- Maintain the battery in a state in which it can fulfil the <u>immediate</u> requirements by maintaining operation within a safe operating envelope.

- Maintain the battery in a state in which it can fulfil the general requirements of the application for as long as possible in <u>future</u> cycles.

- Provide fail safe mechanisms/limp home mode/emergency shut-down functions.

- Provide a traceable software environment where malfunctions and unforeseeable results are reproducible in order to isolate the source of the problem.

- Predict real-time battery performance while considering accuracy, robustness and adaptiveness to low-cost platforms onto which it is implemented.

1.3 Objective of thesis and research questions

In this thesis the development of a new phenomenological battery modelling framework is presented. It is obtained by combining detailed knowledge of cell electrochemistry with the principles of electrical engineering. The mathematical equations describing the complex phenomena during electrochemical reactions are translated into electric circuit elements while retaining a physical meaning of each and without masking, merging or grouping any underlying phenomena/processes. The multiple coupled battery internal processes and phenomena are impossible to isolate and measure in practise, even in a laboratory environment, which makes this simulation a useful tool for gaining insight into the processes occurring during cell operation.

As the physical meaning of each circuit element in the model is retained, physical states can be monitored easily. Knowledge thereof ultimately allows the derivation of a compact battery performance estimator enabling the observation of any internal process in the form of a 'transparent' model.

The visibility of detailed variables allows for optimised control and safeguarding of the individual cells and the battery pack by the BMS, while enabling a more accurate prediction of SoC, SoH, SoF and RUL. As such, this model implementation is designed to be useful to system control engineers. Accurate SoC and SoH prediction based on the fundamental principles of electrochemistry will not only allow designers to better estimate the lifetime of the battery for warranty purposes, but will also render electric vehicles more marketable to customers as a reliable means of transportation.

1.4 Aims

The following aims have been set for the model derived in this thesis and adopted as design criteria of the new equivalent circuit model. In Chapter 4 the previously proposed models by other researchers will be assessed against these criteria. At the close of Chapter 5 the newly derived model will be compared against these aims to discuss the achievement thereof and to highlight areas of further improvements.

1.4.1 New model design criteria

As batteries have become an important building block in modern technology, so has the significance of good modelling and performance prediction as part of control systems grown. The wealth of pre-existing work will be assessed with the aim of establishing knowledge gaps in the following system design and model capability criteria. Models and methodologies proposed in the academic literature are assessed against these criteria in Chapter 4, as well as against the proposed new phenomenological equivalent circuit network at the close of Chapter 5.

1.4.2   System development criteria

The following criteria were established with regards to system design and implementation:

· Development of a computing methodology and experimentally validated equivalent circuit model of a lithium ion battery over length and time scales relevant to automotive applications which captures the relevant physics phenomena of interest

· Translation of electrochemical phenomena into electrical analogies:

  – Each circuit element is to retain a physical meaning.
  – Distinct circuit sections are to be associated with physical phenomena of individual chemical species.
  – Individual domains and local phenomena are to be distinguishable.
  – Variables are to be observable for later implementation of control algorithms; creation of a 'transparent' model.
  – Model extensions are to be easily added.

· Prediction on the basis of on-board available live variables current, voltage and temperature (i.e. no hardware modifications).

· Development of a visual implementation allowing easy parametrisation/adaptation to different cell dimensions.

· Parametrisation through a separate script with an easily modifiable parameter list.

1.4.3   Model prediction capability criteria

The models already presented in the literature cater for different degrees of accuracy, speed and scientific sophistication; making them suitable only for the prediction of specific phenomena and basic cell behaviour. In the quest for optimised battery usage and degradation prediction in automotive applications it is essential to model the individual electrochemical contributors leading to observable battery behaviour. Only this way can the resulting electrical behaviour of a cell be fully replicated. The proposed model is therefore to have the following prediction capabilities:

· Prediction of the following phenomena by developing a physics based electric equivalent circuit of the electrochemistry governing equations describing the processes in the battery:

  – Local chemical species concentrations and chemical/electrochemical/electric potentials
  – Electrochemical double-layer with variable capacitance as a function of local concentration gradients

- Passivating layer growth, with variable layer resistance and capacitance allowing for the prediction of loss of active cyclable material and capacity and power fade
- Variable charge-transfer resistance
- Variable exchange current density as a function of local concentrationStoichiometry-dependents gradients
- Local cell characteristics to be coupled to local temperature
- Electrochemical potential to be derived on the basis of Nernst equations and standard redox potentials, rather than empirical functions
- Diffusion limitations to mass transport
- Activation overpotential for electrochemical reactions to take place
- Spatial discretisation to allow the distinction between local effects occurring at anode, cathode and separator
- Full thermal coupling at the same spatial discretisation to allow for a thermal resolution and the evolution of local temperature as a result of the evolution of local electrochemical properties

- Demonstration of the model capabilities in predicting battery performance under typical automotive characteristic operating conditions

1.4.4 Research questions

Through the development of these tools and the methodology it is hoped that a number of different research questions are answered.

- What are the prediction limitations of a battery model cast in the form of an equivalent circuit model for automotive applications?
- What additional information can be unlocked given the same measurement inputs as conventional black-box models?
- What improvement in prediction accuracy is enabled due to this additional information becoming available?

Where this work aims to add value to the existing academic literature is in creating a transparent model, allowing the observation of parameter states in lieu of control system implementation. This is in order to allow the observation and control of performance characteristics on the basis of fundamental operating principles. Although cast in the framework familiar to application engineers, the model is essentially an electrochemical battery model: all variables have a direct physical interpretation and there is direct access to all states of the cell via the model variables (species concentrations, potentials etc.) for the purpose of battery state control. The development of equivalent circuit networks for each of the complex physical processes and degradation mechanisms occurring in a lithium ion battery is a near exhaustive task and beyond the scope of a single PhD project.

Rather, the approach taken here is aimed at developing the tools and methodology required to incorporate further physical processes relevant to specific applications. As such, the presented methodology can be further refined by implementing additional degradation mechanisms (or physical phenomena in general) atop the present framework.

1.5   Hypothesis

Based on the research questions proposed, the following are working hypotheses to be investigated in the following thesis.

- · A wealth of additional information on internal battery performance characteristics can be extracted, given the basic live measurements available on a vehicle (current, voltage and temperature).

- · This information can be used to compute a more accurate prediction of presently predicted battery states.

- · This information allows the prediction of additional battery states, which have so far been inaccessible. Effects such as cell capacity and power fade can be predicted based on physical phenomena, rather than by empirical laws.

1.6   Thesis structure

First, the operating principle of a lithium-ion battery, design and performance requirements in automotive applications are introduced. Subsequently, a literature research on the current research activities and state-of-the-art in the areas of interest is presented with the aim of assessing the gaps in the current literature. This provides the motivation for the detailed model derivation of the new phenomenological equivalent circuit model in the subsequent chapter. The final chapter presents application and results of the model under various standard battery testing load cycles as well as realistic automotive drive cycle loads.

- · Chapter 2: **Introduction to lithium-ion batteries in automotive applications**

- · Chapter 3: **On-line battery performance estimation**

- · Chapter 4: **Battery modelling**

- · Chapter 5: **The new phenomenological equivalent circuit model**

- · Chapter 6: **Model applications and results**

- · Chapter 7: **Conclusions**

- · Chapter 8: **Future work**

Chapter 2

Lithium-ion batteries in automotive applications

Overview

This chapter provides an introduction to lithium-ion batteries. After presenting important historical developments in the field of electrochemical science with relevance to battery research, the basic operating principles of a lithium-ion battery are explained. The significance of battery design criteria, such as material, cell structure and shape in meeting the high-energy or high-power requirements of automotive applications are discussed. Finally, an overview of the causes of degradation of electrochemical performance over extended periods is given.

This chapter aims to communicate the complexity of electrochemical processes in batteries and justify the need for the derivation of a phenomenological equivalent circuit model able to describe them appropriately.

2.1   A short history of the battery

The first reports of electrochemical energy storage date from 250 BC, where the assembly of iron and copper electrodes, flooded with an organic acidic solution (probably accidentally!) resulted in a galvanic cell of c.a. 0.25 V and 50 mAh [33]. Scientific research in the field of batteries has flourished since the 18th century, when Luigi Galvani investigated electrical impulses in frog muscle. Alessandro Volta's experiments with current flow between iron and copper metals allowed him to conclude that electricity must be generated fundamentally from chemical species and their interactions [34, 35]. Michael Faraday built on Volta's discoveries in the 1840s, establishing the relationship between electrochemical and electric potential. Progress in the use of different chemical agents was made by Gaston Planté in 1859, who assembled a lead-acid cell comprising two sheets of

lead separated by rubber strips, rolled into a spiral and submerged in a sulphuric acid solution. By applying a potential difference between the lead and a lead-dioxide electrode he was able to charge a cell for the first time, obtaining an open circuit potential of 2.7 V [36]. In 1866, George Leclanché developed a zinc-carbon 'wet-cell' comprising a carbon manganese dioxide mixture on a graphite plate as the cathode, zinc as the anode and an ammonium chloride solution as the electrolyte - the Leclanché cell. This early discovered combination of chemicals is still prominent in modern household-use Zinc-Carbon (ZnC) primary cells (20%) of all portable batteries in the UK), although with vast cell capacity improvements [37].

The predecessor to today's commercial rechargeable nickel-cadmium and nickel-iron alkaline batteries was developed by Waldemar Jungner around 1899 [38]. The use of alkaline solutions allowed more freedom in the choice of electrode and casing material as alkaline solutions were found to be less prone to undesirable side-reactions when brought into contact with the other cell components. The work of William Grove on fuel cells from 1839 significantly contributed to a better understanding of the origin of gasses in electrochemical reactions. The gas pressure build-up in new types of batteries had been a barrier to higher cell capacity up to this point. This knowledge was later applied to metal-air batteries, in particular Zinc-Air (Zn-Air) based cells [39].

In 1913 Gilbert Lewis first demonstrated the usefulness of lithium as an electrode material in various experiments but it was not until the 1970s when the first non-rechargeable lithium-metal cells were developed by NASA and the US Department of Energy [36]. The contribution of John Goodenough in 1980 in developing lithium cobalt oxide cathodes in cell assemblies represents a significant milestone in lithium-ion battery battery research and eventually led the commercialisation of $LiCoO_2$ cells by Sony in 1991 [38].

The idea of the battery as the energy reservoir for propelling vehicles, tricycles, carts and locomotives surfaced at a time of great inventorship when many electrified gadgets and curiosities where presented to the public at the World Expositions in the 1870s, 80s and 90s. The development of electric vehicles has, since the beginning, always been a close collaboration between automobile manufacturers and electrochemists. The nature of this joint effort in developing cells specifically to achieve the financial success of electric vehicles has changed significantly over the last 100 years. The handful of electrochemistry scientists and enthusiasts has grown into an independent battery manufacturing industry worth globally in excess of \$70 bn, serving a vast variety of industries. The automotive industry in the meantime turned away from this novel idea and profited enormously from developing the comparatively cheap and safe internal combustion engine. Only in recent times has the development of electric vehicles again become focus of research and investment. For the battery industry, the success of electric vehicles represents a one of many growing revenue streams in a flourishing market, whereas batteries could evolve to be instrumental to the future of the entire automotive industry.

Today, vast improvements in the process of developing modern battery powered vehicles have already been made. Automotive manufactures have optimised the electronic circuitry around the actual battery and harnessed the performance of the best available cell technologies on offer.

Knowledge of the complex and distinct design properties and behaviour of batteries is either fiercely protected by battery manufacturers or non-existent as this information

might not be required for the majority of their customers. The much more stringent requirements for automotive applications have created a market situation where buyers are to some extent dependent on their suppliers without whom their future main revenue drivers will fail to flourish as well as on extensive cell testing. Simultaneously, new battery technologies appear on the market while research is catching up to fully understand the processes inherent to already marketed cell chemistries to a standard sufficient for a successful implementation.

This has resulted in an extreme interest in battery research to de-mystify this complex component and to create a clear understanding of the battery as the fundamental building block of electric powertrains.

2.2   Battery operating principle

A lithium-ion battery typically comprises porous electrodes (anode and cathode), an electrically insulating separator in-between and an ionically conducting medium (electrolyte). Both electrodes are typically an electroactive material mixed with electrically conducting additives which are coated to an aluminium current collector (as the cathode) or a copper current collector (as the anode). The active material of the electrode serves as a host material into which mobile lithium-ions can be intercalated from the electrolyte or they can be extracted. The electrolyte consists of a salt dissociated in an organic mixture of carbonates, which immerses the anode, cathode and separator. This separator in-between anode and cathode prevents electron transport between the electrodes through the inside of the cell, while allowing lithium-ions to permeate.

When fully charged, a maximum amount of lithium is intercalated inside the anode. During discharge lithium leaves the anode and is each oxidised to an electron and a lithium-ion in an electrochemical reaction at the electrode/electrolyte interface. Equation 2.1 describes the oxidation reaction at a carbon anode C_6 and states that n lithium stored (intercalated) in the anode electrode (LiC_6) participate in an electrochemical reaction, such that

$$Li_nC_6 \underset{\text{charge}}{\overset{\text{discharge}}{\rightleftharpoons}} n Li^+ + n\,e^- + LiC_6, \qquad (2.1)$$
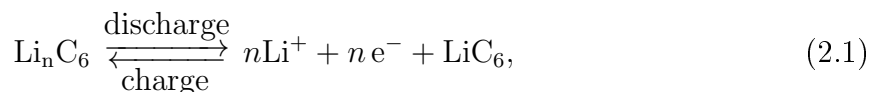
yielding n lithium-ions Li^+, n electrons e^- and remaining active host material LiC_6. The lithium-ions are released into the electrolyte, while the porous separator, which serves as an electronic insulator between anode and cathode, forces the electrons to follow a different path to the lithium-ions through an external circuit via the current collectors. Figure 2.1b) shows a schematic of this process. The lithium-ions travels through the electrolyte phase by diffusion due to concentration gradients to the cathode and react each with an electron from the external circuit. This reduction reaction at the cathode electrode/electrolyte interface where lithium-ions and electrons are reduced to intercalated lithium is formally expressed for a metal oxide MO_2 electrode as
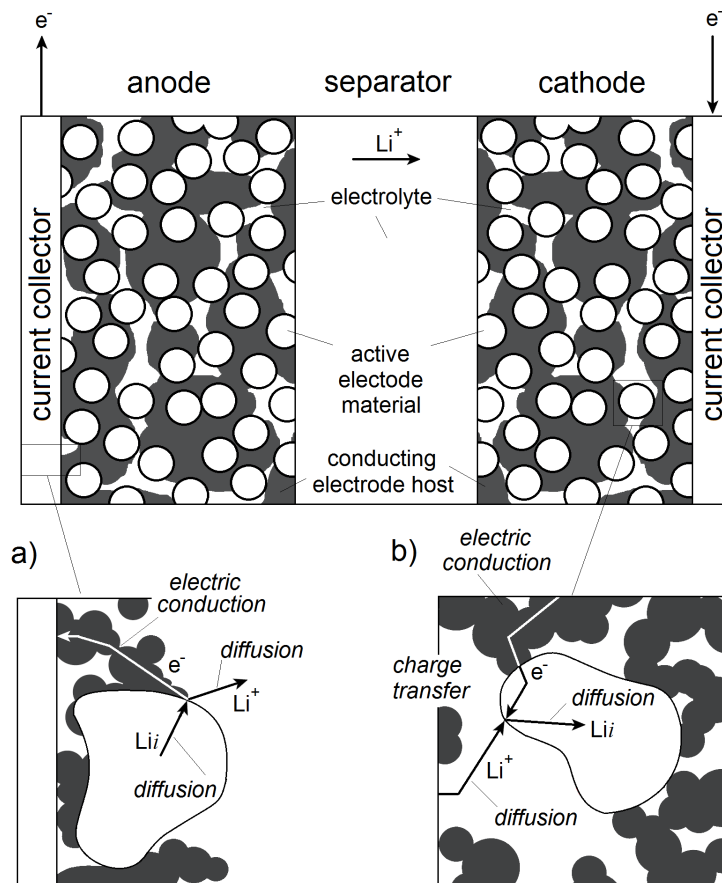
Figure 2.1: Battery schematic showing the direction of intercalated lithium Li*i* (*i* = anode, cathode), electron e$^-$ and lithium-ion Li$^+$ movement during discharge. Reduction and oxidation reactions occur at the electrode/electrolyte interfaces, which are distributed throughout the porous electrode; black: electrically conducting host material, white circles: active material particles (which are not necessarily spherical in reality, as seen in the bottom insets), italics: species transport phenomena and reactions
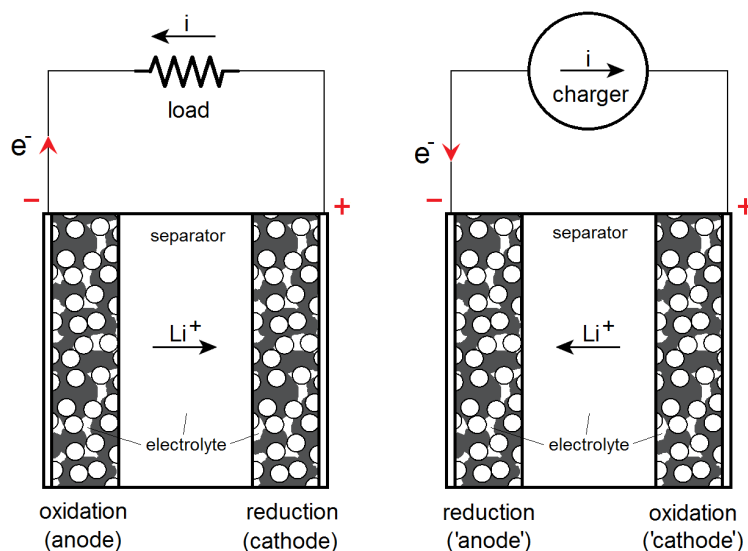
Figure 2.2: Direction of electron and current flux in a battery during discharge (left) and charge (right), apostrophes indicate the definition by convention

$$\text{LiMO}_2 + n\text{Li}^+ + n\text{e}^- \underset{\text{charge}}{\overset{\text{discharge}}{\rightleftarrows}} \text{Li}_n\text{MO}_2, \tag{2.2}$$
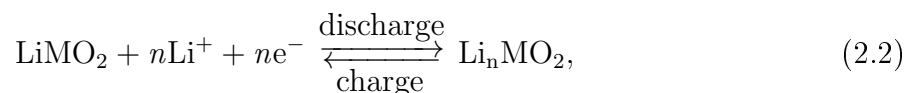
upon which the intercalated lithium diffuses from the surface of the electrode to its bulk. Figure 2.1c) shows a schematic of this process. As a consequence of the reaction direction during discharge, the negative electrode where the oxidation reaction is occurring is commonly referred to as the anode, while the electrode where the reduction reaction takes place is called the cathode. This convention is maintained during charge, although the reduction (cathodic) reaction is now actually occurring at the anode and the oxidation (anodic) reaction is now actually taking place at the cathode. The effect of this convention is depicted in Figure 2.2.

For consistency, the negative electrode will be referred to as the anode and the positive electrode as the cathode during charge and discharge for the remainder of this thesis.

A voltage greater than the open circuit voltage must be applied during charge. Charging a cell causes electrons to flow from the cathode to the anode (Figure 2.2 right). This results in a corresponding ionic-flux inside the cell from cathode to anode; intercalated lithium are oxidised at the cathode, travel through the electrolyte to the anode where they are reduced with the electrons from the external circuit. The positive electrode is still (per definition) referred to as the cathode during charging despite an oxidation reaction taking place at its surface. Similarly, the negative electrode is still referred to as the anode, although a reduction reaction is happening at its surface, as shown in Figure 2.2.

2.3   Battery design

Cell design parameters such as material choice, domain dimensions, cell construction and form factor significantly influence battery performance. For this reason, alternatives for

each of these design aspects will be presented in the following.

2.3.1   Cell materials

In choosing electrode materials, two fundamental quantities are most significant in optimising cell performance:

1. High specific cell capacity $[\mathrm{mAh\,g^{-1}}]$ and energy density $[\mathrm{Wh\,kg^{-1}}]$ to optimise cell packaging, and

2. High cell open circuit potential [V] to maximise the load that can be supplied.

Much research targets the **maximisation of cell capacity**. For commercial cathode materials the specific electrode capacity can be $\sim 120 - 190\,\mathrm{mAh\,g^{-1}}$ [40, 41, 42, 43, 44] while commercial anode materials achieve specific capacities of $\sim 372\,\mathrm{mAh\,g^{-1}}$ (graphite) [45]. This difference in specific capacity indicates that cathode materials pose the capacity-limiting aspect of a cell overall; some are therefore noted in the following:

Lithium cobalt oxide ($LiCoO_2$) based cells are prominent in the portable electronics market due to this chemistry's favourable high theoretical capacity of $\sim 272\,\mathrm{mAh\,g^{-1}}$ and high specific energy of $\sim 1014\,\mathrm{Wh\,kg^{-1}}$. However, limited availability of cobalt has led to relatively high costs of the material and subsequent electrode manufacture. Furthermore, cells of this chemistry have shown early onset of degradation, which was attributed by Belov *et al.* to accelerated CoO_2 layer formation on the anode which increases internal cell impedance, leading to power fade [46, 47, 48]. Amatucci *et al.* further related $LiCoO_2$ cell degradation in terms of capacity fade to the loss of active cyclable lithium, which is tied up in the formation of the passivating layer on the CoO_2 electrode [49, 50, 51, 46, 52, 53, 54]. The danger of thermal runaway as the dominant failure mode is an additional reason for the unpopularity of this cathode chemistry in the automotive industry.

Lithium nickel oxide ($LiNiO_2$) as a cathode material was developed to overcome the limitation of cost [55] although at a compromise of a less ordered and less structurally stable lattice material [55, 10] leading to early cell failure. This issue was addressed by doping the structure with aluminium and/or manganese, resulting in lithium nickel cobalt aluminium oxide ($LiNi_xCo_yAl_zO_2$) and lithium nickel cobalt manganese oxide ($LiNi_xCo_yMn_zO_2$) chemistry-based cathodes (x, y and z stand for weighted ratios of the additives). Optimising the ratio of additives inhibits an impedance increase by the additives and stabilises the charge-transfer reaction process at the cathode electrode surface [56].

Lithium iron phosphate ($LiFePO_4$) was subsequently developed as a cathode material to optimise the electrode's characteristics in terms of thermal stability, thus reducing the likelihood of thermal runaway [10]. Electrodes manufactured with this chemistry have proven to be less expensive [57] and safe as no oxygen is released as part of the electrochemical reaction, thus reducing the risk of cell fires [58, 59]. The list of cathode chemistries in Table 2.1 represents the most popular materials and is not exhaustive.

The most common choice for anodes are carbonaceous materials, namely graphite C_6 (with a theoretical specific capacity $\sim 372\,\mathrm{mAh\,g^{-1}}$), graphitisable soft carbon (with a theoretical specific capacity $\sim 235\,\mathrm{mAh\,g^{-1}}$), non-graphitisable hard carbon (with a theoretical specific capacity $\sim 370\,\mathrm{mAh\,g^{-1}}$) and lithium titanate oxide ($LiTi_4O_5$) (with a theoretical specific capacity of $\sim 175\,\mathrm{mAh\,g^{-1}}$) [60]. The later is found in low voltage applications (due to an anode operating voltage of 1.5 V vs. Li) and exhibit favourable safety and long life characteristics. The much larger electrode nano-structure surface, which is not inhibited by passivating layer growth (as in the other Li-graphite chemistry cells) allows for a significantly higher charge/discharge capability of Lithium titanate cells.

Given the much higher specific capacity of these materials as compared to the cathode materials, the reason for research focus on the cathode becomes apparent.

Cathode material	Theoretical specific capacity $[\mathrm{mAh\,g^{-1}}]$	Average potential $[\mathrm{V}]\,vs.\,\mathrm{Li/Li^+}$
$LiMn_2O_4$	148	4.1
$LiNi_{1/2}Mn_{3/2}O_4$	148	4.7
$LiFePO_4$	170	3.45
$LiCoO_2$	272	4.2
$LiNi_{1/3}Co_{1/3}Mn_{1/3}O_2$	272	4.0
$LiNi_{4/5}Co_{3/20}Al_{1/20}O_2$	272	3.8

Table 2.1: Comparison of selected cathode materials. The practical specific capacities of electrodes made from the each chemistry will be lower (as seen in the figure) due to porosity, additives and binders [10]

The **maximisation of the cell open circuit potential** allows the user to draw a higher power from the cell. A potential difference establishes at the cell terminal due to the difference in potentials of each electrode. The relation between discharged cell capacity and electrode potential is shown in Figure 2.3c). It is interesting to observe that, during discharge, a reduction in intercalated lithium in the anode leads to an increase in the anode electric potential, while an increase in intercalated lithium in the cathode leads to a reduction in the cathode electric potential. The difference of the electrode potentials in Figure 2.3c) results in the cell open circuit potential, shown in Figure 2.3b).
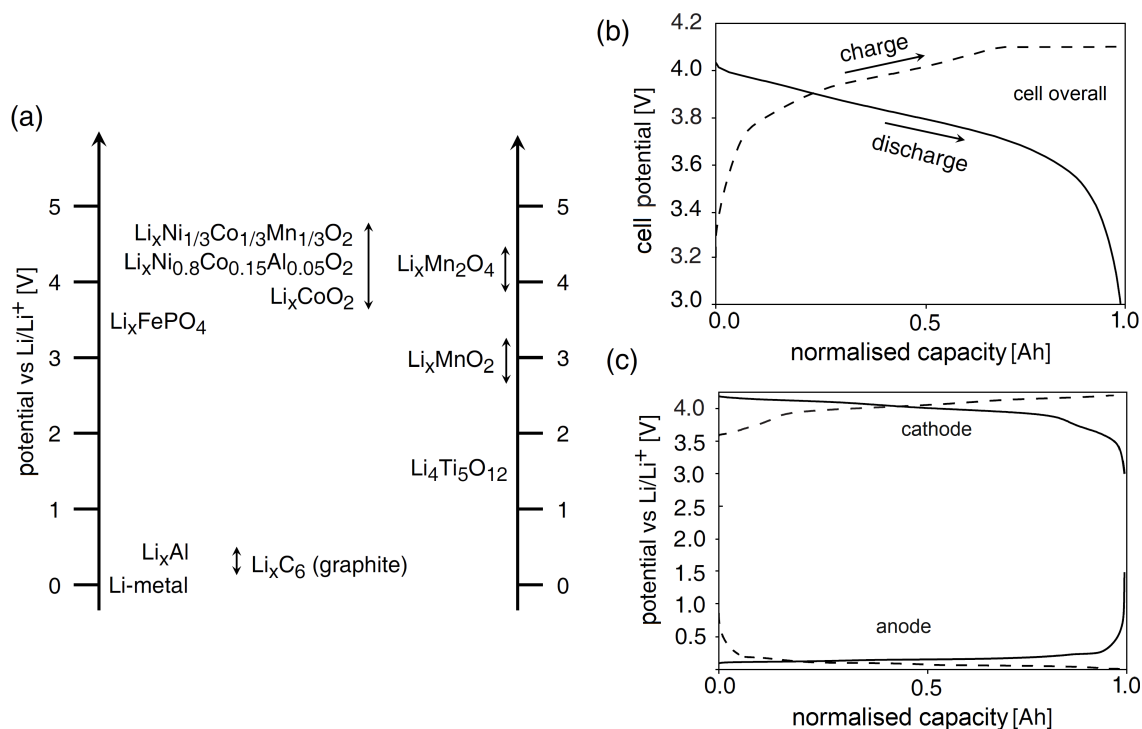
Figure 2.3: (a) Electrode potential ranges of commercially available anode and cathode materials, (b) cell voltage under constant (-) discharge and (- -) charge, and (c) anode and cathode electrode potential under constant (-) discharge and (- -) charge

The electrical potential of commercial cathodes is limited primarily by loss-inducing side-reactions and material stability. The upper limit to the electrical potential of commercial anode materials is constrained by the stability limit of the copper current collector [61], while the lower limit to the electrical potential limit is posed by lithium deposition/plating, breakdown of the solid electrolyte interface and electrolyte decomposition. The potential rages of commercially available lithium-ion battery electrode chemistries is shown in Figure 2.3a).

An optimisation of cell chemistry for a specific load application is essential in good battery system design. The trade-off between the two design criteria, cell open potential and capacity, as well as the shape of the discharge curve have to be considered. In Figure 2.4 several open circuit voltage curves are plotted for cathode materials against capacity. It can be seen that the OCV curve of each cathode chemistry is not constant over capacity but decreases progressively as the cell is discharged. A flat open circuit potential curve allows for a wide voltage operational window of the cell within its system environment, while predicting State of Charge for such chemistries is much more challenging due the small change in voltage over a specific SoC range. Changes in slope of the OCV curve relate to the lithium concentration and lattice arrangement in the host material (causes are discussed in more detail in Chapter 5 and pose a further significant challenge to algorithms predicting SoC.
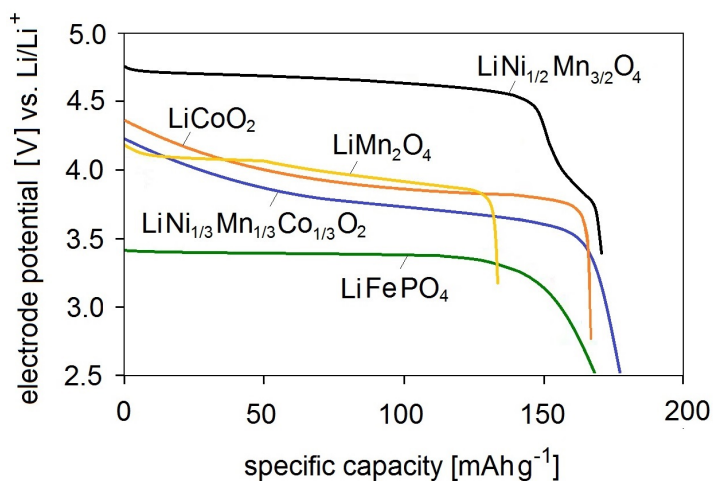
Figure 2.4: Various cathode electrode potentials from Table 2.1 as a function of specific capacity, adapted from [1]

2.3.2 Cell internal construction

Lithium-ion batteries in modern applications are often designed specifically for their intended application. Although cells might look relatively similar in terms of shape and packaging, their internal design parameters such as electrode thickness, porosity, active material structure, particle size/shape, current collector properties, electrolyte types and additives might differ significantly. This is in order to optimise the cell to match the system's power and energy performance requirements. The design difference between high-power and high-energy cell designs is shown in in Figure 2.5a) and b).

he system's power and energy performance requirements. The design difference between high-power and
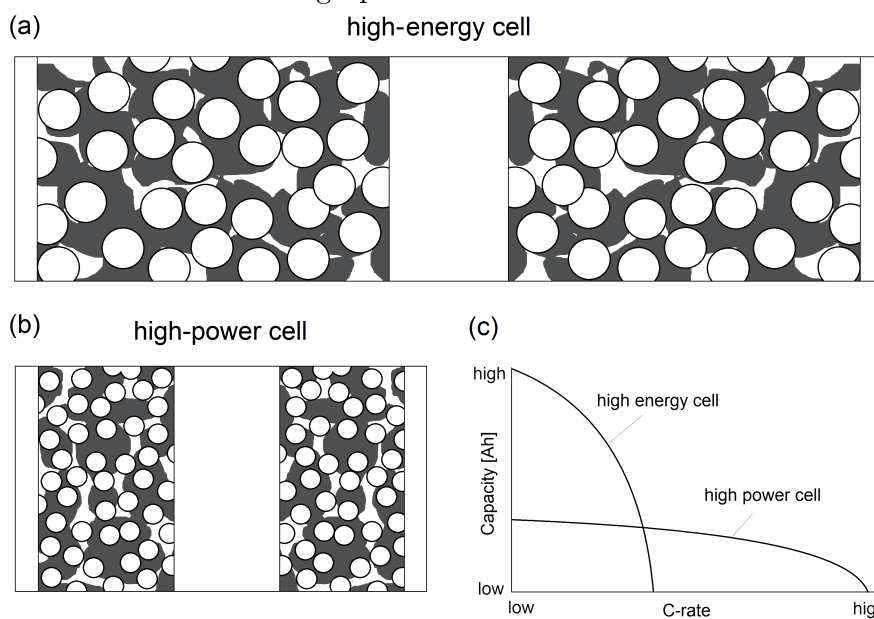
Figure 2.5: Schematic illustrating the difference between high-energy and high-power lithium-ion batteries: (a) high-energy cell, (b) high-power and (c) relation between C-rate and attainable cell capacity. The two cell diagrams are shown at the same scale [2]

· **High-energy cells** for applications such as BEVs and PHEVs, usually comprise thicker electrodes of $\sim 100-200\,\mu m$ (shown in Figure 2.5a) and more active material, allowing more energy to be stored. Consequently, less electrode surface is available for electrochemical reactions to take place and lithium-ions have to diffuse over a longer distance through the electrode before reaching a reaction site $(2-20\,\mu m)$. The rate of conversion from electrochemical to electrical energy is therefore reduced, making the cell less responsive to dynamic loads than a high-power cell.

· **High-power cells** incorporate thinner electrodes of $\sim 35\,\mu m$ (shown in Figure 2.5b) with higher porosity resulting in a large specific surface area. This large surface area leads to short lithium-ion diffusion lengths through the electrodes to the reaction sites of between $0.1-0.5\,\mu m$. The rate of conversion of from electrochemical to electrical energy is therefore very fast, making the cell response to a load very responsive, although being lower in energy density.

As is shown in Figure 2.5c), the reduced transport and reaction limitations in high-power cells allow for higher discharge currents. This makes this type of cell applicable for short-burst type applications such as power-assist modes in HEVs. The high energy-cell, on the other hand, is able to provide a larger discharge capacity due to the larger amount of active material in the electrodes, making it the desired type of cell for low C-rate applications where large battery capacity is required (i.e. BEVs and PHEVs)

2.3.3   Cell form factors

The three types of battery form factors commonly used in automotive applications are cylindrical, prismatic and pouch lithium-ion cells. These designs are subject to standardisation as described in the IEC (International Electrotechnical Commission) ISO standard [62].
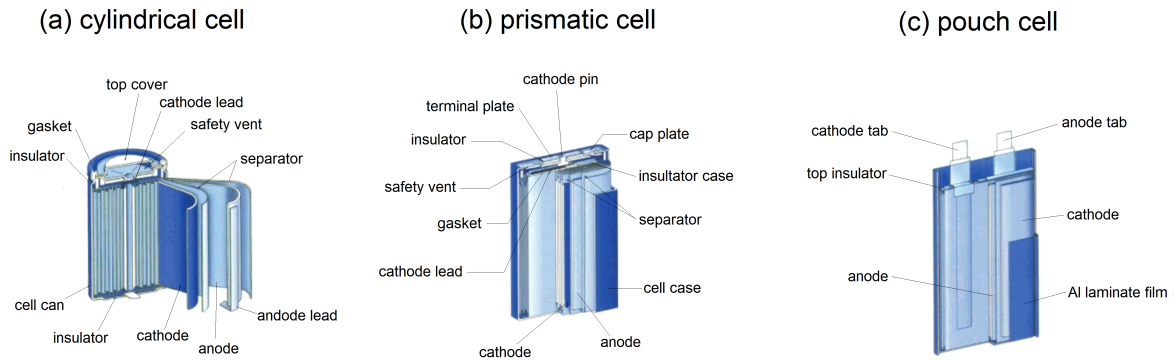
Figure 2.6:   Cell shape variations, modified from [3]

- **Cylindrical cells**, such as those shown in Figure 2.6a), comprise a cell can, giving them good mechanical resilience to external shocks and pressure at relatively low manufacturing cost. Rolling the electrodes like this yields a relatively large surface area, enabling the battery to supply larger discharge currents. Although the cells possess a high energy density within the cylinder casing, the overall energy density of the battery pack is relatively low due to the low packing density of the cylindrical form factor. On the other hand, the 'empty' space between the cylinders may be used for effective cooling. Given the widespread use of this cell shape, their production costs have reduced considerably over the years in comparison to other cell shapes. [29]

- **Prismatic cells** are formed of layered electrodes in the shape of a right prism, as can be seen in Figure 2.6b). Packaging efficiency within a module is thereby improved, although thermal management is more difficult in the remaining space between the cells. Prismatic cells are more prone to bending and impact damage due to the decreased mechanical rigidity of the casing. Increasing impact impact resilience by increasing case thickness reduces the energy density in comparison to cylindrical cells.

- **Pouch cells** are not encased in a rigid structure but in a thin polymer foil pouch, as shown in Figure 2.6c), making this the highest energy density design. This leaves the cells more vulnerable to impact and penetration but also allows large, flat form factors whereby enabling a high heat flux away from the cell. As this type of cell does not have venting valves, a common symptom of cell failure is swelling of the cell pouch. This is a visible and slow failure process as opposed to a build-up of pressure within a rigid casing, followed by a sudden explosion. For this reason, this type of cell is regarded as providing safer fail mechanisms than the former two cell types,
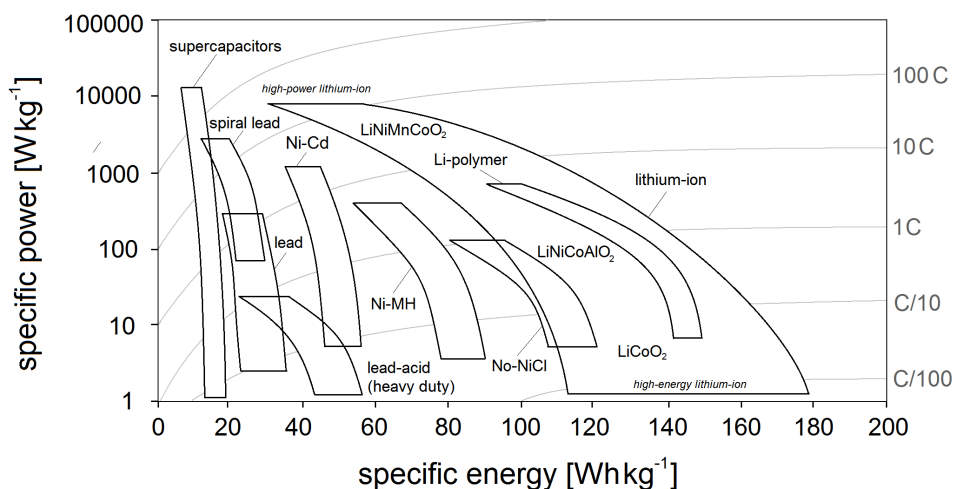
Figure 2.7: Electrode chemistry characteristics (the ranges result due to the dependency on state of charge, temperature and pressure amongst others) .

making it favourable for automotive applications. Additionally, the flat shape allows for tightly packed cell arrangements in the vehicle body floor and makes pouch cells an attractive choice in modern vehicle designs.

2.4 Performance requirements on cells in automotive applications

The demands on BEVs, HEVs and PHEVs batteries differ substantially. This is due to the way they are employed as an energy source in the total energy storage system of the vehicle. Most importantly, it depends on how quickly the battery is required to be able to respond to charge/discharge demands (i.e. the battery power availability or State-of-Function). For HEVs the C-rate can be greater than $40\,C$, for PHEVs it may be around $10\,C$, while the charge acceptance requirements in BEVs is lowest at $\sim 1 - 3\,C$ [63]. The higher the C-rate capability of each individual cell, the more the energy management system will be able to call on electric propulsion and regenerative braking (REGEN) operation, whereby increasing energy efficiency of the vehicle powertrain. Furthermore, short-electric-range PHEVs, for example, will require higher power-to-energy ratio cells than BEVs because higher peak power demands will be distributed over less battery capacity. A higher peak power per unit capacity is available in thinner electrodes, which necessitate higher amounts of inactive electrode materials and has implications on cost, volume, weight and cell life [64, 65, 66, 67, 68, 69, 70].

Various cell chemistries are set into this context in Figure 2.7 and it can be seen that lithium-ion chemistry-based batteries offer a wide range of C-rate, specific energy and specific power. It is the high specific power, and hence C-rate range in combination with high specific energy that make this type of battery so applicable to highly demanding propulsion and REGEN systems in BEVs, HEVs and PHEVs. As the degree of hybridisation increases, the charge acceptance of the battery system grows in importance, justifying the trend from NiMH to Lithium based battery chemistries. From the figure it becomes

apparent that no cell chemistry offers all the desired characteristics, but that achieving an optimum requires trade-offs to be made. In order to address this, cell manufacturers continuously develop new cell chemistries as well as modifications of existing chemistries.

A thorough techno-economic study on optimising cell internal design and pack configuration for electric vehicle applications was conducted by Sakti *et al.* [71] Challenging the fact that most vehicle battery cost analyses treat batteries as though they were all the same and assume a single estimate of cost per kWh of storage, this study encompasses a wide range of design variations in cell design [72]. While fixing the cell chemistry to a Nickel Manganese Cobalt cell, sensitivity studies are performed on electrode design (thick/thin), packaging alternatives (prismatic/pouch/cylindrical) and capacities (size,number of electrode layers, etc.) of cells inside a pack as well as pack configuration, thermal management and control electronics. Including the cost of material sourcing and various manufacturing processes they demonstrate theoretical battery pack cost $(\mathrm{kWh^{-1}})$ reduction potentials. [71]

2.5 Degradation of Electrochemical Performance

A significant challenge for battery system designers is the degradation of initially observed performance characteristics over a cell's lifetime. Operation over extended periods of time leads to various forms of degradation, most of which are influenced by operating conditions such as temperature, cycle number and applied load, to name a few. A reduction in cell capacity (i.e. capacity fade) and an increase in impedance (i.e. power fade) is a primary concern in modern battery management system design, as these changes are usually difficult to incorporate in on-line performance estimators. This is due to the difficulty in isolating the causes and forms of degradation, which are usually complex and interrelated processes, such as chemical and structural changes in the electrodes, electrolyte decomposition, the formation of passivating layers and coverage of previously active reaction surface, the loss of cyclable lithium (and many more) [73]. Moreover, heat generation during operation significantly contributes to the acceleration of these processes.

Degradation of electrochemical performance furthermore depends on cell chemistry, geometry and factors such as ambient temperature and humidity, as well as applied load and voltage. The multitude of these contributing causes and their complex interrelation gives rise to the need of degradation models as extensions to on-line battery performance estimators. The derivation of a model reflecting the electrochemical processes associated with capacity and power fade is detailed in Chapter 5, while at this point an explanation of the phenomena will be provided and their significance on the observed electrochemical performance shown.

2.5.1 Capacity fade

Electrochemical side-reactions occur during operation due to the additives in the electrolyte, namely ethylene carbonate (EC). During the first few cycles of a cell's lifetime, a stable solid-electrolyte interphase is formed on the anode electrode surface by the ethylene carbonate at $\sim 0.8\,\mathrm{V}$ and results in a $\mathrm{Li^+}$ permeable, electronically insulating film
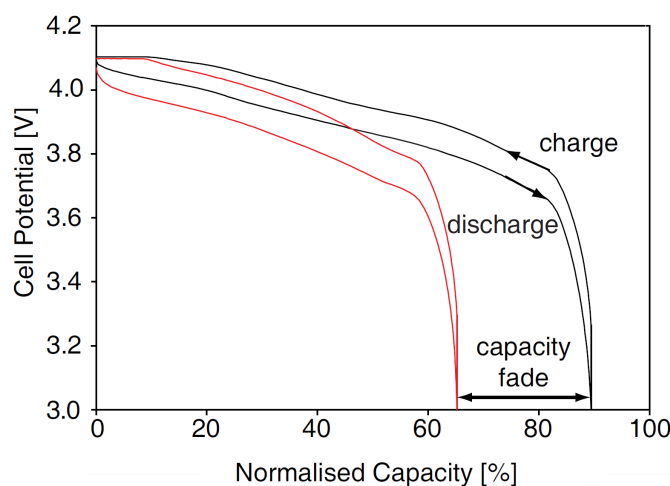
Figure 2.8: Schematic showing the effect of degradation on cell potential over discharged capacity in the form of capacity fade[2]

designed to prevent further electrolyte decomposition [74]. The side-reaction term denotes the non-perfectly reversible intercalation process side exchange current density of this process. A major issue is that this side-reaction causes continued (slow) growth of the passivating layer thickness, which leads to a loss in active lithium species in its build-up, which would otherwise serve as charge/discharge capacity while travelling between the anode and cathode. Capacity fade manifests itself due to:

· a loss of cyclable lithium due to side-reactions tying up lithium-ions in the passivating layer which no longer participate in the redox shuttle

· a loss of active material due to a) local contact losses due to binder decomposition, conductive additive oxidation, current collector corrosion or host material expansion during intercalation, b) host electrode structural breakdown leading to changes in material properties or c) dissolution of the electrode metal from the lattice.

These causes contribute to an irreversible loss of capacity, leading to a changing cycle path over the cell's lifetime [75] and consequently a reduction in attainable cell capacity which is illustrated in Figure 2.8.

2.5.2 Power fade

Over extended periods of cell operation, the effect of increased passivating layer thickness leads to an increase in cell impedance. This increase in impedance has a greater impact at high C-rates, meaning that the power capability of the cell is reduced. This effect is referred to as power fade, although strictly speaking it is potential fade. Multiple causes may contribute to the increase in passivating layer thickness:

· a loss of local contact due to a progressive reduction of active electrode material and conductive additives which are consumed by the passivating layer build-up
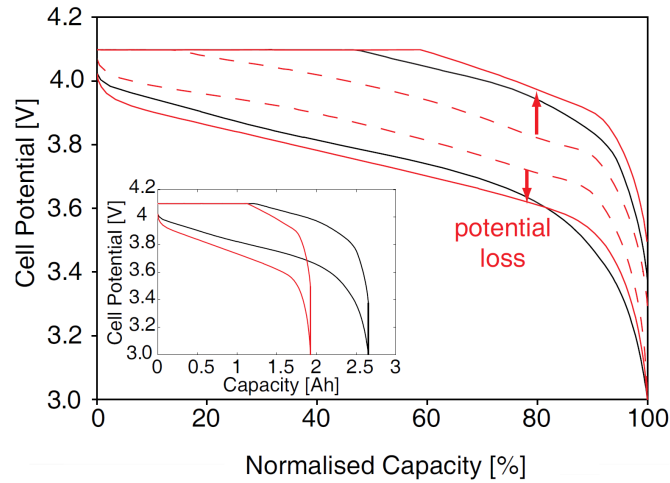
Figure 2.9: Schematic showing the effect of degradation on cell potential over discharged capacity in the form of internal impedance increase (leading to a power fade) [2]

· a reduction of the electrode reaction surface due to the reduction of host material porosity as passivating layers grow

· structural changes of the host materials such as bulk phase transitions which affects reaction kinetics and species transport properties

· changes of electrolyte properties due to local decomposition and solvent evaporation resulting in a change in solvent concentration

· structural changes of the separator, leading to a reduction in porosity

· current collector corrosion leading to increased ohmic resistance

The capacity loss due to passivating layer build-up subsequently causes an internal cell impedance increase, leading to a reduction in useful potential; which (at a constant current) manifests itself in a reduction in available power, which is shown in Figure 2.9.

Chapter 3

On-line battery performance estimation

Overview

In this chapter the operational tasks of Battery Management Systems are discussed and important state and control parameters highlighted. Furthermore, the building blocks to on-board BMSs are introduced, differentiating the computational model of the battery and the decision logic module. The former predicts cell performance states during operating while the latter aims to maintain the cell close or at optimum operating conditions while maximising the cell permissible operating envelope. Finally, the limitations of modern on-board battery performance predictors are set into the context of the technical capabilities of the constituent components, sampling, sensing, subsequent parameter errors and prediction quality due to the lack of suitable battery models.

This chapter aims to communicate the main shortcoming of modern BMSs in terms of the quality of the implemented battery performance algorithms, thus justifying the need for the development of a phenomenological equivalent circuit.

3.1 Introduction

When optimising battery usage it is necessary to adequately predict performance states given current and previous operating conditions. State parameters of particular importance in battery monitoring and control are battery State-of-Charge, State-of-Health, State-of-Function and Remaining useful Life [76]. The ultimate goal of the battery control system is to harness remaining energy such that it is utilised in the most energy efficient manner, while simultaneously ensuring that individual cells are protected from degradation, and operation is maintained within allowable operating thresholds [77, 78].

The estimation of remaining capacity of a battery is not straightforward, as this requires the cell electrochemistry to be in equilibrium [79]. However, it is during operation that
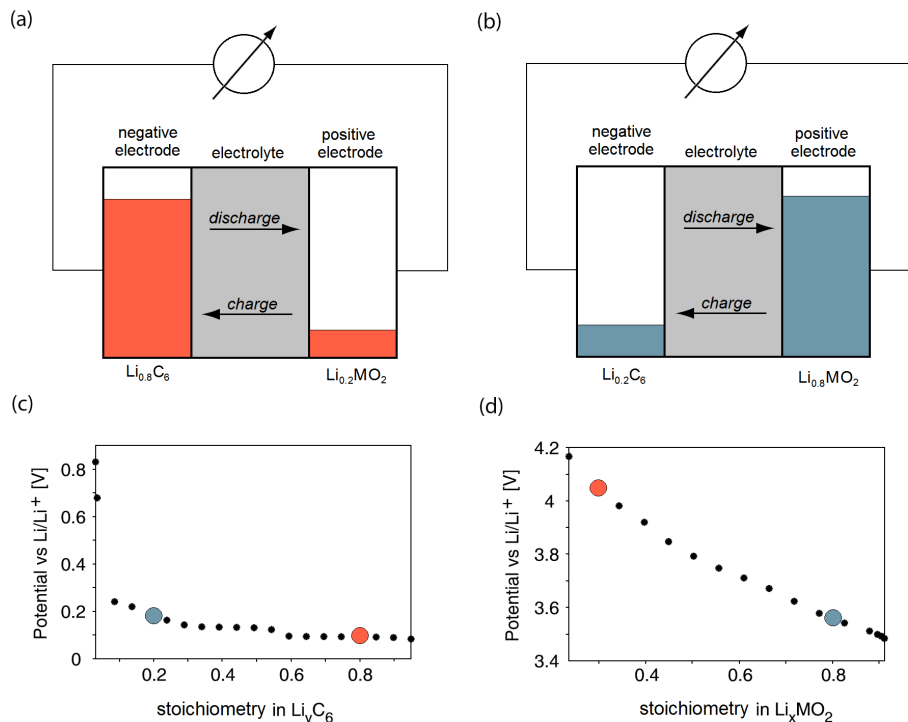
Figure 3.1: Schematic showing the relation between battery State-of-Charge and residual lithium concentration in anode and cathode at (red) 80% SoC and (blue) 20% SoC [2]

vehicle engineers wish to estimate the remaining energy capacity to propel the vehicle. Ultimately, the vehicle should be able to provide up-to-date information about remaining drivable distance, which is to be dynamically updated depending on drive style, temperature and other factors. Sampling, sensing and subsequent parameter errors present a significant challenge in this field [80] and many examples of poor accuracy and reliability of SoC prediction are reported in the literature [81].

3.2 Tasks of the battery management system

Battery packs in automotive applications comprise many identical cells connected together to form a large power source. The complexity of such a system necessitates the prediction, management and control of each of the constituent cells by means of a Battery Management System. The aim of the BMS is to maximise individual cell usage while mitigating cell degradation. This is achieved by continuously adjusting each cell's operating point to an optimum condition. The function of a BMS in automotive applications is multifaceted but of particular importance are the following tasks:

(A) Cell performance state prediction aiming to quantify the following during operation:

  · **Cell capacity** refers to the total available capacity of the cell under consideration of its cycling history. It represents the reference point for State-of-Charge estimation and tends to decline over the cell's live-cycle due to various forms of degradation.

· **State-of-Charge** is the percentage of the residual battery capacity in its present state compared to the maximum rated capacity available [82, 83, 84, 85]. The residual capacity of the cell is directly related to the amount of lithium concentration in the anode and the cathode, which is also called the stoichiometric state. A comparison of the stoichiometric state and SoC for a cell at 80% SoC and at 20% SoC is shown in Figure 3.1. Accurate SoC prediction is essential in achieving optimised energy usage and maximum driving range.

The most simplistic SoC prediction algorithms utilise look-up tables with previously stored data on SoC (possibly also as a function of temperature) [86, 87, 88]. SoC is not only a function of voltage but also of may other factors (such as charge-discharge rate, temperature, hysteresis and self-discharge), which means the the size, accuracy and complexity of these look-up tables can render such models unsuitable for online performance prediction [89]. The prediction and monitoring of causes of cell degradation make this estimation problem even more complex. Rapid assessment of state of charge is especially important in high power batteries in order to prevent the battery being over-charged or over-discharged during high power, short duration events. Failure to do so results in highly accelerated aging. In such applications, coulomb counting is often used in addition to look-up tables with algorithms used to determine when the additional use of look-up tables is most likely to produce more reliable results.

· **State-of-Function** refers to a battery's ability to deliver a certain amount of energy or power under the prevailing operating conditions; also referred to as the 'cranking' ability. This power or energy availability measure is essential in managing the storage device together with other components in the vehicle, for example an engine. The immediately available power must be estimated as it forms an important input for the vehicle supervisory control to determine the propulsion options available to the driver. Battery SoF is particularly important in hybrid applications where decisions must be made by the vehicle control system on which sources of power will be used at a given instant to satisfy driver demand.

· **State-of-Health** is a concept describing the general condition and cell history of a battery and its ability to deliver the specified requirements. The concept of state-of-health is much talked about in industry but usually ambiguously or not defined. State-of-Health (SoH) concerns battery degradation and relates cell performance to the nominal (rated) and end (failure) states [90], given its usage history [91, 92]. It has been shown that certain operating conditions significantly contribute to the deterioration of performance of the cell, such as discharge/charge rate, temperature, overcharge and over-discharge [93, 94, 85]. The resulting degradation due to these aforementioned operating conditions is detectable in the form of changing charge/discharge characteristics. Ultimately, the cell responds differently over time to the same load. Control engineers accordingly have to account for these changes and ensure the updating of the 'new' battery performance characteristics. In order to avoid significant changes in battery performance, battery manufacturers recommend pre-defined operating conditions and safe usage envelopes, outside of which battery characteristics become too difficult or even statistically impossible to predict. Within these bounds manufacturers are confident that battery performance evolution and remaining lifetime can be predicted over the cell's lifetime.

· **Remaining Useful Life** (RUL) is a derivative of the SoH prediction, and denotes the estimated remaining life-time of the battery under the current operating conditions before the available capacity has fallen below a certain End-of-Life (EoL) threshold.

(B) Cell performance state monitoring is essential in order to re-adjust the battery operating point towards its optimum operating point within the Safe Operating Area (SOA). This is in order to maintain the maximum possible RUL under the characteristic operating conditions in the long run and the optimum SoF given a specific operating condition. In order to do so, several parameters are continuously monitored and readjusted:

· **Discharge current** is related to the internal ionic current between the electrode pairs. Diffusion limitations in the mass transport of ionic species in a battery and thermal safety boundaries limit the instantaneously available current.

· A **temperature** increase during operation results from several heat generation sources. Lithium-ion batteries have been shown to be particularly sensitive to temperature, which can cause a significant acceleration of degradation processes. In particular, excessive temperatures can lead to an acceleration of the electrochemical reaction processes, resulting in even more heat being generated; a process called thermal runaway. If uncontrolled, this is a very dangerous phenomenon, which can lead to leakage of electrolyte, fire and even explosion of the cell. On the other hand, if a cell is operated at very low temperatures the electrochemical kinetics is reduced, which leads to locally excessive species concentrations and can potentially cause lithium plating at the electrode surfaces.

· **Cell terminal voltage** depends on the cell SoC and establishes due to the difference between anode and cathode electrical potentials. Battery over-charge leads to an excessively large concentration of lithium in the anode while over-discharge leads to an excessively large concentration of lithium in the cathode. This in turn leads to a sharp increase in cell impedance as the already full electrode opposes further intercalation; finally leading to lithium plating on the electrode surfaces.

3.3 Technical capabilities of the Battery Management System

In assessing battery performance algorithms for automotive applications, the technical capabilities of commercial BMS system have to be considered. The platform consists of complex measurement electronics and master controllers containing various monitoring algorithms. Voltage, current and temperature are parameters which may be measured at cell level, cell string level or pack level, depending on system complexity, cost constraints and accuracy requirements. Their respective sampling rate is crucial in accurately predicting cell response to dynamic phenomena at small time-scales. Since cost is a critical

Requirements	Examples of fundamental requirements
Functional requirements	Real-time prediction capability through high-speed computation; transmission of large volumes of data; scalability for modular battery system (series/parallel configuration, from light to heavy duty commercial vehicles); adaptability to different chemistries
Diagnostic requirements	Monitoring of safety-related functions; diagnostic capability at service station; monitoring of the relevant driving safety functions;
Economic requirements	Maintainability, re-usability due to adaptation; memory optimized code; modular design; long life cycle;
Organisational requirements	Development across distributed locations; modular framework; traceability of faults

Table 3.1: Important requirements for BMS computation platform specifically in automotive applications [11, 12]

design criterion in commercial systems, a trade-off between cell-level monitoring (more accurate/more expensive) and string- or pack-level (less accurate/less expensive) sensor positioning has to be considered. This is a problem particularly for automotive applications with many thousands of cells (e.g. Tesla S with pack sizes containing up to 7104 cells).

It has been reported that commercial automotive sensors provide voltage measurements at an accuracy range between $10\,\mathrm{mV}$ to $30\,\mathrm{mV}$ at sampling rates of $0.1\,\mathrm{s}$ (limited also by the Controller Area Network (CAN) transmission rate) [11]. The accuracy of current measurements poses a greater challenge. Current is most commonly measured using hall sensors or current shunts, the latter with the safety implication of not being physically separable from the current paths. The shunt characteristic resistance causes a potential drop and therefore heat generation, whereby reducing the overall pack energy efficiency. Hall sensors represent a non-invasive alternative, albeit being a more expensive and temperature-dependent component and requiring regular re-calibration. Their accuracy is limited especially at low currents. For these reasons current shunts are implemented much more frequently.

The increase in requirements on battery state prediction is not matched by a growth in on-line computing power and memory. This gives rise to the need for lean prediction algorithms, reduced-order models and the avoidance of complex iterative solution procedures, which inherently require computational power. The functional, diagnostic, economic and organisational requirements on the BMS computation platform are summarised in Table 3.1. A more detailed assessment of the state-of the-art in BMS designs is not part of the scope of this work. Rather, focus in this thesis is the development of the battery model.

3.4   Components of the Battery Management System

The on-board vehicle energy system is complex as several sub-systems are coordinated, monitored and controlled simultaneously at a low error margin and at low computational power. The software environment containing the on-board real-time running battery model is the Battery Monitoring Unit, nested within the Battery Management System. The BMU is a microprocessor unit incorporating a self-updating battery model and a decision logic module.

· The **computational model of the battery** consists of the battery model and the state predictor. Its task is to simulate SoC, SoH, SoF and RUL given measured values of current, voltage and temperature at discrete time steps. This is done either on a cell level, but can also be in a more lumped method for cell strings and other cell arrangements. Different degrees of sophistication in the prediction capabilities exist, depending on the degree of electrification of the vehicle. Depending on the prediction algorithm, the battery performance parameters are updated iteratively upon the arrival of new data samples. Central to the battery performance estimator is the battery state-of-charge prediction which is a topic of particular interest in the battery performance literature. In reviews by Piller *et al.* and Pop *et al.* common methods are presented, namely [95, 96, 97, 89].

  Empirical/Tabulated data relationship models - the comparison of measured terminal voltage to pre-determined thresholds and look-up tables.

  Equivalent circuit models - the emulation of overall cell behaviour by equivalent circuit elements.

  Electrochemistry models - the solution of the electrochemical equations governing the physical processes occurring in the cell.

· The **decision logic module** contains an algorithm comparing the output provided by the battery state predictor are pre-defined allowable operating states. The decision logic module readjusts the battery operating point towards its optimum. It furthermore provides error messages to the Battery Control Unit (BCU) and initiates shut down and other safety procedures. It is programmed to drive the system in a loop towards recommended operating envelopes, cut off regimes, temperature limitations, and safety boundary conditions.

Central to the monitoring and control of the battery is the actual battery model. Several different methodologies are adopted in industry. The different models relevant to automotive applications are discussed in Chapter 4 where they are assessed against the design criteria laid out in Chapter 1.

3.5   Interim conclusion

This chapter presented several important functions and features of modern Battery Management Systems. Sampling, sensing, subsequent parameter errors and the lack of suitable

battery models have been identified as a significant challenge in this field while this thesis focusses on addressing the software-related shortcomings of commonly implemented battery performance prediction algorithms. Hardware-related problems and solutions have been the focus of other researchers' work and are beyond the scope of this thesis.

Chapter 4

Battery modelling

Overview

Various battery models, previously presented in the literature, are discussed in this chapter. Rather than discussing the technical details of each, emphasis is placed on their strengths and weaknesses to single out successful attempts at phenomenological descriptions. Particularly those methods most suitable for modelling lithium-ion battery performance in automotive applications are presented. Strengths and limitations in terms of output accuracy/speed, parametrisation and solution procedure are discussed.

Finally, the capabilities of the most advanced phenomenological equivalent circuit models are assessed against the proposed design criteria (from Chapter 1), to segregate specific areas of further development. These form the basis of the development of the new model in Chapter 5.

4.1   Introduction

Predicting battery performance has been a focus of research for a long time. The main challenge faced is that batteries are electrochemical devices exhibiting complex, non-linear behaviour which depends on a multitude of internal and external factors.

There are many different kinds of models achieving different degrees of accuracy at different levels of complexity. Although these models are commonly presented as alternatives achieving the same goal, they are derived from different principles, require different parametrisation methodologies and deliver different levels of high-fidelity of outputs. An overview of the states and parameters of particular interest to automotive energy management and a typical information flow between the these parameters within the BMS is shown in Figure 4.1.
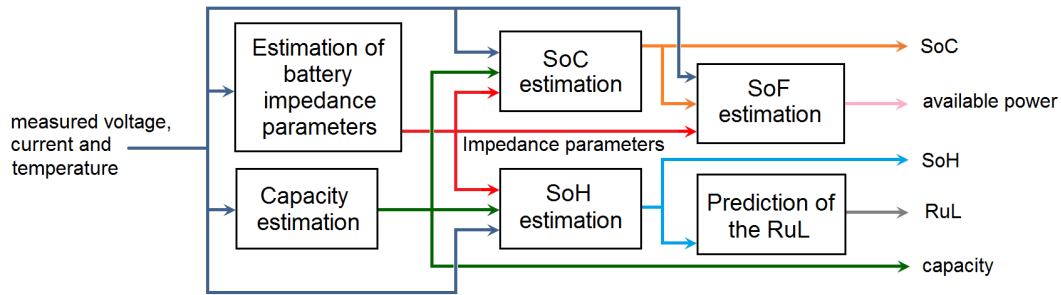
Figure 4.1: Schematic showing the state prediction information inter-relations [4]

The aim of all battery performance prediction tools is to establish a quantified relationship between a set of input parameters (V, I, T) and a set of output parameters, where the information depth of the output in turn depends on the chosen battery model. The process of relating an input to a predicted output requires numerical computation of the relation in form of a transfer function, be that on a vehicle BMS or on a computer. The relation between input and output can also be defined directly using pre-stored data, which then takes the form of a multiplication matrix. This approach masks the electrochemical phenomena inside the cell and only mimics overall cell voltage behaviour during operation.

When discussing different battery models, researchers often distinguish between analytical solutions of electrochemical models, direct measurement methods, book-keeping methods and Electrochemical Impedance Spectroscopy parametrised Equivalent Circuit Models (ECNs).

4.2 Electrochemical models

The electrochemical modelling efforts of researchers in the field of Li/Li-ion battery systems are commonly based on the isothermal electrochemical model developed by Doyle *et al.* [98] for galvanostatic discharge. A macro-homogeneous porous electrode theory approach, developed in 1972 by Newman [99] shown in Figure 4.2, to describe the potential variations in the solid and solution phases was adopted by Gomadam [100]. In this model the material balance in the solution phase is described using concentrated solution theory and in the solid phase using a Fickian diffusion equation in spherical coordinates (Figure 4.2). The details of this model will be discussed in detail in Chapter 5 as this forms the fundamental basis of the newly proposed phenomenological equivalent circuit model.

Confining only to isothermal conditions, Doyle validated this model by demonstrating good agreement with experimental data [101]. Later, Pals and Newman [102], Song and Evans [103] and Wang *et al.* [104] extended this model to include an energy balance in order to predict cell temperature under non-isothermal conditions. Pals and Newman [102] used an average heat generation method while Song and Evans [103] and Gu [104] used local heat generation terms, including ion diffusion, dissipation, buoyancy, ion production and consumption. An electrochemical-thermal model using local heat generation terms has been shown to be more accurate [100] and includes all the features of the isothermal model developed by Doyle *et al.* [98] as well as the additional energy balance included by Song and Evans [103] and Gu [104]; however, this accuracy comes at the cost of
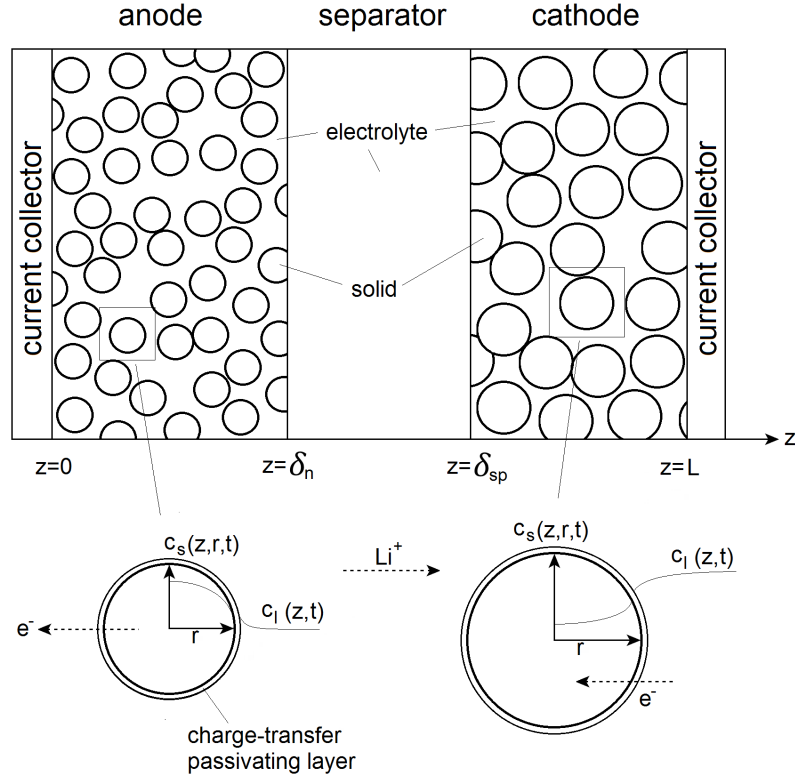
Figure 4.2: Doyle/Newman pseudo 2D single-particle model

requiring more computing power and time. Due to the high computational demands, the challenging parametrisation requirements and the low simulation speed these kinds of models and derivatives thereof [105, 106] are valuable for system optimisation and BMS design prior to implementation but too complex for in-situ operation.

Simplifications of the full electrochemical model have been proposed to overcome the challenges of solution speed for systems integration. One of these is the consideration of only surface Li$^+$ concentration and average bulk concentration in the solid phase to determine the remaining battery capacity using the Polynomial approximation Particle model (PP) [107]. Dao *et al.* further reduced simulation complexity by approximating electrolyte phase concentration gradients by applying Galerkin's method [108]. Electrode and electrolyte over-potentials were then obtained, assuming a constant current density as a function of concentration within the respective phase. The Single Particle (SP) and Multi-Particle (MP) models are recognized as a further approximations of the complex nature of the materials involved, whereby assuming sponge-like structures made up of spheres of solid phase material containing the active species [109, 110]. The major implication of this model is that the electrolyte phase concentration gradients and resulting potential changes are negligible, making this model unsuitable for high C-rate applications, and that the concentration in the solid phase can be approximated by a parabolic profile. [109, 110]

4.3 Empirical law/tabulated battery models

Fully discretised and coupled electrochemical models are far too complex, computationally expensive and difficult to parametrise for on-board automotive battery performance prediction. For this reason, the most commonly implemented battery performance estimation algorithms are based on empirical relationships of input and output given certain operating conditions and constraints [5]. These empirical models are simplistic representations which run much faster, although at the expense of accuracy. These models do not include knowledge of the underlying thermodynamic and electrochemical phenomena. Model variants based on empirical relations are therefore unable to predict time-dependant cell chemistry-related behaviour, thermal and degradation effects. Furthermore, the output of these kinds of models is only valid at the operating conditions at which the original parametrisation dataset was obtained making them unsuitable for advanced battery performance prediction. Several such models are presented in the following.

4.3.1 Peukert equation

One of the first empirical models was presented by W. Peukert in 1897, who developed a model relating cell capacity of a lead-acid battery to the rate of discharge [111]. The Peukert equation describes the dependence of battery discharge capacity on applied current with Peukert's coefficient C as

$$C = \mathrm{K}I^{1-\mathrm{n}},\tag{4.1}$$

where I is the actual discharge current and n and K are experimentally obtained constants based on maximum discharge current I_1 over discharge time t_1 and minimum discharge current I_2 over discharge time t_2, according to

$$\mathrm{n} = \frac{\ln\left(\frac{t_2}{t_1}\right)}{\ln\left(\frac{I_1}{I_2}\right)},\tag{4.2}$$

and

$$\mathrm{K} = I_1^{\mathrm{n}}t_1 = I_2^{\mathrm{n}}t_2.\tag{4.3}$$

Peukert, followed by other researchers, demonstrated that the available cell capacity decreases when increasing the discharge current by using different lead-acid batteries of various capacities and shapes. The unsuitability of Peukert's equation for chemistries other than lead-acid was demonstrated by Chan *et al.* [112]. However, Doerffe and Sharkh, [113] aimed to disprove Chan's conclusions by applying the methodology to lithium-ion batteries, although only for constant current discharge tests.

One limitation to the Peukert equation is that it is mathematically indeterminate for small currents and changing current direction, which means current direction changes cannot be represented by this function. Researchers have since modified this method for non-constant discharge rates by proposing a cumbersome solution with different fitted Peukert coefficients over pre-determined SoC ranges [114] .

Han *et al.* proposed an adaptive Kalman Filter for SoC estimation in conjunction with a Peukert equation, which was extended by He *et al.* for SoC predictions in automotive applications [115]. Although formulation improvements have been made [116], models based on this methodology still suffer the significant drawback of being only valid for the specific operating conditions for which they were parametrised. It is extremely time intensive to populate the required look-up tables containing a depth and variety of operating conditions and state combinations required to make reliable state predictions, especially in automotive applications.

4.3.2   Shepherd model and Tremblay implementation

The Shepherd model is popular in automotive battery estimators and commonly implemented in combination with a Peukert equation-based estimator to predict cell voltage under a varying load. Battery terminal voltage is obtained as: v

$$V_{\text{bat}} = V_{\text{const}} - K_i Q - R_{\text{bat}} I_{\text{bat}}, \tag{4.4}$$

where V_{const} is a constant potential, for example taken to be the voltage of the battery when fully charged in [V], R_{bat} is the ohmic resistance of the cell in [Ω], K_i is the polarisation resistance in [Ω] and Q is the discharged battery capacity in [Ah]. The cell ohmic resistance is defined empirically as:

$$R_{\text{bat}} = R_0 + K_{\text{R}} + K_{\text{R}} \frac{1}{1 - Q}, \tag{4.5}$$

where the total battery ohmic resistance is composed of R_0, the internal battery resistance at full charge, K_{R} the electrolyte resistance at full charge and the ratio of amount of discharged capacity Q to full battery capacity. The problem of algebraic loops in the solution of the Shepherd equation with only SoC as a state variable was addressed by Plett *et al.* in [117, 118]. Building on their approach, O. Tremblay investigated different cell chemistries in addition to incorporating voltage dynamics effects under varying loads and Open Circuit Voltage as a function of State of Charge [5]. He aimed to provide a straightforward procedure for extracting battery characteristic parameters from the manufacturers supplied discharge curve for populating the simple model. This ease of parametrisation ultimately led to the adoption of this model as a basic building block representing a battery in Matlab/Simulink.
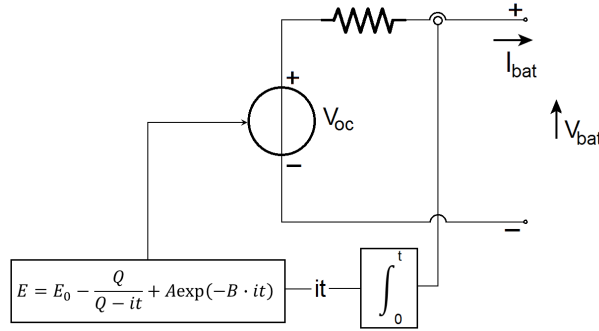
Figure 4.3: Battery model as proposed by Tremblay [5]

This type of circuit has been implemented for example in [119, 120] to investigate power generation systems using lithium-ion battery grid storage. The exponential dependence on State of Charge was further developed by Tofighi and Kalantar [121] who replaced it by a series resistance and short and long transient dipoles, achieving improved dynamic response time and lower simulation overshoots.

However, several limitations reduce the applicability of the Shepherd methodology for automotive implementation. Firstly, the internal resistance of the cell is assumed constant during charge and discharge as well as independent of charge/discharge rate. Furthermore, results are highly depended on the accuracy of the supplied charge/discharge curve. This renders this model unsuitable for dynamic and high C-rate applications where detailed electrochemical parameter evolution is of interest. Fundamentally, this model is not based on the electrochemical behaviour of the cell but rather emulates the cell voltage given a load input.

4.4 Semi-empirical models

Direct measurement methods enable the evaluation of battery performance parameters which are part of the live input parameter set from measurable physical properties (voltage, current and temperature). These methods are the intermediate step between the live battery measurements and the actual transfer function relating measurable battery characteristics to immeasurable performance indicators. These measurement methods form the basis of semi-empirical models.

4.4.1 Open Circuit Voltage based models

The Open Circuit Voltage (OCV) method assumes a predictable relationship between SoC and OCV. It therefore represents a very simple, fast SoC prediction methodology. An example for a recently published advanced form of OCV-SoC estimation is given in Equation 4.6 [122].

$$\begin{aligned}
\mathrm{OCV}(z) \;=\;\; & \mathrm{K_0} + \mathrm{K_1}\frac{1}{1 + e^{\alpha_1(z-\beta_1)}} + \mathrm{K_2}\frac{1}{1 + e^{\alpha_2(z-\beta_2)}} + \mathrm{K_3}\frac{1}{1 + e^{\alpha_3(z-\beta_3)}} \qquad (4.6) \\
& + \mathrm{K_4}\frac{1}{1 + e^{\alpha_4(z-\beta_4)}} + \mathrm{K_5}z
\end{aligned}$$

Where variable z represented the State of Charge, $\mathrm{K_{0\sim5}}$ are linear parameters, and $\alpha_{0\sim4}$ and $\beta_{0\sim4}$ are non-linear parameters. As can be seen, this equation establishes an empirical relation between OCV and State of Charge. Similar functions have prior to this been published by Chen *et al.*, Hu *et al.*, Plett *et al.* and Szumanowski [123, 124, 125, 126].

A significant drawback rendering this method impractical for automotive applications is the required long rest periods to obtain an OCV measurements. Reduced rest periods may result in inaccurate predictions as the cell may not having fully returned to equilibrium conditions. For some cell chemistries with large hysteresis effects, such as $LiFePO_4$, the cell might never return to an equilibrium condition. Moreover, the relationship between SoC and OCV is highly dependent on chemistry (and usually not linear!), temperature, C-rate and many other factors; making this method often unreliable. The implementation of look-up OCV-SoC data obtained under multiple operating conditions in the algorithm yields a more computationally expensive solution than other methods presented in the following, while only resulting in an interpolated, performance prediction [127].

As previously, it is a major shortcoming of this methodology that the battery is treated entirely as a 'black box' and no information can be obtained about any fundamental electrochemical processes allowing a detailed control of the battery.

4.4.2 Electromotive force based models

The Electro-Motive Force (EMF) of a cell relates to its thermodynamic state, which changes over its SoC range. The cell thermodynamic state defines cell characteristics such as open circuit voltage, charge transfer overpotential, diffusion limitations and relaxation time [128]. Unterrieder *et al.* recently demonstrated an SoC prediction methodology based on forecasting OCV during discharge [129, 130]. Basing their approach on electrochemical impedance measurements, Waag and Coleman *et al.* [131, 6] have presented derivative methodologies for EMF prediction.
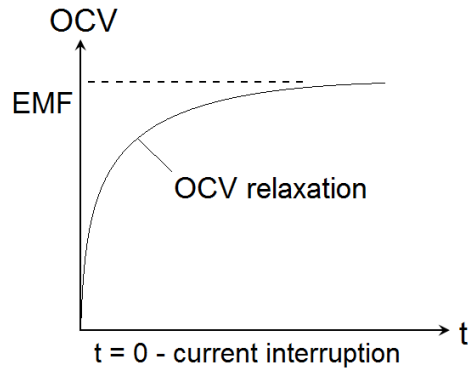
Figure 4.4: Schematic showing EMF voltage relaxation towards OCV upon load removal [6]

This method relates the time taken for the terminal voltage to reach open circuit potential due to the cell EMF at a certain SoC, as shown in Figure 4.4. Again, this method approximates the system as a black box and only relates the ultimate output, SoC, to input parameters current, voltage and temperature. No true prediction of SoH or any intrinsic variable evolution indicating degradation can therefore be inferred.

4.4.3 Book-keeping based models

Book-keeping methods refer to current measurements and integration of 'the charge passed over a time interval'. It is therefore also referred to as 'coulomb-counting'. The accuracy of the resulting SoC prediction is dependent upon temperature, battery history, C-rate and cycle life [132]. With previously stored experimental data, several phenomena occurring during the life of a battery can be empirically compensated for by applying ageing correction factors.

Book-keeping methods are usually combined with OCV measurements during resting periods to reset and refine the initial SoC measurement upon which the following in-operando predictions are based.

4.5 Equivalent Circuit Network models

Equivalent circuit models are a visual and intuitive variant of battery models which make them a popular choice for control engineers without expert knowledge of the electrochemical processes of a battery. They aim to reproduce the voltage behaviour under load by replacing the mathematical laws of electrochemistry by electric circuit equivalents. An advantage of type of model is that battery performance can be simulated as part of the embedding circuit. These models range from 'lumped' networks to more sophisticated circuit networks. Examples of such models are presented in the following.

4.5.1   Passive elements circuit networks with voltage sources

The equivalent electronic network may, for example, consist of linear passive elements, such as resistors, capacitors and inductors, to account for the internal resistance of a cell [133]. Using only these parameters, an ECN model generally fails to describe the intrinsic battery performance states. In an attempt to account for these, various equivalent circuit models have been proposed, consisting of linear passive elements in combination with ideal voltage sources which are parametrised by interpolating pre-stored data of electrode potential; making this model strongly dependent on the quality of its a priori parametrisation [134, 135]. The complexity of coupled phenomena under real-life operating conditions means that it is unlikely that the voltage source is able to emulate cell behaviour accurately. Examples of circuits with pre-populated voltage sources are the RINT, RC and Thevenin model and further derivations thereof.

(A) The RINT model

The basic form of the RINT model was as first proposed by the Idaho National Engineering and Environmental Laboratory [136]. It consists of an ideal voltage source V_{oc}, populated by an empirical battery open-circuit voltage data table and an internal resistance R_0, both functions of temperature. A potential difference between the cell terminals reflects the terminal voltage V_{bat} under application of a current I_{bat}.

The main limitations of the RINT model lie in its strong dependency on pre-populated look-up tables and the therefore limited applicability in real world dynamic operating conditions. The oversimplification of the electrochemical processes inside the battery and the lack of capacitive response of the system was demonstrated by Johnson *et al.* [137, 138].
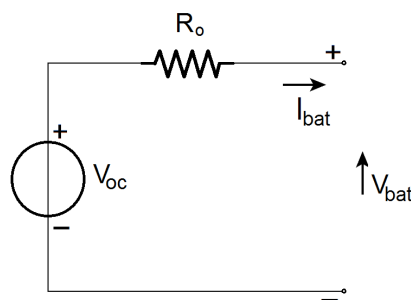
Figure 4.5: RINT equivalent circuit model example implementation

$$V_{\text{bat}} = V_{\text{oc}} - I_{\text{bat}} R_0, \tag{4.7}$$

(B) The RC circuit model

The RC circuit model, made popular by the company 'SAFT Batteries', combines capacitive and resistive elements to achieve battery characteristic behaviour under load. Two

capacitors and three resistors are arranged as shown in Figure 4.6. This model was created in the attempt of associating a physical meaning to each electric element. Electrochemical reaction capacitance (more specifically double-layer capacitance, which is discussed in Chapter 5) is represented by a small capacitor C_c. Remaining battery capacity in is represented by the 'bulk' capacitor C_b.
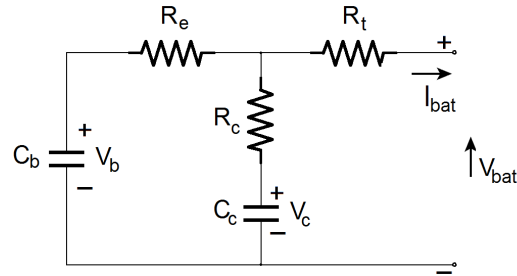
Figure 4.6: RC equivalent circuit model example implementation

Equation 4.8 represents the transfer function equivalent to the circuit model depicted in Figure 4.6.

$$[V_{\text{bat}}] = \left[\begin{array}{cc} \frac{R_c}{R_e+R_c} & \frac{R_e}{R_e+R_c} \end{array} \right] \left[\begin{array}{c} V_b \\ V_c \end{array} \right] + \left[R_t - \frac{R_e R_c}{R_e + R_c} \right] [I_{\text{bat}}] \tag{4.8}$$

Its implementation into the popular vehicle drivetrain modelling software ADVISOR [138] has contributed to the widespread use of this model. As with previous equivalent models in this chapter, the electrochemical processes are lumped, no distinction can be made between local processes and only the cell's overall voltage response is replicated.

(C) The Thevenin circuit model

The Thevenin circuit model takes the form of a parallel-series arrangement of constant resistor and capacitor elements. An ideal battery open circuit voltage source V_{oc} is arranged in series with internal resistance R_0 and a parallel couple, C_{th} and R_{th}, contributing transient capacitive response and polarisation overpotential resistance respectively.
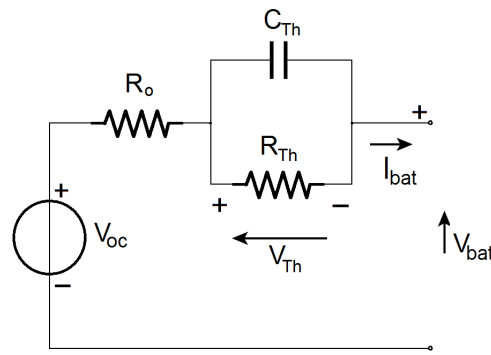
Figure 4.7: Thevenin equivalent circuit example implementation

This circuit can be written in the form of a transfer function as:

$$V_{\text{bat}} = V_{\text{oc}} - V_{\text{th}} - I_{\text{bat}} R_0, \tag{4.9}$$

where

$$V_{\text{th}} = -\frac{V_{\text{th}}}{R_{\text{th}} C_{\text{th}}} + \frac{I_{\text{bat}}}{C_{\text{th}}}. \tag{4.10}$$

Similar to the previously introduced models, the fundamental processes occurring during operation are masked, rendering this methodology unsuitable for the purpose of accurate battery state and degradation prediction.

4.5.2 Advanced equivalent battery modelling - state of the art

Significant contributions in the development of phenomenologically meaningful equivalent circuit were made by researchers such as Rael, Bergveld and Prada [139, 4, 140, 141]. Identifying that electrochemical analytical solutions of partial differential equations is not suitable for in-situ battery performance prediction, they developed modelling methodologies for equivalent circuit elements describing physical processes [4, 140, 139]. Their work therefore forms the starting point of the model development presented in this thesis. On the basis of the isothermal pseudo 2D battery mathematical model proposed by M. Doyle, T.F Fuller and J. Newman [98, 106] and extended by Smith and Wang [142], they aimed to describe the electrochemical phenomena in the cell given four basic unknown system variables: ionic concentration of the electrolyte c^{l} and the associated electrolyte potential ϕ^{l}, lithium concentration of each electrode c^{s} and the associated electrode potentials ϕ^{s}.

Several assumptions and simplifications limit the applicability of their model variants to low C-rate applications. For example, the model proposed by Rael *et al.* assumes isothermal conditions during operation [139], while the model proposed by Bergveld assumes a homogeneous temperature distribution throughout the model with no thermal gradients [4].

These models are limited to low charge/discharge rates not only because of heir isothermal or thermally homogeneous evaluation but these models do not, so far, account for diffusion limitations to mass transport in the electrodes and electrolyte and only have constant passivating layer resistances and double-layer capacitances.

This means that the model predicts an immediate availability of intercalated lithium partaking in electrochemical reactions, whereby overestimating power capability. These factors contribute to the inability of these models in predicting highly dynamic and high C-rate load cycles accurately.

A good attempt at establishing a physics based equivalent circuit was presented by Bergveld who developed a circuit system describing the thermodynamics and charge transfer kinetics [4]. He transformed the mathematical descriptions governing the physical

phenomena into electrical equivalents. However, a shortcoming of this model is that it does not allow for local temperature variations (and gradients), does not include a passivating or variable double-layers and does not account for any degradation features, such as capacity fade or power fade.

To the author's knowledge, Bergveld's work represents the best attempt at retaining physically meaningful individual circuit elements and circuit representations of governing electrochemistry equations in distinct domains. The mentioned simplifications render the proposed model, which was developed specifically for small portable electronics applications (low C-rate, continuous charge/discharge), unsuitable for highly dynamic automotive-type loads.

4.6   Adaptive system methods

To utilise the advantages provided by different methods and to arrive at a globally optimised estimation, several modelling methods may be combined into hybrid algorithms. The objective is to arrive at superior estimation efficiency and accuracy as compared to the individual estimation algorithms [143, 97, 144]. Various adaptive systems enhancing the accuracy of state predictors have been developed for this purpose. These were implemented in an iterative loop with the battery model in order to refine its parameters continuously.

One popular variant is the combination of coulomb-counting with the EMF method. Pop *et al.* implemented this real time estimator, which combines a direct measurement of EMF of the battery during rest periods to set the initial SoC with coulomb-counting during charge/discharge which builds upon the initial rest SoC value. He introduced a simple empirical correction factor which accounts for degradation by adjusting the model parameters.

Wang *et al.* [144] proposed another type of hybrid method in combining coulomb-counting with a Kalman filter, in a methodology he termed 'the Kalman Ah method'. In this method, a Kalman filter is applied to the initial SoC value, which is used for the subsequent coulomb-counting procedure. By ensuring this initial convergence to the true SoC value, Wang achieved an average SoC estimation error of 2.5% as compared to an average estimation error of 11.4% when using only the standard coulomb-counting method [144].

Finally, Kim and Cho applied an Extended Kalman Filter (EKF) and a per-unit (PU) system to a battery model parameter estimation algorithm in order to track SoC evolution as a function of cell-life [143]. In their model, parameters are empirically adjusted by a 'degradation' factor.

In this active research field, further variants of adaptive system methodologies have been coupled to battery models and include back propagation (BP), neural networks [145], radial basis functions (RBF), fuzzy logic methods [146], support vector machine strategies [147], fuzzy neural networks [148, 149] and various derivatives of Kalman filters [147, 87, 148, 88, 117, 150, 125, 151].

4.7 State-of-Health estimators

In order to assess on-line battery performance deterioration for each consecutive cycle, several methods have been proposed. An easily and cheaply implementable method is the comparison of discharged capacity (through coulomb-counting) for the same cut-off voltage with previous cycles. This measure quantifies SoH as the amount of remaining capacity of the cell as compared to the first cycle. A drawback of this method is the requirement of comparable charging/discharging conditions allowing the comparison between cycles during rest periods. This means this method is unable to provide continuously updating SoH predictions.

Sauer *at al.* distinguishes three methodologies for degradation modelling [152]: physical-chemical processes modelling, coulomb-counting with weighting to adjust for degradation during adverse operating conditions, and a special event-oriented concept that utilizes pattern recognition to identify severe operation conditions. The drawback of the proposed detailed physical-chemical model is the dependence on a specific cell chemistry, extensive parametrisation with experiments and considerable computational power requirements, which make it unsuitable for on-line evaluation. The coulomb-counting method is based on an empirical degradation readjustment factor which means this model treats the ageing process, again, as a "black-box" problem. Similarly, the adverse pattern recognising algorithm requires extensive testing of the proposed adverse operating conditions. Not only will the resulting forms of degradation be dependent on the operating conditions under which they occur but also on the characteristics of the cell used in collecting the parametrisation data.

Many methods have been proposed in the literature but there is disagreement over which forms of degradation exist, what the underlying causes are and how these are related [91, 153, 154]. A majority of the proposed models relate experimental data obtained under idealistic operating conditions and simple load cycles to calendar life estimations [155]. Such models may rely on statistical or mathematical methods [146, 156, 157] or are established on the basis of semi-empirical correlations [158].

In automotive applications SoH is often estimated from a single measurement of either cell impedance or cell conductance [125]. One proposed approach is the formulation of a weighted function of SoH of several cell parameters, all of which vary with cell age [90]. Capacity fade as an important aspect of SoC has been investigated by Bhangu *et al.* [159], who employed an extended Kalman filter, estimating capacity loss due to a reduction in the bulk capacitance. Do *et al.* [160] combined a modified Randles circuit with extended Kalman filter in a real-time identification method. In doing so the number of additional RC-pairs resulted in divergence issues and overly optimistic results, as well as yielding an equivalent circuit model containing circuit elements with no physical meaning.

4.8 Commercial automotive implementations

A common form of battery performance prediction is shown in Figure 4.8. It has to be noted that when implementing such an estimation procedure, limitations and errors arise

from the different sampling rates of current, voltage and temperature. This is due to the fact that all these parameters are communicated to the BMS on the Controller Area Network bus (CAN-bus) where parts of each piece of information is lined up in successive 'packages' along one single information path rather than in parallel information channels. Online measurements obtained at the same time therefore do not necessarily arrive at the BMS at the same time, leading to estimation error [11].

The most commonly implemented SoC models are based on the coulomb-counting method combined with OCV-SoC look-up tables, allowing a recalibration of the initial SoC estimate during rest periods [161]. The accuracy of coulomb counting based models depends on the quality of live measurements on the vehicle during operation. Most commonly, current is obtained via a voltage measurement across a shunt resistor connected in series with the battery system, which is then converted into a current reading [161]. To reduce losses in the power drawn from modern automotive battery packs the shunt resistors are becoming substantially smaller resulting in a much smaller voltage drop across and therefore larger rounding errors. The measurement accuracy and sampling rate of this shunt resistor voltage is the principal source of inaccuracies in methods based on coulomb counting [161].

A common implementation example is depicted in Figure 4.8. In this example an online optimisation algorithm is applied to calculate SoC and SoH by continuously reiterating several empirical cell characteristic parameter functions: nominal capacitance $C_n = f_1(SoC, T, SoH)$, series resistance $R_s = f_2(SoC, T, SoH)$, parallel resistance $R_p = f_3(SoC, T, SoH)$, and parallel capacitance $C_p = f_4(SoC, T, SoH)$.

$$\frac{dSoc\,(t)}{dt} \quad = \quad \frac{I_{\text{bat}}\,(t)}{C_{\text{n}}} \tag{4.11}$$

$$\frac{dV_{\text{p}}\,(t)}{dt} \quad = \quad -\frac{V_{\text{p}}\,(t)}{R_{\text{p}}C_{\text{p}}} + \frac{I_{\text{b}}\,(t)}{C_{\text{p}}} \tag{4.12}$$

$$V_{\text{bat}}\,(t) \quad = \quad OCV\,(t) - V_{\text{p}}\,(t) - R_{\text{s}}I_{\text{b}}\,(t) \tag{4.13}$$

$$SoH_{\text{c}}\,(t) \quad = \quad \frac{C_{\text{n}}\,(t)}{C_{\text{n}}\,(0)} \tag{4.14}$$

$$SoH_{\text{p}}\,(t) \quad = \quad \frac{R_{\text{s}}\,(0)}{R_{\text{s}}\,(t)} \tag{4.15}$$
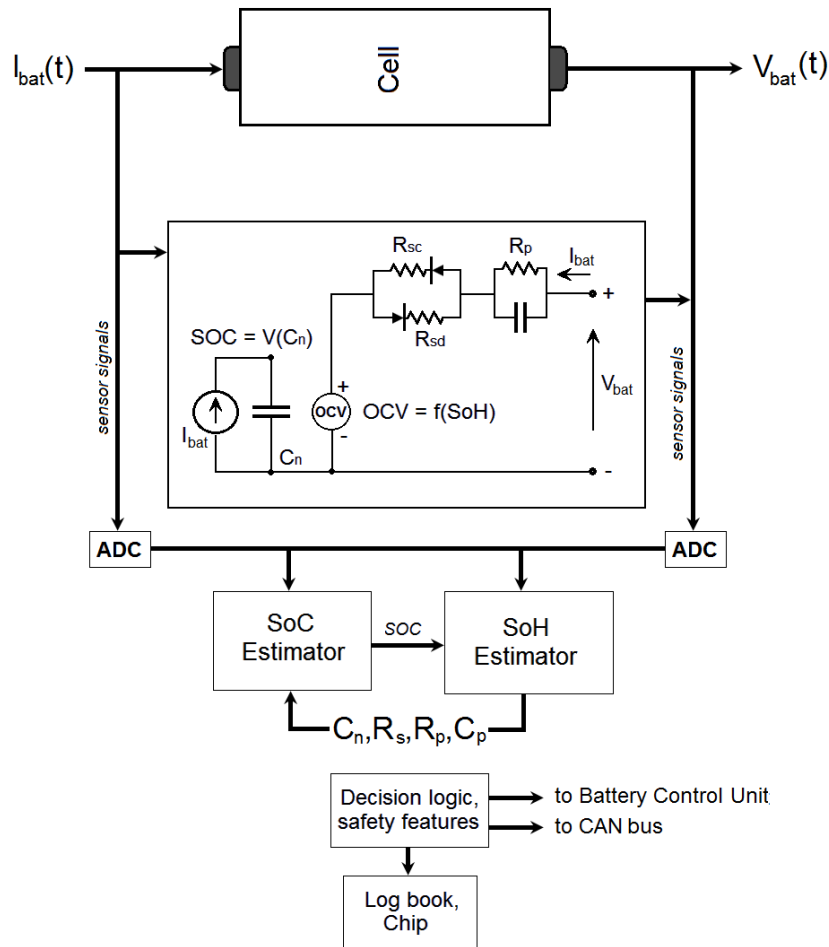
Figure 4.8: Example of an online parameter iteration algorithm implementation with nested SOC and SoH estimator

Again, this method masks the ion algorithm implementation with itlex electrochemical processes inside the cell and no insight is possible into the individual physical processes. Therefore, such a model does not suffice for advanced battery management control algorithms where more fundamental performance states are required for precise control of the battery.

4.9   Model parametrisation methods

4.9.1   Charge/discharge pulse test produces

Researchers exploring simple equivalent circuits commonly employ current pulse tests, such as the HPPC (Hybrid Pulse Power Characterisation procedure [136]) and various other pulse current discharge tests, to parametrise their models. While helpful in quantifying relative changes in comparison to previously collected parameters, the depth of information on the cell to be extracted using these procedures is very limited and sufficient only for very simple equivalent circuit models.

4.9.2   Electrochemical Impedance Spectroscopy

Electrochemical Impedance Spectroscopy (EIS) is a powerful tool which can be used to investigate the characteristic behaviour of a cell. A cell impedance measurement generally involves the excitation of the cell with a known electrical stimulus (current or voltage), and measuring the electrochemical system response to this perturbation (voltage or current, respectively). A commonly used procedure, shown in Figure 4.9a), is the application of a single-frequency sinusoidal signal (although other excitation signal shapes can be used [162]), and the subsequent measurement of the phase and amplitude of the resulting signal.

The resulting impedance measurement is a complex ratio of stimulus and response measurement as a function of frequency. The response may be presented in the form of Bode plots (magnitude versus frequency and phase angle versus frequency) or Nyquist diagrams (imaginary versus real part). Information can be deduced on several intrinsic electrochemical properties, such as internal impedance, diffusion and charge transfer characteristics.

An example of this is shown in Figure 4.9b). Impedance response is recorded as a lumped cell response of anode and cathode, whereby summing the effect of various internal characteristic processes. This makes the distinction of anodic and cathodic contributions and the attribution of frequency ranges to individual phenomena challenging. By conducting half cell experiments, the cell overall impedance response can be distinguished into the separate responses of cathode (Figure 4.9c) and anode (Figure 4.9d). Different physical processes of (I) series resistance with respect to the reference electrode, (II) double-layer and charge-transfer phenomena and (III) diffusion phenomena of lithium-ion through the electrolyte and of intercalated lithium through each electrode material are represented by shaded regions in Figures 4.9c) and 4.9d). Such half-cell data is only accessible by measuring impedance with respect to a third (reference) electrode. The insertion of such an electrode, however, means a disturbance of the cell structure and can lead to a distortion of the cell's impedance response. As can be seen, each electrode contributes different amounts of impedance along the scanning frequency range; a feature which is masked completely when testing the complete cell. The fact that electrochemical phenomena cannot always be distinguished as originating from anode or cathode presents a limitation to the usefulness of this technique. The processes occurring inside the cell differ and therefore have to be accounted for separately for meaningful performance prediction. In-situ measurement of battery EIS is impractical in automotive applications as well as most portable battery systems, an very accurate frequency sweep signal has to be applied and a very accurate measurement of the system response recorded in order to compute meaningful system impedance data.

4.10   Interim conclusion

State-of-Charge and State-of-Health prediction is an active research field both in academia and industry. While some researchers aim to arrive at a performance estimate from previously collected data given similar operating conditions, others arrive at state estimations
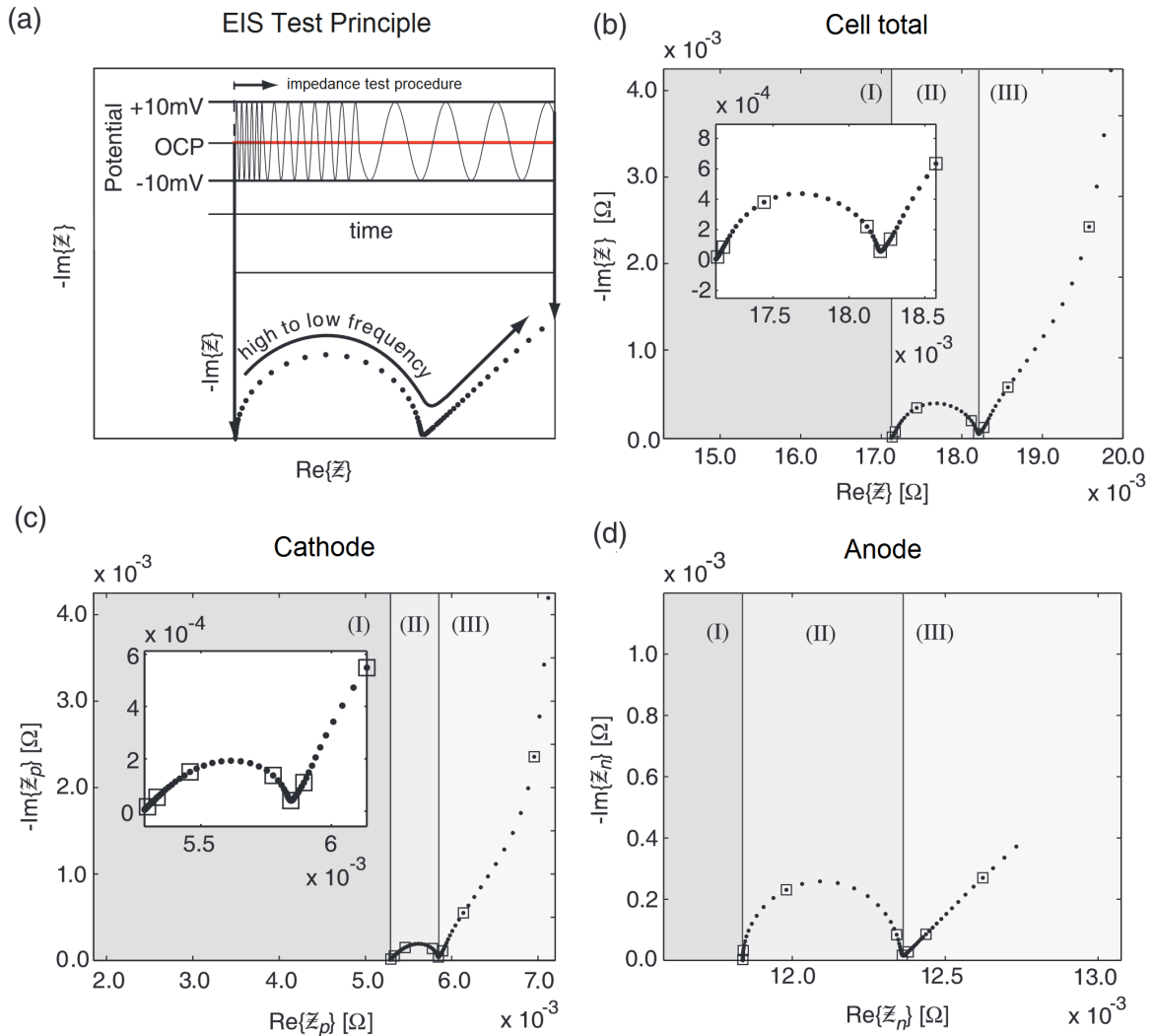
Figure 4.9: (a) Schematic describing the process of EIS given a sinusoidal signal. Each dot in the figures represents an impedance measurement at a different frequency (b) example whole cell impedance response, (c) positive electrode impedance contribution and (d) negative electrode impedance contribution). Several electrochemical phenomena are indicated: (I) series resistance with respect to the reference electrode, (II) intercalation phenomena (e.g. charge transfer, double-layer) and, (III) diffusion of lithium-ion in the electrolyte and of intercalated lithium in the solid electrode; modified from [2]

via complex mathematical modelling of the internal electrochemical processes. The objective of all estimators is to provide accurate and useful information on states as quickly to the control unit managing the battery. The effectiveness of the methods presented above depends, amongst other things, on the reliability and timeliness of the measurement data serving as the input to the model. In the following, the state-of-the-art modelling methodologies are assessed against the design criteria for the new equivalent circuit model.

When revisiting the design criteria laid out in Chapter 1, it becomes clear from the description of the various models above that none completely satisfy the design criteria.

· <u>Electrochemical models</u>, although representing the electrochemical processes and phenomena most accurately, are too computationally expensive for on-board battery performance prediction. Even reduced-order models thereof still require the iterative numerical solution of mathematical equations, which requires large amounts of computational power. The extension of full electrochemical analytical models with the required additional physical phenomena associated with cell degradation increases the computational cost even further.

· <u>Empirical</u> and <u>semi-empirical model</u> based estimations, on the other hand do not provide the required depth of information required to accurately predict electrochemical phenomena occurring during operation. They mimic the overall cell response to a load, which prohibits the evaluation of detailed processes associated with degradation.

· In the field of <u>advanced Equivalent Circuit Models</u>, some significant steps have been taken towards unifying the electrochemical phenomena encapsulated in full electrochemical models and the benefits of simplifying the system in an ECN approach. However, many of the desired features of the model as well as degradation mechanisms have not been included in previously presented models.

In assessing the capabilities of the most advanced phenomenological equivalent circuit models against the proposed design criteria (Chapter 1), the following areas of further development remain which will be addressed in Chapter 5.

1. Structuring the model into clearly defined physics based sub-circuits governing individual species' phenomena

2. Derivation of an equivalent circuit element governed by electrochemical reaction process phenomena which links the individual circuits

    (a) allowing for locally variable passivating layer thickness, resistance and capacitance, depending on local electrochemistry and temperature

    (b) allowing for locally variable double-layer capacitance and potential, depending on local electrochemistry and temperature

3. Extension of previous work in phenomenological equivalent circuit modelling by including thus far excluded phenomena

---

    (a) allowing for local temperature and the subsequent dependency of local electrochemical processes

    (b) allowing for capacity fade through loss of cyclable lithium and for power fade through increase of internal impedance

4. Removal of any empirical dependencies in the model

5. Coupling of all phenomenological analogies to local heat generation

6. Structuring of the model in the form of a visual representation/layout of the network and ability to extend to aid future adaptation/modifications/extension and system-level implementation by system engineers

A more detailed table with a literature assessment may be found in the Appendix.

Chapter 5

The new Equivalent Circuit Model

Overview

This chapter presents the derivation of the new phenomenological equivalent circuit model. The underlying thermodynamic and electrochemical principles are discussed allowing the derivation of the the final equations for electrochemical and electrical potentials and other physical processes which are implemented in the model. A distinction is made between the electrical modelling domain, which includes the species circuit networks governing the charged species (lithium-ions and electrons) in electrolyte and external circuit respectively, and the chemical modelling domain, including the species circuit network governing uncharged intercalated lithium inside the electrodes.

The significance of electrochemical driving forces leading to a (useful) electrical cell potential are discussed and the contribution of various overpotentials to a reduction in useful cell potential examined.

Subsequently, a methodology for representing the electrochemical reaction process in a single electrical element is presented. This link is introduced in the form of the Triple Species Element and serves as the connection between the electrical and the chemical domains, linking the three separate transport circuits of electrons, intercalated lithium and lithium-ions in the electrode and the electrolyte domain respectively. This element is also shown to account for various overpotentials during operation which are significant in predicting local inefficiencies and the onset of degradation.

Species transport in the electrodes and electrolyte are thereafter discussed and the expressions for circuit elements derived, allowing a phenomenological representation of the entire system. The model is locally coupled to a thermal model, allowing for local heat generation at each discretisation in the system. Furthermore, expressions for circuit elements representing variable double layers and passivating layers on each electrode surface are derived.

Finally, degradation mechanisms in the form of capacity and power fade are included as features of this new model.

5.1   Operating principle in detail

The operating principle of lithium-ion batteries, which was already briefly discussed in Chapter 3, is the same for all chemistries, although electrode materials, electrolyte and other composites may vary, and cell geometric designs might be optimised for specific applications. In principle, an electrochemical cell provides a potential by electrically harnessing the difference between electrochemical potentials of anode and cathode.

Both electrodes in the system are electronic conductors, each with an electrical potential, ϕ_i, due to the electrochemical potential, $\bar{\mu}_i$, of lithium stored in it. As a design feature, the chemical potential μ_i of the intercalated anode is always larger than that of the cathode. The resulting difference in chemical potentials between the electrodes acts as the driving force for electrochemical reactions, enabling spontaneous de-intercalation of Li^+ from the anode and intercalation into the cathode when the external circuit is closed. This electrochemical driving force is present when the cell terminals are connected, as the cathode chemical potential is always below that of the anode, even when the cell is fully discharged. Uncontrolled (spontaneous) discharge due to cell shorting must therefore be avoided. The useful battery electric potential results from the difference in electrical potentials between the electrodes and is called the cell open circuit potential V_{oc}.

Upon discharge the anode which is at a higher chemical potential μ_a than the cathode μ_c, releases lithium-ions Li^+ into the electrolyte, thereby increasing its electrical potential ϕ^a towards equilibrium with respect to Li/Li^+. These lithium-ions move to the cathode, towards the more favourable thermodynamic state (with lower chemical potential); the cathode electrical potential ϕ^c of which is therefore decreased. The resulting ionic flux from anode to cathode in turn occurs simultaneously to an electron (e^-) flux in the external circuit. This discharge process is illustrated in 5.1. The process of absorbing a lithium-ion into an electrode is referred to as intercalation or lithiation, while the process of releasing a lithium-ion into the electrolyte is called de-intercalation or de-lithiation.
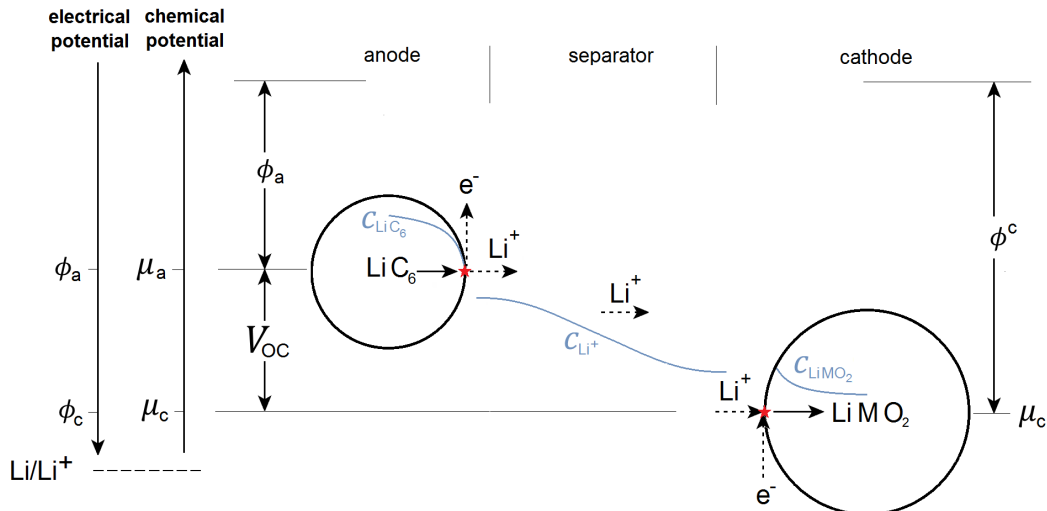
Figure 5.1: Schematic describing the discharge process with lithium oxidation occurring at the anode and Li^+ reduction taking place at the cathode. Here, each electrode is represented by a single sphere, while radii might differ between the two materials. Dotted lines: reaction product/reactant; blue lines: concentration gradients; red star: reaction site.

Figure 5.2: Overview of modelling domains, species networks and phases in the system, at an electrode/current collector interface; the porous electrode is represented by a multitude of spheres

5.2 Potentials driving electrochemical reactions

As discussed in Section 5.1, the operating principles of a lithium-ion cell are defined by electrochemical and electrical potentials. As a potential is applied to the terminals the intercalated lithium participates in electrochemical reactions and ionic and electron fluxes establish. Different potentials and resulting overpotentials result during these reduction and oxidation reactions. Figure 5.2 shows the regions in which electrical potentials apply and the regions where electrochemical potentials apply. It can be seen that, as soon as a intercalated lithium has de-lithiated from an electrode it becomes a species with electrical charge (i.e. a negatively charged electron or a positively charged lithium-ion) while the intercalated lithium inside the particles represent an uncharged species.

5.2.1 Electrochemical potentials

The ***chemical potential*** μ_i in $[\text{J mol}^{-1}]$ of a species i is a measure of energy of a chemical depending on its activity and its ***standard chemical potential***, also called redox potential μ_i^0 in $[\text{J mol}^{-1}]$. Deviations of activity a_i away from its equilibrium condition a_i^{eq} in $[\text{mol m}^{-3}]$ are encapsulated in the ***activity chemical potential*** term. The standard electrochemical potential is independent of the applied charge but is a function only of temperature and pressure. It can be considered a material energy property.

$$\mu_i = \mu_i^0 + \text{R}T \ln \left(\frac{a_i}{a_i^{\text{eq}}} \right), \tag{5.1}$$

where R is Boltzmann's constant in $[\text{J mol}^{-1}\text{K}^{-1}]$ and T is temperature in $[\text{K}]$.

Peter Debye and Erich Hueckel predicted that an activity a_i is proportional to the species concentration c_i in $[\text{mol}\,\text{m}^{-3}]$ by a dimensionless activity coefficient γ (assumed to be unity throughout, which holds for ideal solutions of pure substances in condensed phases [163]). They assumed further that average species concentration is equal to its molar amount m_i in [mol] in the occupied control volume V_i in $[\text{m}^3]$, which allows the formulation of the activity Equality 5.2. This relation is important in the modelling of species concentrations at all locations in the system, which the final model has to be capable of.

$$a_i = \gamma c_i = \frac{\gamma m_i}{V_i} \tag{5.2}$$

As an electron flux establishes during cell operation, an electrical charge appears on each electrode. Each species therefore has an additional potential $z_i \text{F} \phi_i$, resulting in an overall **electrostatic potential.** It can be seen that the charged electrochemical potential term in equation 5.3 establishes due to an electrical charge with **electrical potential** ϕ_i on a species with valence z_i.

$$\mu_{e,i} = z_i \text{F} \phi_i, \tag{5.3}$$

and F is Faraday's constant in $[\text{C}\,\text{mol}^{-1}]$. The **electrochemical potential** $\bar{\mu}_i$ in $[\text{J}\,\text{mol}^{-1}]$ is defined as the sum of the chemical potential (Eq. 5.1) and the electrostatic potential (Eq. 5.3) due to a charge being present on the species. Equation 5.2 can be substituted for species activity in order to arrive at an expression for electrochemical potential of a polarised electrode as a function of local species concentration.

$$
\begin{aligned}
\bar{\mu}_i &= \mu_i + \mu_{e,i} \\
&= \mu_i^0 + \text{R}T \ln\left(\frac{c_i}{c_i^{\text{eq}}}\right) + z_i \text{F} \phi_i,
\end{aligned}
\tag{5.4}
$$

where Equation 5.4 can be expressed for all species participating in a reaction at each reaction site. Under the absence of a charge, there is no electrostatic potential ($\bar{\mu}_{e,i} = 0$) and after a sufficient rest period the system reaches equilibrium where each species concentration and activity locally reaches equilibrium values ($c_i = c_i^{\text{eq}}$, $a_i = a_i^{\text{eq}}$). Consequently, under equilibrium conditions, the electrochemical potential is therefore equal to the chemical potential.

The meaning of the terms in Equation 5.1 do not hold for electrons which have no 'chemical' activity. Simplifying the principles of atomic physics of electron density a constant electrochemical potential is assumed for electrons which is independent of charge density.

From the described nature of the potentials the following can therefore be summarised for the three species involved in a lithium-ion battery insertion system: intercalated lithium, lithium-ions and electrons:

· for a <u>charged</u> species in a <u>non-equilibrium</u> system: $\bar{\mu}_i = \mu_i^0 + RT \ln\left(\frac{a_i}{a_i^{\mathrm{ref}}}\right) + z_i F \phi_i$ Applies to intercalated lithium, lithium-ions (not electrons, which have no activity).

· for an <u>uncharged</u> species in a <u>non-equilibrium</u> system: $\bar{\mu}_i = \mu_i + RT \ln\left(\frac{a_i}{a_i^{\mathrm{ref}}}\right)$ Applies to intercalated lithium, lithium-ions (not electrons, which have no activity).

· for an <u>uncharged</u> species in <u>equilibrium</u>: $\bar{\mu}_i = \mu_i$ Applies to intercalated lithium, lithium-ions and electrons.

· for the special case of <u>electrons</u> $\bar{\mu}_{e^-} = \mu_{e^-} - F\phi_{e^-}$ as a concentration formulation does not apply there.

5.2.2 Species reactions and interactions

A lithium-ion battery provides a useful electrical potential by harnessing the change in electrochemical potentials during reactions. These reactions take place due to favourable thermodynamic energy states which provide the driving force to electrochemical reactions. Since these are directly related to the electrical potential of each electrode in the system, they represent the link between chemical domain and electrical domain. The equations presented in this section arrive at the building blocks of the equivalent circuit model, and therefore their meaning, significance and calculation is discussed in detail here.

The change in electrochemical potentials of the reacting species represents the driving force of a spontaneous reaction and is also referred to as the ***change in free electrochemical energy*** $\triangle\bar{G}$ of a reaction in $[\mathrm{J\,mol^{-1}}]$. Like in any energy-cascade system a reaction will only occur if it is thermodynamically favourable, meaning only if the electrochemical potential of the oxidised species is lower than that of the reduced species. If a reduction reaction reaction (= at the cathode) during discharge is considered, the change in potential of the reduced lithium-ions and electrons must be greater than that of the intercalated lithium for the reaction to occur spontaneously. At the same time, an oxidising (delithiation) reaction (= at the anode), will only occur if it is thermodynamically favourable i.e. if the electrochemical potential of the intercalated lithium is greater than that of the lithium-ions and electrons combined. Equation 5.5 illustrates this process at the hand of a reduction reaction at the cathode.

$$
\begin{aligned}
\triangle\bar{G}_{\mathrm{Red}} &= \bar{\mu}_{\mathrm{Red}} - (\bar{\mu}_{\mathrm{Ox}} + n\bar{\mu}_{\mathrm{e^-}}) & (5.5) \\
&= \mu_{\mathrm{Red}} - (\mu_{\mathrm{Ox}} + n\mu_{\mathrm{e^-}}) + \overbrace{z_{\mathrm{Red}}F\phi_{\mathrm{Red}}}^{0} - (z_{\mathrm{Ox}}F\phi_{\mathrm{Ox}} + nz_{\mathrm{e^-}}F\phi_{\mathrm{e^-}}) \\
&= \triangle G_{\mathrm{Red}} - (z_{\mathrm{Ox}}F\phi_{\mathrm{Ox}} + nz_{\mathrm{e^-}}F\phi_{\mathrm{e^-}})
\end{aligned}
$$

where $\triangle G_{\mathrm{Red}}$ is the ***change in free energy***, the valence of the oxidised species is $(z_{\mathrm{Ox}} = +n)$, that of the reduced species is $(z_{\mathrm{Red}} = 1 - n)$ and n the number of electrons

participating in the reaction. Recalling that $z_{e-} = 1$, charge neutrality in the electrolyte is therefore satisfied, such that $\sum_i z_i c_i = 0$. Substitution of these valence numbers into Equation 5.5 allows the reformulation of the change in electrical potential from the reduced to the oxidised species.

$$\triangle \bar{G}_{\mathrm{Red}} = \triangle G_{\mathrm{Red}} - (n\mathrm{F}\phi_{\mathrm{Ox}} - n\mathrm{F}\phi_{e-}) \tag{5.6}$$

As previously discussed, only the oxidising products (lithium-ions and electrons) have a charge, the former being transferred into the electrolyte and the latter being transported via the electronically conducting electrode additives and current collectors. This allows the substitution of the liquid (electrolyte) electrical potential ϕ^{l} for the oxidising product ϕ_{Ox} (i.e. lithium-ion) electrical potential and the substitution of electrode electrical potential ϕ^{s} for the electron potential ϕ_{e-}, resulting in Equation 5.7.

$$\triangle \bar{G}_{\mathrm{Red}} = \triangle G_{\mathrm{Red}} - \left(n\mathrm{F}\phi^{\mathrm{l}} - n\mathrm{F}\phi^{\mathrm{s}}\right) \tag{5.7}$$

The change in free energy $\triangle G_{\mathrm{Red}}$, which already emerged in Equation 5.5 denotes the change in electrochemical potential under the absence of a charge, while the change in free electrochemical energy is evaluated under the presence of a charge. Their difference is therefore the potential difference across the electrode/electrolyte interface $n\mathrm{F}\left(\phi^{\mathrm{l}} - \phi^{\mathrm{s}}\right)$ due to the applied potential.

$$n\mathrm{F}\left(\phi^{\mathrm{l}} - \phi^{\mathrm{s}}\right) = \triangle G_{\mathrm{Red}} - \triangle \bar{G}_{\mathrm{Red}} \tag{5.8}$$

which can be expanded to allow the observation of chemical potentials μ_{Red}, μ_{Ox} and μ_{e-} which is important for the later implementation of diffusion limitations of these species (see Section 5.3).

$$n\mathrm{F}\left(\phi^{\mathrm{l}} - \phi^{\mathrm{s}}\right) = \mu_{\mathrm{Red}} - \mu_{\mathrm{Ox}} - n\mu_{e-} - \triangle \bar{G}_{\mathrm{Red}} \tag{5.9}$$

he potentials in Equations 5.8 - 5.9 are visualised in the form of an equivalent circuit in Figure 5.3. The top diagram represents Equation 5.9. The chemical potentials are represented by capacitors as each can then effectively represent an electrically replenished chemical store of species at the reaction site which behaves capacitively. The expression for their capacitance is derived in Section 5.7. The change in free electrochemical energy $\triangle \bar{G}_{\mathrm{Red}}$ is represented by a voltage source as it represents a quantity resulting from the interaction of several species at the reaction site, leading to a reduction in useful interface potential difference. A double layer capacitor C^{dl} is arranged in parallel, which will be discussed in Section 5.6. Similarly, in the bottom half of Figure 5.3, Equation 5.8 is visualised, where the chemical potential contributions are lumped and therefore represented by a voltage source adopting their potential sum.

Figure 5.3: Equivalent circuit implementation of intercalation site chemical potentials and changes in free energy. Top figure: Equation 5.9, Bottom figure: Equation 5.8. Capacitances represent chemical potentials of individual species, voltage sources represent changes in free electrochemical energy of the reacting species. The direction of electrochemical reaction current (i.e. species flux J^{ch}) is shown. The units of all chemical potentials is [J mol^{-1}], while the unit of chemical flux is [mol s^{-1}]. Arrows indicate a positive direction of a potential

It can be seen that, once the charge on this system is removed (i.e. $J^{\text{ch}} = 0$) and equilibrium has been reached (no balancing between the lower branches and the double layer branches), there is no driving force for the species either to reduce or to oxidise, such that $\bar{\mu}_{\text{Red}} = \bar{\mu}_{\text{Ox}} + n\bar{\mu}_{\text{e}^-}$. This means that under equilibrium conditions the free electrochemical energy $\triangle \bar{G}_{\text{Red}} = 0$, which reduces Equation 5.7 to:

$$
\begin{aligned}
0 &= \triangle G_{\text{Red}} - n\text{F}\left(\phi^{\text{l}} - \phi^{\text{s}}\right) &\text{(5.10)}\\
\triangle G_{\text{Red}} &= n\text{F}\left(\phi^{\text{l}} - \phi^{\text{s}}\right)
\end{aligned}
$$

The electrical potential difference across the electrode/electrolyte interface is now only dependent on the chemical potentials of the intercalated species. This is analogous to the potential characteristics previously summarised at the end of Section 5.2.1.

The above energy relations are expressed at the hand of a reduction reaction at the cathode, which is defined as a reaction in the positive direction. Simultaneously, an oxidation reaction must occur at the anode, accepting lithium-ions into the electrode in order for the redox couple to be complete. This oxidation reaction therefore occurs in the opposite direction to the reaction at the reducing electrode, which manifests itself in a negative sign as shown in Equations 5.11 - 5.12.

$$
\begin{aligned}
\triangle G_{\text{Ox}} &= -\triangle G_{\text{Red}} &\text{(5.11)}\\
\triangle \bar{G}_{\text{Ox}} &= -\triangle \bar{G}_{\text{Red}} &\text{(5.12)}
\end{aligned}
$$

Analogous to Equation 5.8 the electrical potential difference across the electrode/electrolyte interface at the anode can be expressed as

$$
\triangle G_{\text{Ox}} - \triangle \bar{G}_{\text{Ox}} = n\text{F}\left(\phi^{\text{s}} - \phi^{\text{l}}\right), \tag{5.13}
$$

where the opposite direction of the reaction can be seen to result in a reversal in order of liquid (electrolyte) electrical potential ϕ^{l} and solid (electrode) electrical potential ϕ^{s}.

The change in free electrochemical energy during the reduction reaction on the cathode $\triangle G_{\text{Red}}$ and the oxidation reaction at the anode $\triangle G_{\text{Ox}}$ gives rise to a lithium-ion flux from the anode to the cathode. This is driven by the attraction towards the more electrochemically favourable intercalation state but also by lithium-ion and intercalated lithium concentration gradients which establish due to diffusion limitations. The chemical flux J^{ch} in $[\text{mol s}^{-1}]$, occurs at each electrode/electrolyte interface provided there is a driving force (i.e. a thermodynamically favouring change in free electrochemical energy) [73].

$$
J^{\text{ch}} = a_{\text{s}}\left(k_{\text{a}}\right)^{1-\alpha}\left(k_{\text{c}}\right)^{\alpha}\left(a_{\text{Ox}}^{\text{b}}\right)^{\alpha}\left(a_{\text{Red}}^{\text{b}}\right)^{1-\alpha}\left\{\exp\left(\frac{\alpha^{\text{a}}}{\text{R}T}\triangle\bar{G}_{\text{Ox}}\right) - \exp\left(-\frac{\alpha^{\text{c}}}{\text{R}T}\triangle\bar{G}_{\text{Red}}\right)\right\} \tag{5.14}
$$

Where $a_{\text{Red}}^{\text{b}}$ is the bulk activity of the reduced species, a_{Ox}^{b} is the surface activity of the oxidising species and α^{a} and α^{c} are the anodic/cathodic transfer coefficients (also called symmetry factor), where $(0 < \alpha^{\text{a}} + \alpha^{\text{c}} < 1)$. Equation

5.2.3 Electrical potentials

As mentioned previously, it is the difference in electrical potentials observed across the electrode/electrolyte interface at anode ϕ^{a} and cathode ϕ^{c} which ultimately provides a useful cell potential between the terminals.

> The electrical potential of the electrode in units of [V] is linked to its chemical potential in units of $[\mathrm{J\,mol^{-1}}]$ (which caused it) by a factor of $1/n\mathrm{F}$, where n is the number of electrons partaking in each reaction (in this thesis unity).

To prove this, the units of the individual products resulting in an electrical potential are segregated in equation 5.15.

$$\phi \;=\; \mu n^{-1}\mathrm{F}^{-1} \equiv \left[\frac{\mathrm{J}}{\mathrm{mol}}\right]\left[\frac{\mathrm{C}}{\mathrm{mol}}\right]^{-1} \equiv \left[\frac{\mathrm{J}}{\mathrm{C}}\right] \equiv [\mathrm{V}] \tag{5.15}$$

With the conversion factor one can retrieve further electrical equivalents to chemical quantities, such as the relation between electron flux (i.e. current) in units of [A] and ionic-flux (i.e. chemical species flux) in the units of $[\mathrm{mol\,s^{-1}}]$.

$$I = n\mathrm{F}J^{\mathrm{ch}} \equiv \left[\frac{\mathrm{C}}{\mathrm{mol}}\right]\left[\frac{\mathrm{mol}}{\mathrm{s}}\right] \equiv \left[\frac{\mathrm{C}}{\mathrm{s}}\right] \equiv [\mathrm{A}] \tag{5.16}$$

As previously mentioned, $\triangle \bar{G}_{\mathrm{Red}} = \triangle \bar{G}_{\mathrm{Ox}} = 0$ once the charge on a system is removed and equilibrium has been reached. This allows for the equilibrium electrical potential of each electrode to be expressed as a function of the change in free energy.

$$E^{\mathrm{eq}} = \frac{\left(\phi^{\mathrm{l}} - \phi^{\mathrm{s}}\right)}{n\mathrm{F}} = \frac{\triangle G_{\mathrm{Red}}}{n\mathrm{F}} = \frac{\triangle G_{Ox}}{n\mathrm{F}}, \tag{5.17}$$

which can be shown to have units of [V], given the units of the products of which it is comprised.

$$E^{\mathrm{eq}} = \triangle G_{\mathrm{Ox}}n^{-1}\mathrm{F}^{-1} \equiv \left[\frac{\mathrm{J}}{\mathrm{mol}}\right]\left[\frac{\mathrm{C}}{\mathrm{mol}}\right]^{-1} \equiv \left[\frac{\mathrm{J}}{\mathrm{C}}\right] \equiv [\mathrm{V}] \tag{5.18}$$

The electrode equilibrium potential E^{eq} depends on the instantaneous electrical operating conditions of the electrode as well as the transient electrochemical properties. In the following, the constituents of equilibrium electrode potential are explored for a reduction reaction at the cathode.

$$E^{\text{eq}} \;=\; \frac{\triangle G_{\text{Red}}}{n\text{F}}, \tag{5.19}$$

which allows for the expression of electrical potential difference across the electrode/electrolyte interface $\left(\phi^{\text{l}} - \phi^{\text{s}}\right)$ as

$$
\begin{aligned}
\left(\phi^{\text{l}} - \phi^{\text{s}}\right) \;&=\; \frac{\triangle G_{\text{Red}}}{n\text{F}} - \frac{\triangle \bar{G}_{\text{Red}}}{n\text{F}} \\
&=\; E^{\text{eq}} - \frac{\triangle \bar{G}_{\text{Red}}}{n\text{F}},
\end{aligned}
\tag{5.20}
$$

Equation 5.20 can be expanded to allow the observation of chemical potentials μ_{Red}, μ_{Ox} and μ_{e^-} which is important for the later implementation of diffusion limitations of lithium-ions and intercalated lithium (Section 5.3).

$$\left(\phi^{\text{l}} - \phi^{\text{s}}\right) \;=\; \frac{\mu_{\text{Red}}}{n\text{F}} - \frac{\mu_{\text{Ox}}}{n\text{F}} - \frac{n\mu_{\text{e}^-}}{n\text{F}} - \frac{\triangle \bar{G}_{\text{Red}}}{n\text{F}} \tag{5.21}$$

Analogous to Figure 5.3 one can visualise Equations 5.20 - 5.21 in the form of an equivalent circuit (shown in Figure 5.4), this time composed of electrical potentials, where capacitors denote separate species' electrical potential while voltage sources represent the overpotentials establishing during each reaction process. The direction of the electrical current is indicated.

The last term in Equations 5.21 is also referred to as the ***activation overpotential*** η^{act}. It represents an 'energy-hurdle' to be overcome in order to a reaction to take place. It is only present when an electrochemical reaction takes place and can be expressed according to Prada et al. [140]:

$$
\begin{aligned}
\eta^{\text{act}} \;&=\; \frac{\triangle \bar{G}_{\text{Red}}}{n\text{F}} = -\frac{\triangle \bar{G}_{\text{Ox}}}{n\text{F}} \\
&=\; \frac{\text{R}T}{\alpha n\text{F}} \ln\left(\xi + \sqrt{\xi^2 + 1}\right)
\end{aligned}
\tag{5.22}
$$

where

$$\xi = \frac{r_{\text{s}}}{6\varepsilon_{\text{s}} i^0 a_{\text{s}} \delta} I_{\text{bat}} \tag{5.23}$$
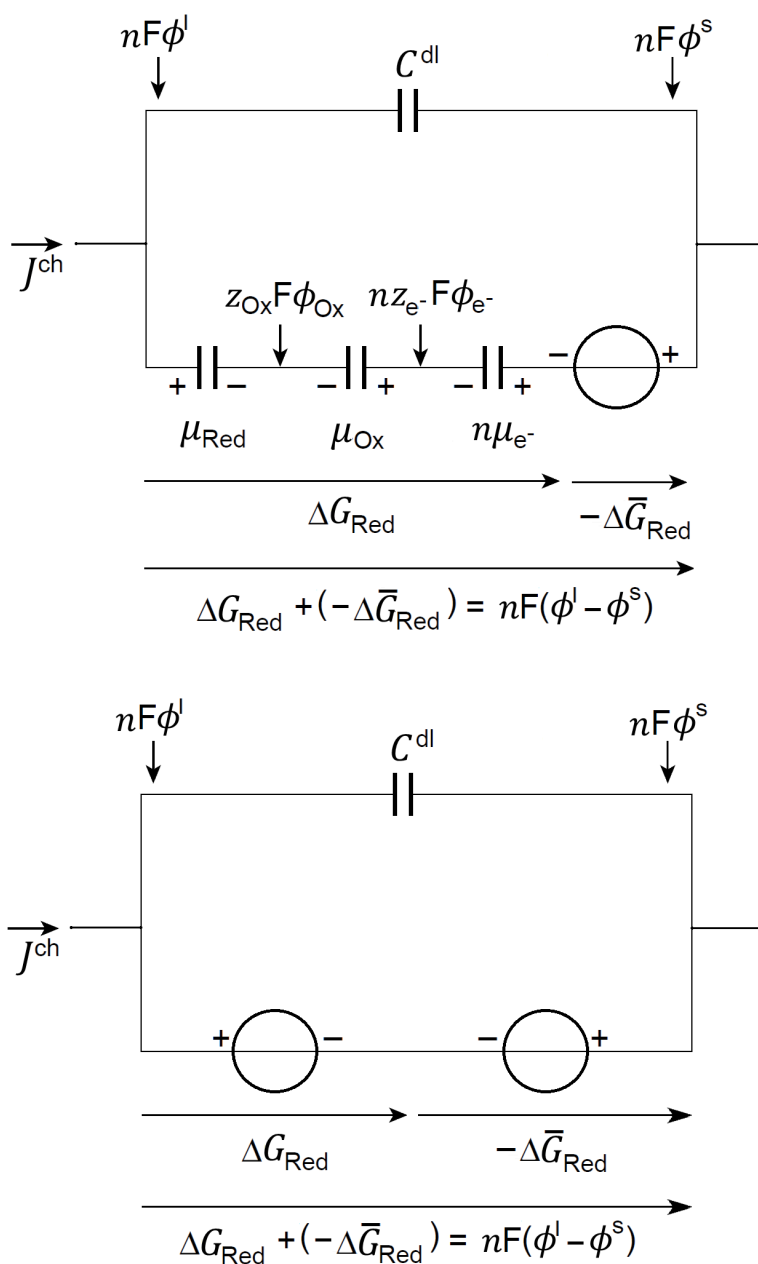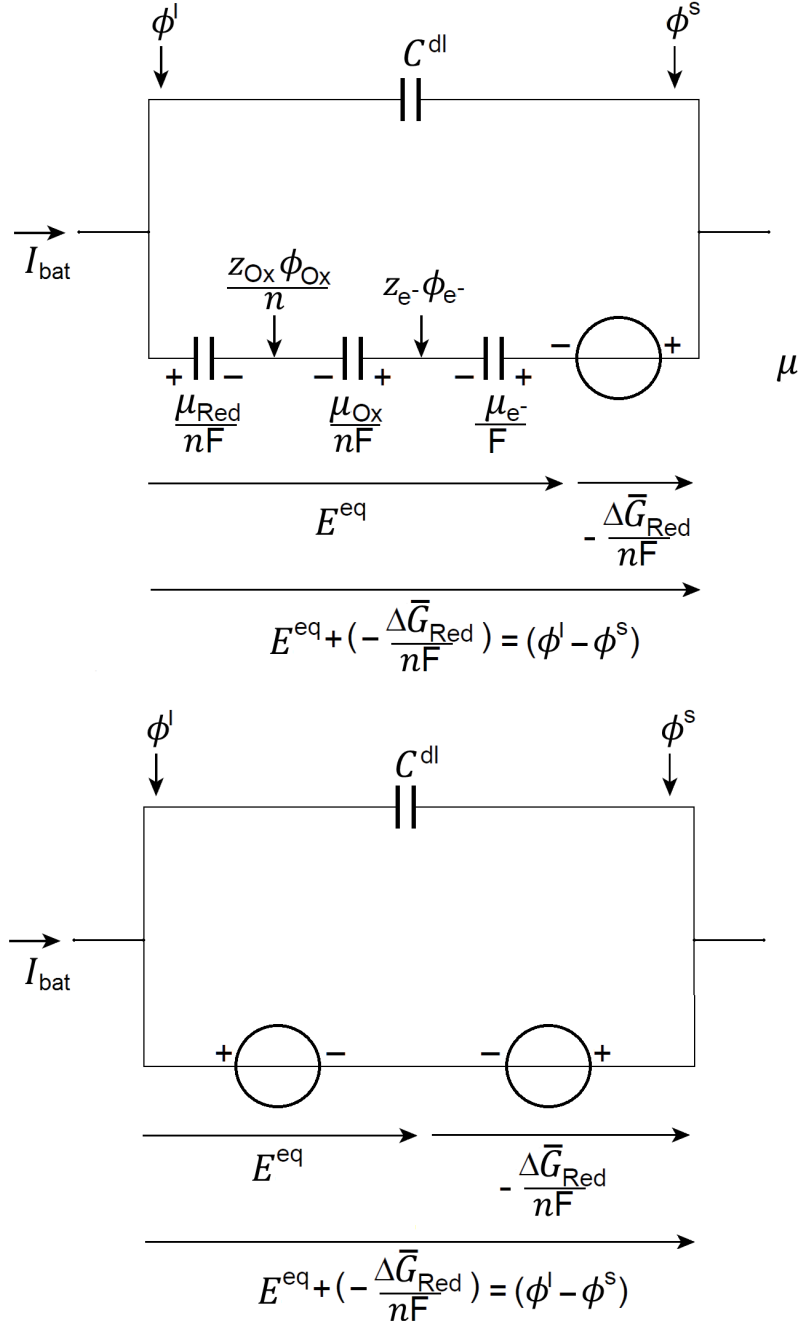
Figure 5.4: Equivalent circuit implementation of intercalation site electrical potentials and changes in free energy. Top figure: Equation 5.21, Bottom figure: Equation 5.20. Capacitances represent electrical potentials of individual species, voltage sources represent potential differences due to changes in free electrochemical energy of the reacting species. A double layer capacitor C^{dl} is arranged in parallel, which will be discussed in Section 5.6. The direction of electrical current I_{bat} is shown. The units of all electrical potentials is [V], while the unit of electrical current is [A]. Arrows indicate a positive direction of a potential

5.3 Lithium diffusion in the electrodes and electrolyte

In the following, the time dependencies of the above electrochemical and electrical quantities is discussed. Almost none are available instantaneously but experience a time delay due to mass and charge transport limitations. This is the reason for the dynamic response of a cell to varying loads and relaxation phenomena when the load is removed. It is therefore important to investigate their origin and to implement the associated phenomena in the model.

Since the species involved in the reactions have a mass and are physically diffusing through electrodes and electrolytes, limitations to mass diffusion have to be accounted for. In the following, diffusion overpotentials as part of the overall electrode potential are discussed during discharge. The oxidising species are therefore Li^+ and e^- while the reduced species is the intercalated lithium Li_i. As the lithium is reduced into the cathode, its intercalated lithium concentration increases. The notion of stoichiometry is used to quantify the ratio of concentration or activity of the reduced and oxidised species and can theoretically vary from complete lattice site occupation (at which $x_i = 1$), to complete lattice site vacancy (at which $x_i = 0$).

The stoichiometry x_i (or molar fraction) of the intercalation electrode i is a function of the ratio of activities of intercalated lithium a_{Li_i} and lithium-ions a_{Li^+}. Using the linear relation between activity and concentration (Equation 5.2) this ratio can be expressed in terms of concentrations of the reduced and the oxidised species.

$$
\begin{aligned}
x_i &= \frac{a_{Li_i}}{a_{Li_i} + a_{Li^+}} \\
&= \frac{c_{Li_i}}{c_{Li_i} + c_{Li^+}}
\end{aligned}
\tag{5.24}
$$

However, in practice only a range of stochiometries can be achieved for anode and cathode materials, depending on the capabilities of the lattice materials. This ratio is directly related to the electrode SoC such that

$$
SoC_i = \frac{c_{Li_i}}{c_{Li_i} + c_{Li^+}} \cdot 100
\tag{5.25}
$$

which is equal to the state of charge at the opposite electrode as mass has to be conserved in an ideal system. These quantities apply to the bulk, meaning the material deep within the electrode, which the intercalated lithium has to reach by diffusion. Limitations to diffusion of, both, intercalated lithium in the electrodes and lithium-ions in the electrolyte are critical to the power capability of a cell. These diffusion limitations define how quickly charge can be obtained from the cell, as Li^+ has to diffuse from the core of the host lattice to the surface to participate in the reaction and hence release an electron.

Due to these transport limitations, concentration gradients establish both inside the electrodes and the electrolyte, especially when high loads are applied. This results in local

Li$^+$ accumulation or depletion for short durations until the concentration gradient balances the local inhomogeneity. This means the bulk species properties may temporarily deviate from the surface properties where the intercalation process occurs. This local concentration non-equilibrium causes local surface activity variations, in turn causing a potential drop. Hence, under non-equilibrium conditions the apparent electrode potential is not equal the equilibrium potential, i.e. $\left(\phi^{\mathrm{l}} - \phi^{\mathrm{s}}\right) \neq E_i^{\mathrm{eq}} \neq E_i^{\mathrm{eq}*}$ and Equation 5.17 has to be modified to include surface activity properties rather than quantities relating to bulk properties.

It has been shown that these local concentration imbalances during lithiation and de-lithiation stem from electrical and elastic interaction forces between the Li$^+$ ions and the host atoms leading to phase changes. These have to be accounted for by including extra interaction energy terms [164]. The interaction energies are incorporated by including the term U_i, a dimensionless attraction energy coefficient inherent to the electrode material, resulting in the stoichiometry-<u>independent</u> interaction energy term $\mathrm{R}TU_i$ in [J mol^{-1}]. The addition of the term $\mathrm{R}T\zeta_i$ in [J mol^{-1}] allows for a stoichiometry-<u>dependent</u> interaction energy term [164].

$$E_i^{\mathrm{eq}} = E_i^0 + \frac{\mathrm{R}T}{n\mathrm{F}}\left[\ln\left(\frac{a_i^{\mathrm{s}}}{a_{\mathrm{Li}i}^{\mathrm{s}}}\right) - U_i x_i + \zeta_i\right] \tag{5.26}$$

The significance of the individual terms of this equation can be seen in Figure 5.5 at the example of a LiNi$_{1/3}$Co$_{1/3}$Mn$_{1/3}$O$_2$ cathode and a LiC$_6$ anode. The experimental data curve for the cathode was obtained as the difference of an 0.05 C discharge voltage measurement and the (graphite) anode equilibrium potential as obtained from Doyle *et al.*'s [165] empirical equation which is widely used in the literature and was derived with half-cell experiments. The empirical function for the cathode was derived via curve fitting of individual data points. The curve of electrode equilibrium potential with no interaction energy was obtained using the first two terms of Equation 5.26. The potential curve including attraction energy (i.e. including all terms of Equation 5.26) was fitted over distinct ranges of stoichiometry with the parameters given in Table 5.1.
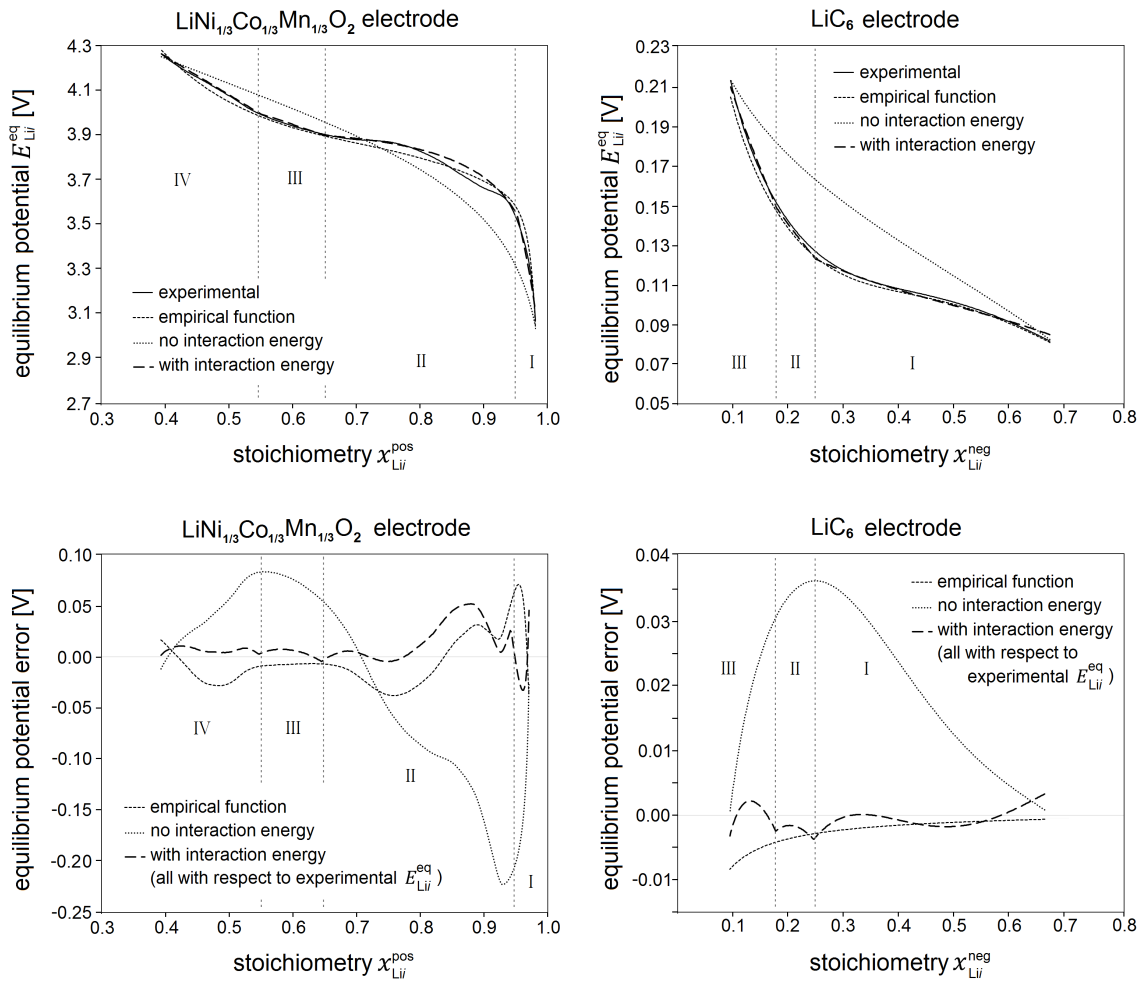
Figure 5.5: (a) LiNi$_{1/3}$Co$_{1/3}$Mn$_{1/3}$O$_2$cathode equilibrium potentials as function of stoichiometry, (b) LiC$_6$ anode equilibrium potentials as function of stoichiometry, (c) error of cathode equilibrium potential predictions as function of stoichiometry, and (d) error of cathode equilibrium potential predictions as function of stoichiometry, phases are indicated by Roman letters

	Phase	**Species**	
		Cathode	Anode
		$i = \mathrm{MO_2}$	$i = \mathrm{C_6}$
Standard redox potential [V]	$E^0_{\mathrm{L}ii}$	4.13	0.11
Stoichiometry-dependent interaction energy coefficient [-]	$U_{i,\mathrm{I}}$	6.0	-0.10
	$U_{i,\mathrm{II}}$	-1.0	0.10
	$U_{i,\mathrm{III}}$	-0.2	0.35
	$U_{i,\mathrm{IV}}$	0.6	
Stoichiometry-independent interaction energy coefficient [-]	$\zeta_{i,\mathrm{I}}$	5.95	-0.07
	$\zeta_{i,\mathrm{II}}$	-0.71	-0.02
	$\zeta_{i,\mathrm{III}}$	-0.19	0.03
	$\zeta_{i,\mathrm{IV}}$	0.25	
Phase-transition stoichiometry [-]	$x_{i,\mathrm{I}\to\mathrm{II}}$	0.95	0.25
	$x_{i,\mathrm{II}\to\mathrm{III}}$	0.65	0.18
	$x_{i,\mathrm{III}\to\mathrm{IV}}$	0.55	

Anode equilibrium potential equation [142]

$$
\begin{aligned}
E_{\mathrm{a}}^{\mathrm{eq}} =\ & 8.00229 + 5.0647 x_{\mathrm{a}} - 12.578 x_{\mathrm{a}}^{0.5} - 8.6322 \times 10^{-4} x_{\mathrm{a}}^{-1} + \\
& 2.1765 \times 10^{-5} x_{\mathrm{a}}^{1.5} - 0.46016 \times \exp\left(15 \times (0.06 - x_{\mathrm{a}})\right) - \\
& 0.55364 \times \exp\left(-2.4326 \times (x_{\mathrm{a}} - 0.92)\right)
\end{aligned}
$$

Cathode equilibrium potential equation

$$
\begin{aligned}
E_{\mathrm{c}}^{\mathrm{eq}} =\ & 6.45737 \times 10^9 x_{\mathrm{c}}^{1.5} - 7.72071 \times 10^9 x_{\mathrm{c}}^1 + 4.39471 \times 10^9 x_{\mathrm{c}}^{1.5} \\
& -9.69912 \times 10^8 x_{\mathrm{c}}^2 - 2.61703476 \times 10^8 x_{\mathrm{c}}^{-0.5} + 1.91844 \times 10^5 x_{\mathrm{c}}^{-2} \\
& +4.91232 \times 10^5 \times \ln\left(x_{\mathrm{c}}\right) - 1.38471 \times 10^7 \times \ln\left(x_{\mathrm{c}}^2\right) + 9.37309 \times 10^9 \times \ln\left(x_{\mathrm{c}}^{-1}\right) \\
& +1.21487 \times 10^6 \times \ln\left(x_{\mathrm{c}}^{-2}\right) + 3.00017 \times 10^7 \times \exp\left(x_{\mathrm{c}}\right) - 1.61690 \times 10^9 \times \exp\left(-x_{\mathrm{c}}\right) \\
& -3.89311 \times 10^4 \times \tan\left(x_{\mathrm{c}}\right) - 1.38662 \times 10^9
\end{aligned}
$$

Table 5.1: Parametrisation of Equation 5.26 for anode and cathode electrode equilibrium potential; subscripts I-IV stand for phases #I to #IV along the electrode potential curve as indicated in Figure 5.5

A smooth phase transition of the thermodynamics-based equilibrium curves (Equation 5.26) is ensured by the following relation between the stoichiometry-independent interaction energy coefficients of each phase j of each electrode i.

$$
\zeta_{i,j+1} = (U_{i,j+1} - U_{i,j}) \cdot x_{i,j\to j+1} + \zeta_{i,j} \tag{5.27}
$$

It can be seen from Figure 5.5 that several of the characteristic features of the experimentally obtained anode and cathode equilibrium potential curves are missing, especially in the curve of potential calculated from thermodynamic principles excluding the interaction

energy terms. Both the curve of potential calculated from thermodynamic principles including the interaction energy terms as well as the empirically fitted function are in much better agreement with the experimental potential curves. Phase transitions are visible as changes in slope on the equilibrium potential curves. For the equations including the attraction energy terms, these are known to be defined by specific stoichiometry ranges. The definition of distinct phases and transition points implies the following simplification: a species cannot present in two adjacent phases at any point [166, 164]; however, this implication is not only very difficult to experimentally verify but also unlikely to be accurate. The equilibrium potential errors of cathode and anode are shown in the second row of Figure 5.5 and are evaluated as the difference of the predicted and the experimentally obtained equilibrium potentials. It can clearly be seen that the thermodynamic calculation under the omission of the interaction energy terms yields the worst prediction. The reason for the discrepancy of the predictions under the inclusion of the interaction energy terms stems from the fact that there are, indeed, species co-existing in two phases, as was also investigated by Wu *et al.* [167]. The error of the prediction according to the fitted equilibrium potential equation originates in the number of terms used in the function. A higher number of terms naturally yields a better curve-fit, although not a better physical understanding of the underlying phenomena.

In order to avoid the piece-wise fit of equilibrium potential over the stoichiometric intervals, the continuous empirical function was preferred for implementation in the model. This decision is supported by the fact that this method is not only sufficiently accurate (see Figure 5.5) but also only requires a single low-rate discharge and one of the two electrode's empirical equilibrium potential equations from half cell experiments, commonly a carbon anode; the potential equation of which is readily available in the literature. The electrode/electrolyte interface electrical potential can now be expressed as

$$\left(\phi^{\mathrm{l}} - \phi^{\mathrm{s}}\right)_i = E_i^{\mathrm{eq*}} + \eta^{\mathrm{act}}, \tag{5.28}$$

where $E_i^{\mathrm{eq*}}$ is the apparent equilibrium potential, accounting for diffusion of Li^+ in the electrolyte and diffusion of $\mathrm{Li}i$ in the electrode. It is formulated according to Equation 6.1. For the detailed expansion see the Appendix.

$$
\begin{aligned}
E_i^{\mathrm{eq*}} &= E_{\mathrm{Li}i}^0 + \frac{\mathrm{R}T}{n\mathrm{F}}\left[\ln\left(\frac{a_i^{\mathrm{s}}}{a_{\mathrm{Li}i}^{\mathrm{s}}}\right) - U_i x_i + \zeta_i\right] \\
&\qquad\qquad\qquad\qquad + \frac{\mathrm{R}T}{n\mathrm{F}}\ln\left(\frac{a_{\mathrm{Li}^+}^{\mathrm{s}}}{a_{\mathrm{Li}^+}^{\mathrm{eq}}}\right) \\
&= E_i^{\mathrm{eq}} + \frac{\mathrm{R}T}{n\mathrm{F}}\ln\left(\frac{a_i^{\mathrm{s}}a_{\mathrm{Li}i}^{\mathrm{b}}}{a_{\mathrm{Li}i}^{\mathrm{s}}a_i^{\mathrm{b}}}\right) + \frac{\mathrm{R}T}{n\mathrm{F}}\ln\left(\frac{a_{\mathrm{Li}^+}^{\mathrm{s}}}{a_{\mathrm{Li}^+}^{\mathrm{eq}}}\right) \\
&= E_i^{\mathrm{eq}} + \eta_{\mathrm{Li}i}^{\mathrm{d}} + \frac{\mathrm{R}T}{n\mathrm{F}}\ln\left(\frac{a_{\mathrm{Li}^+}^{\mathrm{s}}}{a_{\mathrm{Li}^+}^{\mathrm{eq}}}\right) \\
&= E_i^{\mathrm{eq}} + \eta_{\mathrm{Li}i}^{\mathrm{d}} + \eta_{\mathrm{Li}^+}^{\mathrm{d}}
\end{aligned}
\tag{5.29}
$$

Together with overpotentials due to lithium diffusion in the electrode $\eta_{\mathrm{Li}i}^{\mathrm{d}}$ and in the the electrolyte $\eta_{\mathrm{Li}^+}^{\mathrm{d}}$, the apparent equilibrium potential $E_i^{\mathrm{eq*}}$ is a function of the equilibrium potential E_i^{eq}, which itself is a function of the standard redox potential E_i^0, the

stoichiometry-dependent attraction energy $\mathrm{R}TU_i x_i$ and the stoichiometry-independent attraction energy $\mathrm{R}T\zeta_i$. The individual terms of Equation 6.1 are summarised on the left hand side of Table 5.2 and are set opposite their chemical equivalents (using the $1/n\mathrm{F}$ conversion factor).

Substitution of Equation 5.28 into Equation 6.1 yields the electrode potential which establishes across the reaction site interface (i.e. $\phi^\mathrm{l} - \phi^\mathrm{s}$). This is visualised in Figure 5.6. It can be seen in the figure that the difference between real electrode potential $E_i^{\mathrm{eq}*}$ and the equilibrium electrode potential E_i^{eq} is the sum of all overpotentials $\eta_{\mathrm{Li}i}^\mathrm{d} + \eta_{\mathrm{Li}^+}^\mathrm{d} + \eta^\mathrm{act}$, in other words the ***charge-transfer overpotential*** η_i^ct of a species reaction.

> The useful potential to be obtained from each electrode (resulting in the overall useful potential between the cell tabs) is reduced by the charge transfer overpotential.
>
> $$\left(\phi^\mathrm{l} - \phi^\mathrm{s}\right)_i \;=\; E_i^{\mathrm{eq}} + \underbrace{\eta_{\mathrm{Li}i}^\mathrm{d} + \eta_{\mathrm{Li}^+}^\mathrm{d} + \eta^\mathrm{act}} \qquad (5.30)$$
>
> $$E_i^{\mathrm{eq}} + \qquad\qquad \eta_i^\mathrm{ct} \qquad\qquad\qquad (5.31)$$
>
> Together, the diffusion overpotential contributions of both species (Li^+ and $\mathrm{Li}i$) result in a potential drop in the process of extracting energy from the cell, whereby reducing the energy provided by the cell. Thus, correctly accounting for the potential drop is essential in a model used in dynamic applications (such as automotive). The model described in this section therefore evaluates change transfer overpotential as a sum of all its constituents.

The described overpotentials establish as soon as a current is allowed to flow between anode and cathode and electrochemical reactions occur. This net current I_bat between an electrode pair is composed of the cathodic current contribution from the reduction reaction i_Red and the anodic current contribution from the oxidation reaction i_Ox; both of which occur at their respective charge-transfer overpotentials [73].

$$I_\mathrm{bat} = (i_\mathrm{Red} - i_\mathrm{Ox})\, a_s = i^0 a_s \left[\left(\frac{a_\mathrm{Red}^\mathrm{s}}{a_\mathrm{Red}^\mathrm{b}}\right) \exp\left(\frac{\alpha^\mathrm{a}\mathrm{F}}{\mathrm{R}T}\eta^\mathrm{ct}\right) - \left(\frac{a_\mathrm{Ox}^\mathrm{s}}{a_\mathrm{Ox}^\mathrm{b}}\right) \exp\left(-\frac{\alpha^\mathrm{c}\mathrm{F}}{\mathrm{R}T}\eta^\mathrm{ct}\right) \right] \quad (5.32)$$

where i^0 is the exchange current density of a charge-transfer reaction in $[\mathrm{A\,m^{-2}}]$ and the ratios of surface and bulk quantities represent reduction and oxidation product diffusion in the electrodes.

The exchange current density term i^0, which denotes the reaction current flowing at zero overpotential, distinguishes in reduction (cathodic) and oxidation (anodic) current density (and therefore only dependent on bulk properties). It is a function of the electrode material and interface properties, the anodic k_a and the cathodic k_c charge transfer coefficients in $[\mathrm{m\,mol^{-0.5}\,s^{-1}}]$, the activity of the oxidised species a_Ox^b in the electrolyte and the activity of the reduced species in the electrode $a_\mathrm{Red}^\mathrm{b}$.

Description	Electrical domain [V]	Description	Chemical domain [J mol^{-1}]	Relation
Real equilibrium potential	$E_i^{\mathrm{eq}*}$	Real equilibrium energy	$\Delta G_{\mathrm{Lii}} + nF\eta_{\mathrm{Li}+}^{\mathrm{d}}$	$E_i^{\mathrm{eq}*} = \frac{\Delta G_{\mathrm{Lii}}}{nF} + \eta_{\mathrm{Li}+}^{\mathrm{d}}$
Equilibrium equilibrium potential	E_i^{eq}	Change in free energy	ΔG_{Lii}	$E_i^{\mathrm{eq}} = \frac{\Delta G_{\mathrm{Lii}}}{nF}$
Standard redox potential	E_i^0	Change in standard free energy	$\Delta G_{\mathrm{Lii}}^0$	$E_i^0 = \frac{\Delta G_{\mathrm{Lii}}^0}{nF}$
Electrical concentration potential	$\frac{RT}{nF}\ln\left(\frac{1-x_{\mathrm{Li}}^i}{x_{\mathrm{Li}}^i}\right)$	Electrochemical concentration energy	$RT\ln\left(\frac{1-x_{\mathrm{Li}}^i}{x_{\mathrm{Li}}^i}\right)$	$1/nF$
Stoichiometry-dependent interaction potential	$\frac{RT}{nF}U_i;x_{\mathrm{Li}}^i$	Stoichiometry-dependent interaction energy	$RT\,U_i;x_{\mathrm{Li}}^i$	$1/nF$
Stoichiometry-independent interaction potential	$\frac{RT}{nF}\zeta_i$	Stoichiometry-independent interaction energy	$RT\,\zeta_i$	$1/nF$
Diffusion overpotential in the electrode	$\eta_{\mathrm{Lii}}^{\mathrm{d}}$	Diffusion limitation energy in the electrode	$RT\ln\left(\frac{a_i^s a_{\mathrm{Lii}}^b}{a_{\mathrm{Lii}}^s a_i^b}\right)$	$\eta_{\mathrm{Lii}}^{\mathrm{d}} = \frac{RT}{nF}\ln\left(\frac{a_i^s a_{\mathrm{Lii}}^b}{a_{\mathrm{Lii}}^s a_i^b}\right)$
Diffusion overpotential in the electrolyte	$\eta_{\mathrm{Li}+}^{\mathrm{d}}$	Diffusion limitation energy in the electrolyte	$RT\ln\left(\frac{a_{\mathrm{Li}+}^s}{a_{\mathrm{Li}+}^{\mathrm{ref}}}\right)$	$\eta_{\mathrm{Li}+}^{\mathrm{d}} = \frac{RT}{nF}\ln\left(\frac{a_{\mathrm{Li}+}^s}{a_{\mathrm{Li}+}^{\mathrm{ref}}}\right)$
Activation overpotential due to the change in free electrochemical energy	η^{act}	Change in free electrochemical energy	$\Delta\bar{G}_{\mathrm{Lii}}$	$\eta^{\mathrm{act}} = \frac{\Delta\bar{G}_{\mathrm{Lii}}}{nF}$

Table 5.2: Detail overview over overpotential species contained in the real equilibrium Equation 5.28 at the example of an oxidation reaction at the potitive electrode during charge
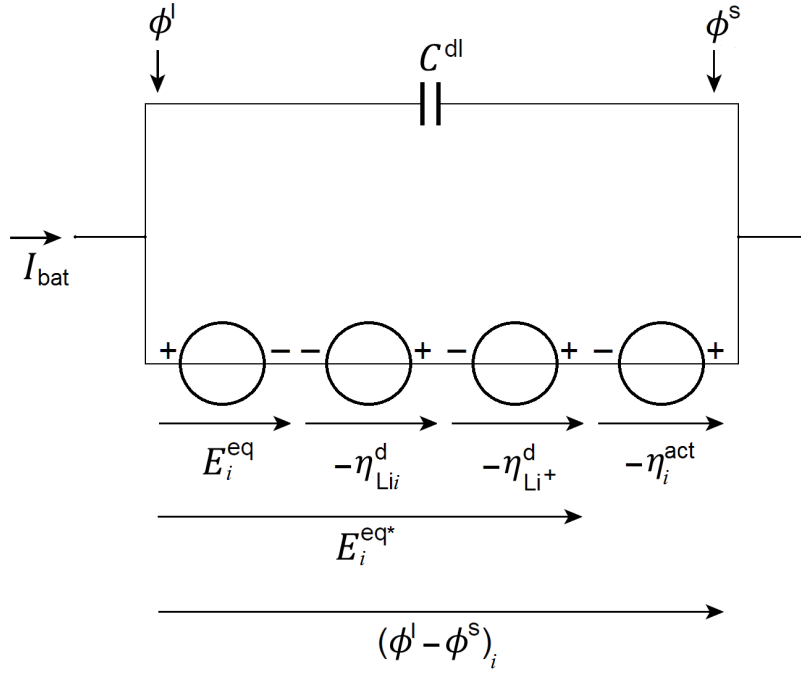
Figure 5.6: Visualisation of the complete real electrode potential equation in the electrical domain

For the charge transfer reaction at each electrode i surface, the exchange current density $i_{\text{Li}i}^0$ [168, 4] can be expressed as:

$$i_{\text{Li}i}^0 = n\text{F}a_{\text{Li}i}\left(k_\text{a}\right)^{\alpha^\text{a}}\left(k_\text{c}\right)^{\alpha^\text{c}}\left(a_i^\text{b}\right)^{\alpha^\text{c}}\left(a_{\text{Li}i}^\text{b}\right)^{\alpha^\text{a}} \tag{5.33}$$

I_bat (Equation 5.32) can be more conveniently expressed in terms of surface and bulk concentrations (instead of activities) by using the proportionality between activity and concentration given by Equation 5.2.

$$I_\text{bat} = \left(i_\text{Red} - i_\text{Ox}\right)a_\text{s} = i^0 a_\text{s}\left[\left(\frac{c_\text{Red}^\text{s}}{c_\text{Red}^\text{b}}\right)\exp\left(\frac{\alpha^\text{a}\text{F}}{\text{R}T}\eta^\text{ct}\right) - \left(\frac{c_\text{Ox}^\text{s}}{c_\text{Ox}^\text{b}}\right)\exp\left(-\frac{\alpha^\text{c}\text{F}}{\text{R}T}\eta^\text{ct}\right)\right] \tag{5.34}$$

The assumption that reduction/oxidation surface and bulk species concentrations are equal at any time $\left(c_\text{Red}^\text{s} = c_\text{Red}^\text{b} \text{ and } c_\text{Ox}^\text{s} = c_\text{Ox}^\text{b}\right)$ leads to a simplification of Equation 5.34, known as the Butler-Volmer equation (Equation 5.35). This simplification implies that there are no mass transport limitations between bulk and surface locations, and therefore no resulting diffusion overpotentials as part of the charge transfer overpotentials. The only remaining contribution to the charge transfer overpotential is therefore activation overpotential, leading to $\eta^\text{ct} = \eta^\text{act}$. Equation 5.34 simplifies accordingly to

$$I_\text{bat} = \left(i_\text{Red} - i_\text{Ox}\right)a_\text{s} = i^0 a_\text{s}\left[\exp\left(\frac{\alpha\text{F}}{\text{R}T}\eta^\text{act}\right) - \exp\left(-\frac{\alpha\text{F}}{\text{R}T}\eta^\text{act}\right)\right] \tag{5.35}$$
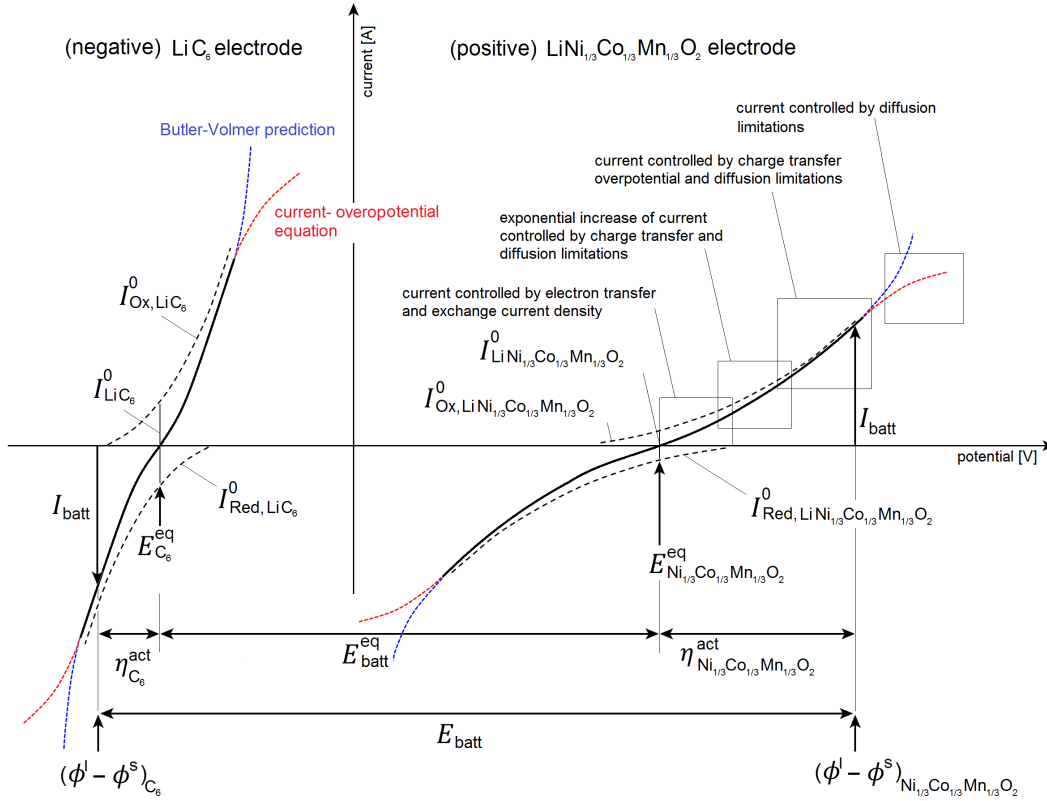
Figure 5.7: Current-overpotential characteristics of cathode and anode (red), compared to the Butler-Volmer prediction ($\eta_d = 0$) (blue)

Under the assumptions of the Butler-Volmer equation, the surface quantities in Equations 5.32 - 5.34 are defined as being equal to bulk concentrations. The difference in current-overpotential behaviour of the the surface-bulk distinction and the simplified Butler-Volmer assumption is shown in Figure 5.7. It can be seen that the assumption of no mass transport overpotential losses is only valid for relatively low currents. At high currents, the cell response to a load becomes dominated by diffusion limitations. This means models based on the Butler-Volmer equation alone are inadequate for predicting of cell behaviour under high C-rates and dynamic loads. Due to the importance of predicting cell behaviour under such conditions the full current-overpotential equation is implemented in this model (Equation 5.34) rather than the simplified Butler-Volmer equation (Equation 5.35). The regions beyond which the Butler-Volmer approximation ceases to be accurate as mass transport limitations become dominant are indicated in Figure 5.7.

5.4   The passivating layer

Upon first assembly of a cell with a carbon anode a passivating solid electrolyte interphase (SEI) layer forms at the electrode surface. This layer prevents the direct contact between electrode and electrolyte and the decomposition of the solid intercalation matrix. The first establishment of a homogeneous layer is therefore crucial for a long term performance of the battery and stable charge transfer reactions over the entire electrode surface. For this reason the first cycles of a cell's life are usually performed under tightly

controlled operating conditions as part of the manufacturing process before the cell is actually sold. Throughout operation, the passivating layer continues to grow slowly at the electrode/electrolyte interface due to the presence of continuous parasitic side-reactions. In order to account for its effects on battery performance, a layer of thickness δ_i^{pl} is considered to physically separate reactants and products, acting as a resistance against the charge transfer reactions. As a measure of cell degradation with cycling, the layer thickness and resistance are considered to increase at a rate depending on the exchange current and temperature. Also as a result of parasitic reactions, active lithium can be deposited at the layer irreversibly, such that it no longer participates in the reaction process, leading to capacity fade. The presence of a passivating layer also introduces an effective resistance R_i^{pl},contributing to an increase in cell internal impedance, and thus causing power fade. Prada et al.'s approach is adopted in describing the effects of this layer [141]. The passivating layer overpotential is the voltage drop over the layer:

$$\eta_{\mathrm{i}}^{\mathrm{pl}} \quad = \quad -\frac{i_{\mathrm{t}} R_i^{\mathrm{pl}}}{a_{\mathrm{s}}} \tag{5.36}$$

where

$$R_i^{\mathrm{pl}} = \frac{\delta^{\mathrm{pl}}}{\kappa^{\mathrm{pl}}} \tag{5.37}$$

The resistance posed by this layer increases at a rate depending on the exchange current and temperature. In doing so, cyclable lithium is bound to the layer and no longer participates in the redox shuttle; manifesting itself in capacity fade. The resistance increase also contributes to an increase in cell internal impedance, observable as power fade. Both of these concepts are included in this model and are discussed in detail in Section 5.9.

5.5 The triple species element

The electrical electrode/electrolyte interface potential accounts for overpotentials due to diffusion in the electrodes and the electrolyte, due to thermodynamic reaction activation and due to passivating layer losses (Equation 5.38).

A new circuit element termed the Triple Species Element encapsulates the following equation:

$$\left(\phi^{\mathrm{l}} - \phi^{\mathrm{s}}\right)_i \quad = \quad E_i^{\mathrm{eq}} + \eta_{\mathrm{Li}i}^{\mathrm{d}} + \eta_{\mathrm{Li}^{+}}^{\mathrm{d}} + \eta_i^{\mathrm{act}} + \eta_i^{\mathrm{pl}} \tag{5.38}$$

The **Triple Species Element (TSE)** encapsulates the process of the electrochemical reaction and, as such, serves as the link between the electrical and the chemical

> domains, connecting the three separate transport circuits of electrons, the reduced species (intercalated lithium) in the electrodes and the oxidized species (lithium-ions) in the electrolyte. It therefore represents the link between the electrochemical reaction in response to a load.

Equation 5.38 can be interpreted with the help of electric circuit elements. Figure 5.8a) shows the constituent electrode potential losses included in the proposed model as well as (b) the introduction of the TSE. The electrode equilibrium potential is reduced by all present overpotentials which act as losses. A capacitor is placed in parallel with the TSE to represent the double-layer capacitance at the reaction site and is discussed in Section 5.6.

5.6   The electrochemical double layer

The vicinity of the electrochemical charge-transfer process taking place is called the electrochemical double layer. The double layer forms at the interface of an electrical conductor and a ionically conducting electrolyte, in this case electrolyte, due to the local charge inhomogeneities, which occur as soon as a cell is first assembled and the components come into contact. It is a concept used to visualise the ionic environment in the vicinity of a charged electrode/electrolyte interface and may be more thought of as a region than a solid material layer.

The theory of a layer forming due to charged electrons immersed in electrolyte repelling co-ions of the charge while attracting counter-ions [169, 73] was presented by Hermann von Helmholtz in 1879. He derived that a layer of polarity of an atomic distance establishes at the interface of electrode and electrolyte [170].

He suggested that this ionic layer stores charge and that the local potential changes linearly from the electrode potential ϕ^s to the electrolyte potential ϕ^l over the Helmholtz distance δ_H, as shown in Figure 5.9a). In Helmholtz layer theory it is assumed that the capacitance of the dielectric ionic layer is constant, meaning it can simply be represented by a capacitor element, such that it behaves similarly to a dielectric capacitor.

In this simplified description of the double layer, the capacitance C_H is independent of the charge density and a function of the dielectric constant of the electrolyte as well as the double-layer (or in this case Helmholtz layer) thickness. The model simplifies many of the complex processes occurring in the vicinity of the electrode/electrolyte interface, such as adsorption onto the surface and interaction between solvent dipole moments and the electrode.

The Helmoltz layer theory was further modified by Gouy and Chapman [171, 172], by modelling anion and cation distribution in a non-linear way; They included a non-linear capacitance element C_{G-C}, as shown in Figure 5.9b) accounting for thermal motion of electrolyte anions and cations. The continuous distribution thereof in the electrolyte away from the electrode solid surface is called the diffuse layer. Their proposed exponential
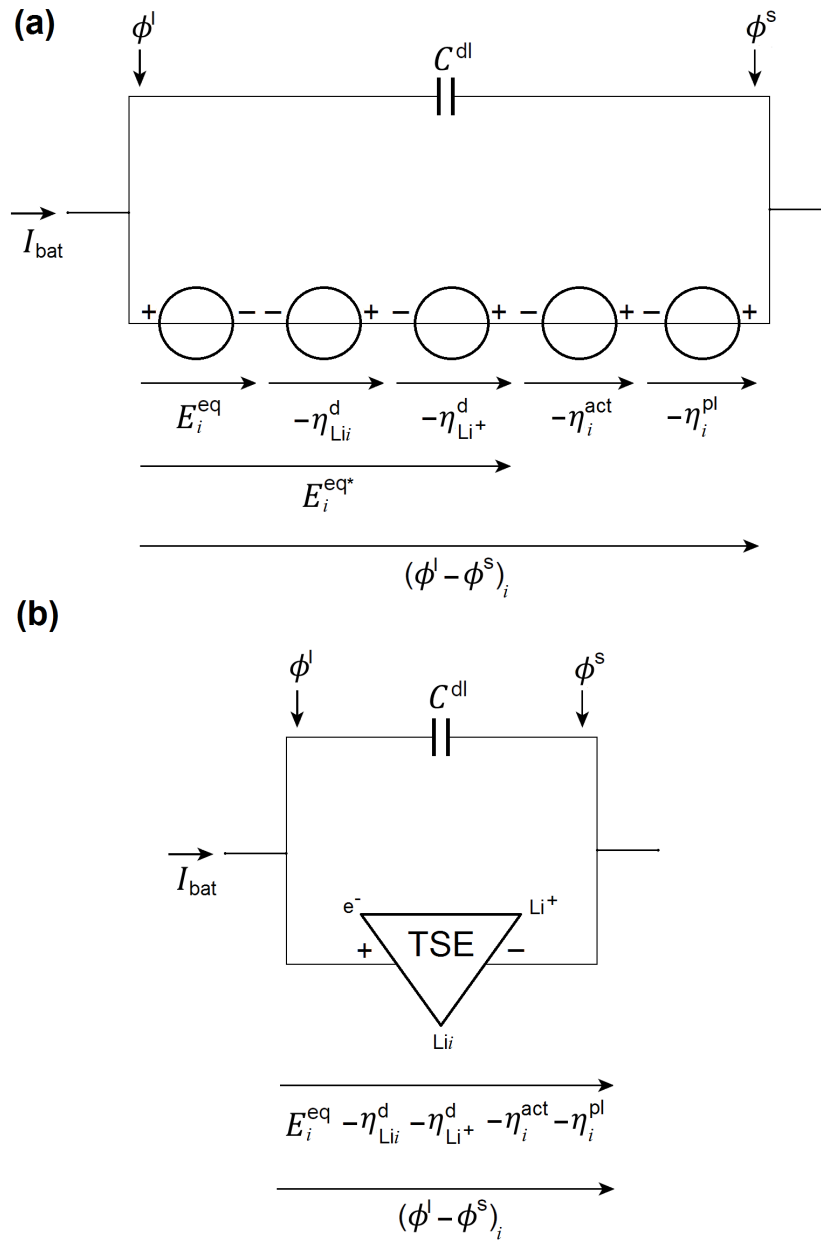
Figure 5.8: (a) Electrode/electrolyte interface potential including diffusion overpotentials, activation overpotential and passivating layer overpotential, and (b) Triple Species Element representation of Equation 5.38 representing the link between the electron, lithium-ion and intercalated lithium networks
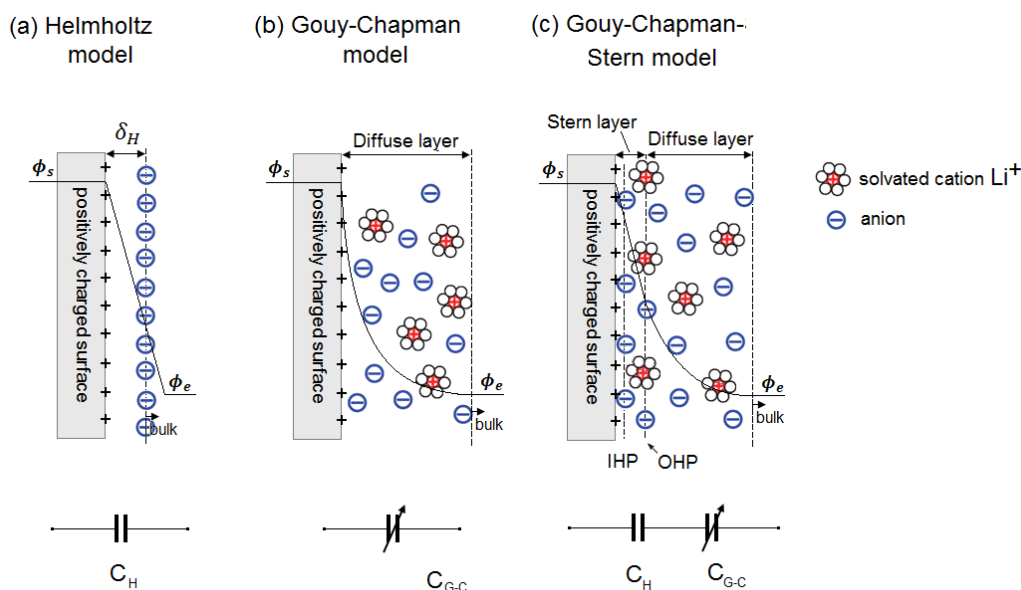
Figure 5.9: Schematic of double-layer models (a) the Helmholtz model, (b) the Gouy–Chapman model, and (c) the Stern model, showing the inner Helmholtz plane (IHP) and outer Helmholtz plane (OHP)

anion and cation distribution model resulted in an overestimation of capacitance in the location of a point charge at the electrode surface.

Aiming to overcome the problem of exponential capacitance at the electrode surface, Stern [173] integrated the two previous modelling approaches, proposing that the double layer is formed by a Helmholtz layer in series with a Gouy-Chapman layer, as shown in Figure 5.9c). The former, called a compact or Stern layer, contains adsorbed ions. He defined the regions occupied by the two types of adsorbed ions by further distinguishing the inner Helmholtz plane and the outer Helmholtz plane.

This field of research has been very active in the past and many more theories have been offered, although disagreement remains as to what the double layer actually is, where it is and what it depends on [73, 164, 174]. A challenging aspect in modelling the region at the interface of the electrode and the electrolyte is that the physical phenomena are near-impossible to experimentally verify. As soon as a reference electrode is inserted to investigate local properties, it itself has an effect on the electrochemical processes taking place. Furthermore, the definition of the location of 'bulk' electrolyte poses challenges in the analysis in that there is disagreement where the screening length ends in the region of the reaction site. Although the effect of polarity in the vicinity of the interface ceases to affect the ionic movement further away from the surface it is difficult to define where this non-linearly decreasing potential region ends.

The vicinity of the double-layer at the electrode-electrolyte interface is where the electrochemical charge-transport process takes place. The high ionic concentrations that are inherent to the double layer are expected to affect ionic transport to and from the interface.

The following represents the simplest version of the Gouy-Chapman model. Only univalent ions are considered and the electrolyte assumed to be charge neutral, such that

there is an equal number of positive and negative ions.

The distance over which the potential drop η_i^{dl} due to the presence of the double layer occurs, is characterised by the Debye length λ [175, 176]. The Debye length in turn is a function of electrolyte lithium-ion concentration c_{Li^+}, the applied current, and the ionic conductivity of the double layer film κ^{dl} in $[\mathrm{S\,m^{-1}}]$. This means that, the more concentrated the bulk electrolyte, the smaller the Debye length, meaning the screening is more effective.

The double-layer overpotential is therefore a function of only the electrolyte properties and is independent of electrical potential of the electrode.

$$\eta_i^{\mathrm{dl}} = \frac{\lambda_i}{\kappa_i^{\mathrm{dl}}}, \tag{5.39}$$

where

$$\lambda = \sqrt{\frac{\mathrm{R}T\varepsilon_0\varepsilon_{\mathrm{r}}}{2(n\mathrm{F})^2 c_{\mathrm{Li}^+}}}, \tag{5.40}$$

where ε_0 is the the permittivity of free space and ε_{r} is the dielectric constant in $[\mathrm{F\,m^{-1}}]$.

Oldham *et al.* [172] refined the expressions first proposed by Kornyshev [177] for electrode/electrolyte interfaces, by relating the electrical potential difference between the electrode/electrolyte interface $\phi^{\mathrm{l}}(0)$ and the bulk electrolyte $\phi^{\mathrm{l}}(\infty)$ to the charge density q on the interface as a sum of an inner layer potential drop (first term of Equation 5.41), depending on particle size of a lithium-ion r_{Li^+} and an outer layer potential drop (second term of Equation 5.41).

$$\frac{\phi^{\mathrm{l}}(0) - \phi^{\mathrm{l}}(\infty)}{q} = \frac{r_{\mathrm{Li}^+}}{\varepsilon_0\varepsilon_{\mathrm{r}}} + \frac{2\mathrm{R}T}{n\mathrm{F}q} \arcsin\left\{ \frac{q}{\sqrt{8\mathrm{R}T\varepsilon_0\varepsilon_{\mathrm{r}}c_{\mathrm{Li}^+}(x)}} \right\} \tag{5.41}$$

This equation can be expressed as two capacitors in series, thus the overall capacitance of the double layer being the inverse of the sum of the reciprocals of the two constituting layers; the inner and the outer.

$$
\begin{aligned}
\frac{1}{C_{\mathrm{dl}}} &= \frac{\phi^{\mathrm{l}}(0) - \phi^{\mathrm{l}}(\infty)}{q} \\
&= \frac{\phi^{\mathrm{l}}(0) - \phi^{\mathrm{l}}(\lambda)}{q} + \frac{\phi^{\mathrm{l}}(\lambda) - \phi^{\mathrm{l}}(\infty)}{q} \\
&= \frac{1}{C_{\mathrm{inner}}} + \frac{1}{C_{\mathrm{outer}}},
\end{aligned}
\tag{5.42}
$$

where the capacitances of the inner layer capacitance can be formulated as

$$C_{\text{inner}} = \frac{\varepsilon_0 \varepsilon_{\text{r}}}{r_{\text{Li+}}} \tag{5.43}$$

and the outer layers can be obtained by factoring Equation 5.40 out of Equation 5.41 as

$$C_{\text{outer}} = \frac{\sqrt{\varepsilon_0 \varepsilon_{\text{r}}}}{\lambda} \frac{q}{\sqrt{8\text{R}Tc_{\text{Li+}}(x)} \arcsin\left\{\frac{q}{\sqrt{8\text{R}T\varepsilon_0\varepsilon_{\text{r}}c_{\text{Li+}}(x)}}\right\}}. \tag{5.44}$$

It can be seen that only the outer layer capacitance varies as a function of lithium-ion concentration away from the reaction site, while the inner layer is described by a linear relationship between distance and capacitance. Equation 5.42 of this Gouy-Chapman modification proposed by Oldham *et al.* is plotted in Figure 5.10 for the Kokam 5 Ah cell (Parameters: $\varepsilon_{\text{r}} = 0.177\,\text{nF}\,\text{m}^{-1}$, $r_{\text{Li+}} = 1.00\,\text{nm}$, $c_{\text{Li}i}(\infty) = 1200\,\text{mol}\,\text{m}^{-1}$ and $T = 298\,\text{K}$).
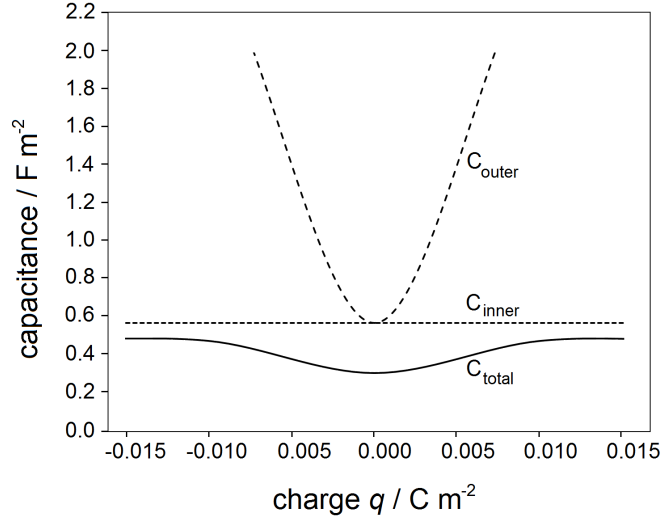
Figure 5.10: Inner and outer double layer capacitance contribution as a function of stored charge at the solid-electrode interface under the assumption of constant electrolyte density for a Kokam 5 Ah cell

In Figure 5.10, the capacitance contributions from the inner and the outer layer are distinguished. For the case of an un-polarised double-layer (the point of zero charge) the capacitance of the layer minimises, as can be seen by the vertical axis intersection in Figure 5.10. Under this condition, the Equation 5.41 for the overall layer capacitance at each electrode/electrolyte interface simplifies to

$$C_i^{\text{dl}} = \frac{\varepsilon_0 \varepsilon_{\text{r}}}{r_{\text{Li+}} + \lambda_i}. \tag{5.45}$$

As has been shown previously in Figures 5.4 - 5.6, the double-layer capacitance is arranged in parallel with with the apparent electrode potential in the circuit arrangement.

5.7   Species transport in the electrode and electrolyte

Up to this point only the electrochemical phenomena at the reaction site have been discussed. In the following, the physical processes associated with mass transport between bulk and interface locations will be discussed. This allows the derivation of electrical circuit equivalents which encapsulate the capacitative and resistive nature of electrochemical species transport in electrodes and electrolyte. Expressions reflecting the physical phenomena will be derived allowing the representation of the system in an equivalent circuit while retaining a logical phenomenological correspondence to the physical phenomena.

5.7.1   Species transport in the electrolyte

As a current is applied, a concentration gradient of lithium-ion in the electrolyte phase establishes, resulting in relative ionic motion from high to low concentration regions, encapsulated by a separate sub-circuit representing diffusion in the electrolyte. The flux of a species as a result of such concentration gradients can be described by Fick's first law,

$$J_i(x,t) = -D_i \frac{\delta c_i(x,t)}{\delta x} \tag{5.46}$$

such that particles diffuse away from regions of high concentration to regions of low concentration. In general, a space-varying flux leads to a change in local concentration with time, as given by Fick's second law:

$$\frac{\delta c_i(x,t)}{\delta t} = D_i \frac{\delta^2 c_i(x,t)}{\delta x^2} \tag{5.47}$$

When modelling species transport to or away from intercalation or de-intercalation sites, a source/sink term j_{Li} in $[\text{A m}^{-3}]$, denoting the consumption/production of species at the electrode/electrolyte interface has to be included in Equation 5.47; This term represents additional mass entering or leaving the respective species circuit and applies at each electrode/electrolyte interface.

For example, as a charge is applied, the negative species flux due to a positive concentration gradient of the to-be-reduced (intercalated lithium) species in the cathode leads to a positive concentration gradient in the electrolyte next to it of the already oxidised species (lithium-ions), in turn leading to a species flux there. Diffusion of lithium-ion in the electrolyte can be formulated as

$$\frac{\partial \left(\varepsilon^{\text{l}} c_{\text{Li}^+}\right)}{\partial t} = \frac{\partial}{\partial x}\left(D_{\text{Li}^+}^{\text{eff}} \frac{\partial}{\partial x} c_{\text{Li}^+}\right) + \frac{1 - t_+^0}{\text{F}} j_{\text{Li}}, \tag{5.48}$$

where ε is the electrolyte volume fraction and t_+^0 is the ion transport number [73]. The ion transport number, also called the transference number, is the fraction of total current

carried in an electrolyte by a given ion. Typically, salts in aqueous solution have transference numbers near 0.5, meaning each species (ions and cations) carries roughly half of the current [73].

The boundary conditions in the electrical domain reflect the fact that Li^+ is contained in the electrolyte only.

$$\left. \frac{\partial c_{Li^+}}{\partial x} \right|_{x=0} = \left. \frac{\partial c_{Li^+}}{\partial x} \right|_{x=L} = 0. \tag{5.49}$$

The effective electrolyte diffusion coefficient of lithium-ions $D_{Li^+}^{eff}$ in $[m^2\,s^{-1}]$ is a function of the weighted average of the diffusion coefficient D_{Li^+} of the anions and the cations in either the separator or the electrodes and ε^l is the volume fraction of the electrolyte phase.

$$D_{Li^+}^{eff} = D_{Li^+} \varepsilon^l \tag{5.50}$$

5.7.2 Species transport in the electrodes

This methodology can be applied for diffusion in the radial direction for the purpose of species transport modelling in the spherical electrode particles. The species transported in the sub-circuit describing the electrodes is uncharged intercalated lithium Lii.

$$\frac{\partial c_{Lii}}{\partial t} = \frac{D_{Lii}}{r^2} \frac{\partial}{\partial r} \left(r^2 \frac{\partial c_{Lii}}{\partial r} \right), \tag{5.51}$$

where i denotes the respective electrode domain and D_{Lii} is the respective electrode diffusion coefficient in $[m^2\,s^{-1}]$.

The boundary condition in this case reflects the fact that the intercalated lithium can only be produced/consumed by reactions at the electrode/electrolyte interface of area a_s. They are converted from/into Li^+, as specified by Equation 5.48 and appear in the source/-sink term j_{Li} at the electrode/electrolyte interface. The boundary conditions reflect the symmetry of geometry chosen for spherical particles in Equation 5.51.

$$\left. \frac{\partial c_{Lii}}{\partial r} \right|_{r=0} = 0, \, -D_{Lii} \left. \frac{\partial c_{Lii}}{\partial r} \right|_{r=r_S} = \frac{j_{Li}}{a_s F} \tag{5.52}$$

5.7.3 Phenomenological electric circuit elements derivation

The transport phenomena of lithium-ions in electrolyte and intercalated lithium in electrodes are translated into phenomenological electric circuit elements in the following. These form the building blocks of the sub-circuits governing the transport of the individual species, which will finally be assembled into a complete circuit network governing the electrochemical reactions between them.

> As lithium-ions are positively and electrons are negatively charged species, the circuit element governing their transport are formulated to reflect electrical quantities in $[V]$, $[A]$, $[\Omega]$ and $[F]$. Intercalated lithium represents an uncharged chemical species, hence the formulation of the circuit governing its transport to reflect electrochemical/chemical quantities in $[J \, mol^{-1}]$, $[mol \, s^{-1}]$, $[J \, s \, mol^{-2}]$ and $[mol^2 \, J^{-1}]$. The TSE represents the translation node where chemical quantities are linked to electrical quantities by a conversion factor of $1/nF$.

The low-frequency phenomenon of mass transport by diffusion is commonly modelled in equivalent circuit models by RC pair arrangements. Such fitted resistor-capacitor networks are, however, not derived from the physical phenomena in a cell. Not only this, it also makes those models less flexible outside their parametrisation regime, which makes this approach unsuitable for the purpose of this thesis. Here, each electrical analogy is to retain its physical meaning, hence the values of all resistors and capacitors are to be functions of fundamental electrochemical parameters unlike in previous ECN models.

The RC pair arrangement implemented for mass transport in the chemical and electrical domains is shown in the electrode (in spherical coordinates) and in the electrolyte (in Cartesian coordinates) in Figure 5.11. The values of the resistors and capacitors in each domain are derived in the following.

In the chemical domain, the charge on the capacitor corresponds to the molar amount m_i of the species present within a shell volume and the potential drop across the capacitor corresponds to the specie's electrochemical potential $\bar{\mu}_i$. In the case of an electrical field being present the additional potential of the capacitor is equal to the electrostatic potential. The resulting potential across the entire element then amounts to the electrochemical potential as the sum of chemical potential and electrostatic potential, as shown in Figure 5.12.

The definition of capacitance of a species is derived in the following in the chemical domain in $[mol^2 \, J^{-1}]$ following an analogy to a dielectric capacitor. As stated previously, activity a_i tends to be proportional to molar content m_i by $a_i(x) = \gamma m_i(x)/m_{\text{ref}}(x)$. This allows the substitution of molar amount m_i, using the fact that concentration is equal to $m_i(x)/(\Delta x)^3$ to obtain the chemical (superscript = 'ch') capacitance $C^{\text{ch}}(x, t)$ as a function of concentration in a control volume.

The chemical capacitance as a result of local species particle concentration is therefore

$$\frac{1}{C^{\text{ch}}(m_i)} = \frac{\partial \bar{\mu}_i}{\partial m_i} = \frac{\partial}{\partial m_i} \left(\mu_i^0 + RT \ln \left(\frac{m_i}{m_i^{\text{ref}}} \right) \right) = \frac{RT}{m_i} \tag{5.53}$$

This methodology is applied to the chemical capacitance in $[mol^2 \, J^{-1}]$ in the intercalated lithium transport network inside the electrodes, which is in this case in polar coordinates; resulting in the chemical capacitance of a shell-shaped volume at distance r_j from the particle centre.
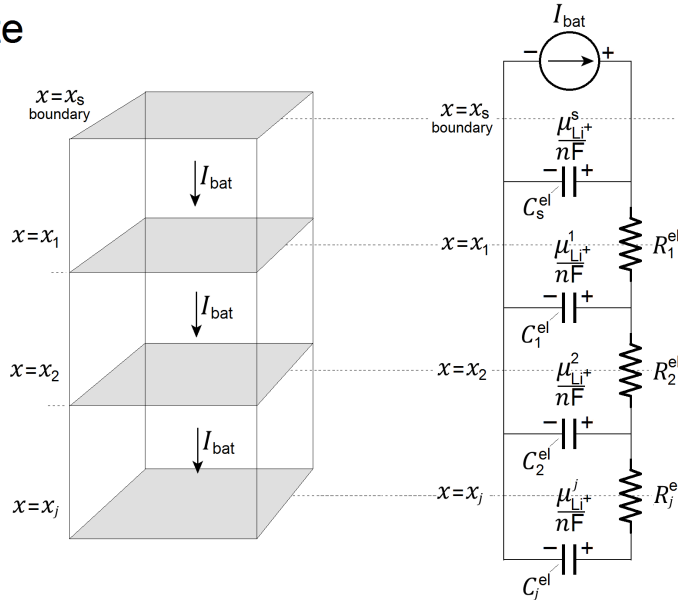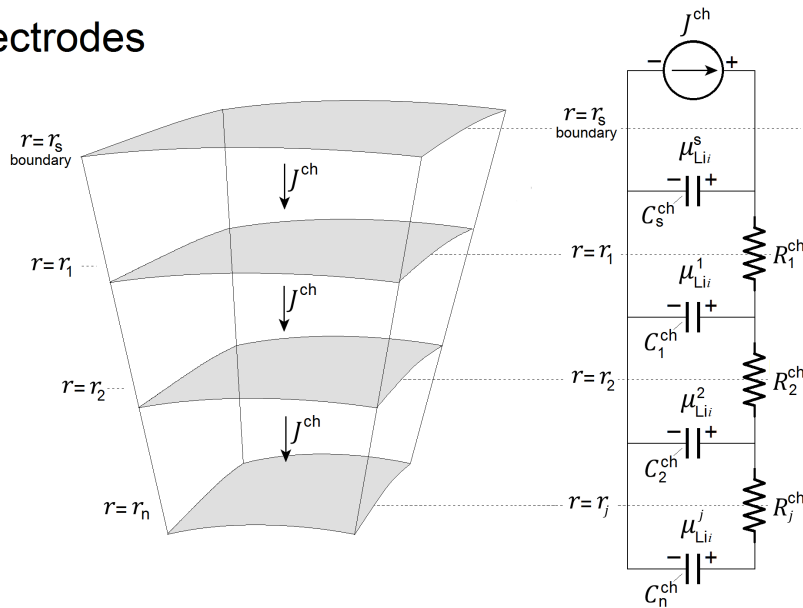
Figure 5.11: Resistor and capacitor (RC) elements integration for (top) lithium-ion transport in the electrolyte in Cartesian coordinates in the electrical domain, and (bottom) intercalated lithium transport inside the electrodes in the chemical domain in spherical coordinates
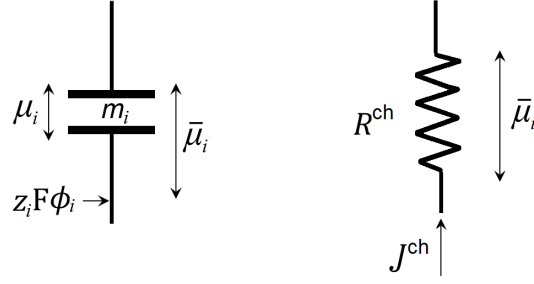
Figure 5.12: Capacitor electrical equivalent of the electrochemical potential $\bar{\mu}_i$ of species i consisting of the chemical potential μ_i in its' uncharged state and the additional electrostatic potential $z_i\mathrm{F}\phi_i$ due to a charge being applied to the species

$$C_{\mathrm{Li}i}^{\mathrm{ch}}(r_j) \;=\; \frac{c_{\mathrm{Li}i}(r_j)}{\mathrm{R}T(x_j)} \cdot \frac{4}{3}\pi (r_j - r_{j-1})^3 \tag{5.54}$$

where j is a counter through the spatial discretisation points. This equation is valid for transport through both electrodes i. The temperature inside the particle is considered homogeneous and taken to be equal to the surface temperature $T(x_j)$ of each particle. A detailed discussion of the thermal model is provided in Section 5.10.

Using Equations 5.15 - 5.16, the expression for the electrical capacitance of discretised electrolyte volumes with lithium-ions can be derived in Cartesian coordinates in [F] in the electrical domain by applying the $1/n\mathrm{F}$ conversion factor. Although the assumption is made in this model that the amount of species particles participating in each reaction is equal $(n_{\mathrm{Li}^+} = n_{\mathrm{Li}i} = n)$ these n-terms are included in the following derivations to allow future adaptation to species reactions obeying different reaction ratios.

$$C_{\mathrm{Li}^+}^{\mathrm{el}}(x_j) = \frac{c_{\mathrm{Li}^+}(x_j)}{\mathrm{R}T(x_j)(n\mathrm{F})^2} \cdot (x_j - x_{j-1}) A_{\mathrm{s}} \tag{5.55}$$

The local species concentration variations in the electrodes lead to species fluxes to and away from the interface. Transport from a region with high electrochemical potential to a region with low electrochemical potential can be expressed as [178]:

$$J_i^{\mathrm{ch}}(r_j) = -\frac{Dc_i(r_j)}{\mathrm{R}T(x_j)}\frac{\partial \bar{\mu}_i}{\partial r} \cdot (r_j - r_{j-1}) \tag{5.56}$$

The chemical flux can be considered as the result of an electrochemical potential gradient across a chemical resistance such that

$$J_i^{\mathrm{ch}}(r_j) = -\frac{1}{R_i^{\mathrm{ch}}(r_j)} \cdot \frac{\partial \bar{\mu}_i}{\partial r}. \tag{5.57}$$

Equating Equations 5.56 and 5.57 allows the derivation of an expression of $R_{\mathrm{Li}i}^{\mathrm{ch}}(r_j)$ as a resistance in $[\mathrm{J\,s\,mol}^{-2}]$ to an intercalated lithium flux inside the electrodes.

$$R_{\text{Li}i}^{\text{ch}}\left(r_j\right) = \frac{\text{R}T\left(r_j\right)}{c_{\text{Li}i}\left(r_j\right)D_{\text{Li}i}} \cdot \left(r_j - r_{j-1}\right)^{-1} \tag{5.58}$$

Analogous to the methodology applied for deriving chemical capacitances, Equation 5.15 is used to obtain the expression for resistance in $[\Omega]$ to a flux of lithium-ions though electrolyte in the electrical domain and in Cartesian coordinates:

$$R_{\text{Li}^+}^{\text{el}}\left(x_j\right) = \frac{\text{R}T\left(x_j\right)\cdot\left(n\text{F}\right)^2}{c_{\text{Li}^+}\left(x_j\right)D_{\text{Li}^+}} \cdot \left(x_j - x_{j-1}\right)^{-1}. \tag{5.59}$$

The expressions for R^{el} and C^{el} allow the calculation of an RC time as $\triangle x^2/D$ which is in accordance with derivations by Horno *et al.* [179].

Derivative quantities of energy and power can be derived easily using these fundamental electrical and chemical expressions and are summarised in Table 5.3.

Electrical domain			Chemical domain		
Quantity	*Symbol*	*Unit*	*Quantity*	*Symbol*	*Unit*
Electrical **potential**	V	V	Electrochemical **potential**	$\bar{\mu}$	J mol^{-1}
Electron **flux** (current)	I	A	Chemical **flux**	J^{ch}	mol s^{-1}
Electrical **power**	$P^{\text{el}} = VI$	W	Chemical **power**	$P^{\text{ch}} = \bar{\mu}J^{\text{ch}}$	W
Charge **amount**	$Q = It$	C	Molar **amount**	$m = J^{ch}t$	mol
Electrical **energy**	$E^{\text{el}} = P^{\text{el}}t$	J	Chemical **energy**	$E^{\text{ch}} = P^{\text{ch}}t$	J
Electrical **capacitance**	$C^{\text{el}} = QV^{-1}$	F	Chemical **capacitance**	$C^{\text{ch}} = m\,\bar{\mu}^{-1}$	$\text{mol}^2\,\text{J}^{-1}$
Electrical **resistance**	$R^{\text{el}} = VI^{-1}$	Ω	Chemical **resistance**	$R^{\text{ch}} = \bar{\mu}\left(J^{\text{ch}}\right)^{-1}$	Js mol^{-2}

Table 5.3: Analogy between the electrical and chemical domains

5.8 Charge conservation

Charge has to be conserved in the electrolyte as part of the chemically balanced reaction at the anode and the cathode. Equation 5.60 is therefore adopted

$$\frac{\partial}{\partial x}\left(\kappa^{\text{eff}}\frac{\partial}{\partial x}\phi^{\text{l}}\right) + \frac{\partial}{\partial x}\left(\kappa_{\text{D}}^{\text{eff}}\frac{\partial}{\partial x}c_{\text{Li}^+}\right) + j_{\text{Li}} = 0, \tag{5.60}$$

where κ^{eff} is the electrolyte effective ionic conductivity in $[\text{S m}^{-1}]$ and $\kappa_{\text{D}}^{\text{eff}}$ is the electrolyte ionic conductivity in $[\text{A m}^{-1}]$. As previously, j_{Li} represents the source/sink term due to the conversion of chemical species which enter/leave the electrolyte.

Furthermore, it is assumed that there is no flux of the species out of the control volume, meaning the domain potential gradient at the boundary $[x = 0, L]$ must be zero.

$$\left.\frac{\partial\phi^{\text{l}}}{\partial x}\right|_{x=0} = \left.\frac{\partial\phi^{\text{l}}}{\partial x}\right|_{x=\text{L}} = 0 \tag{5.61}$$

The electrolyte ionic conductivity $\kappa_{\mathrm{D}}^{\mathrm{eff}}$ is in itself a function of the concentration of the species in the electrolyte.

$$\kappa_{\mathrm{D}}^{\mathrm{eff}} = \frac{2\mathrm{R}T\kappa^{\mathrm{eff}}}{\mathrm{F}} \left(t_{+}^{0} - 1\right) \left(1 + \frac{d\ln f_{\pm}}{d\ln c_i}\right) \tag{5.62}$$

and,

$$\kappa^{\mathrm{eff}} = \kappa\varepsilon_{\mathrm{Li+}}^{\mathrm{p}}, \tag{5.63}$$

where the electrolyte ionic conductivity in the bulk electrolyte κ was obtained experimentally by Smith & Wang *et al.* [142].

$$\kappa = 15.8c_{\mathrm{Li+}}\exp\left(-13472\cdot c_{\mathrm{Li+}}^{1.4}\right) \tag{5.64}$$

Charge also has to be conserved inside the electrodes. The source/sink term links the electrode and electrolyte domains (Equations 5.60-5.65). This expression applies to both electrodes

$$\frac{\partial}{\partial x}\left(\sigma_{\mathrm{Li}i}^{\mathrm{eff}}\frac{\partial}{\partial x}\phi_{\mathrm{Li}i}^{\mathrm{s}}\right) = j_{\mathrm{Li}} \tag{5.65}$$

Note that a fixed sign j_{Li} acts as a source in one domain and as a sink in the other. At the electrode/current collector interfaces there is a charge flux which is a function of the drawn current (Equation 5.66). At the separator the boundary conditions for the conservation of charge in the electrodes (Equation 5.67) can be deduced as

$$-\sigma_{\mathrm{a}}^{\mathrm{eff}}\frac{\partial\phi_{\mathrm{a}}^{\mathrm{s}}}{\partial x}\bigg|_{x=0} = \sigma_{\mathrm{c}}^{\mathrm{eff}} + \frac{\partial\phi_{\mathrm{c}}^{\mathrm{s}}}{\partial x}\bigg|_{x=\mathrm{L}} = \frac{I}{A_{\mathrm{s}}} \tag{5.66}$$

$$\frac{\partial\phi_{\mathrm{a}}^{\mathrm{s}}}{\partial x}\bigg|_{x=\mathrm{L}_{-}} = \frac{\partial\phi_{\mathrm{c}}^{\mathrm{s}}}{\partial x}\bigg|_{x=\mathrm{L}-\mathrm{L}_{+}} = 0 \tag{5.67}$$

where the effective electronic conductivities $\sigma_{\mathrm{Li}i}^{\mathrm{eff}}$ in $[\mathrm{S\,m^{-1}}]$ for each electrode are defined as

$$\sigma_{\mathrm{Li}i}^{\mathrm{eff}} = \sigma_{\mathrm{Li}i}\varepsilon_{\mathrm{Li}i} \tag{5.68}$$

The equivalent circuits for the sub-systems (intercalated lithium, lithium-ions and electrons) are combined, as shown in Figure 5.13. As can be seen the TSE links the e^{-} circuit containing an electron transport resistance $R_{\mathrm{el}}^{\mathrm{e}^{-}}$, the intercalated lithium circuits in the electrodes and the lithium-ion circuit in the electrolyte.
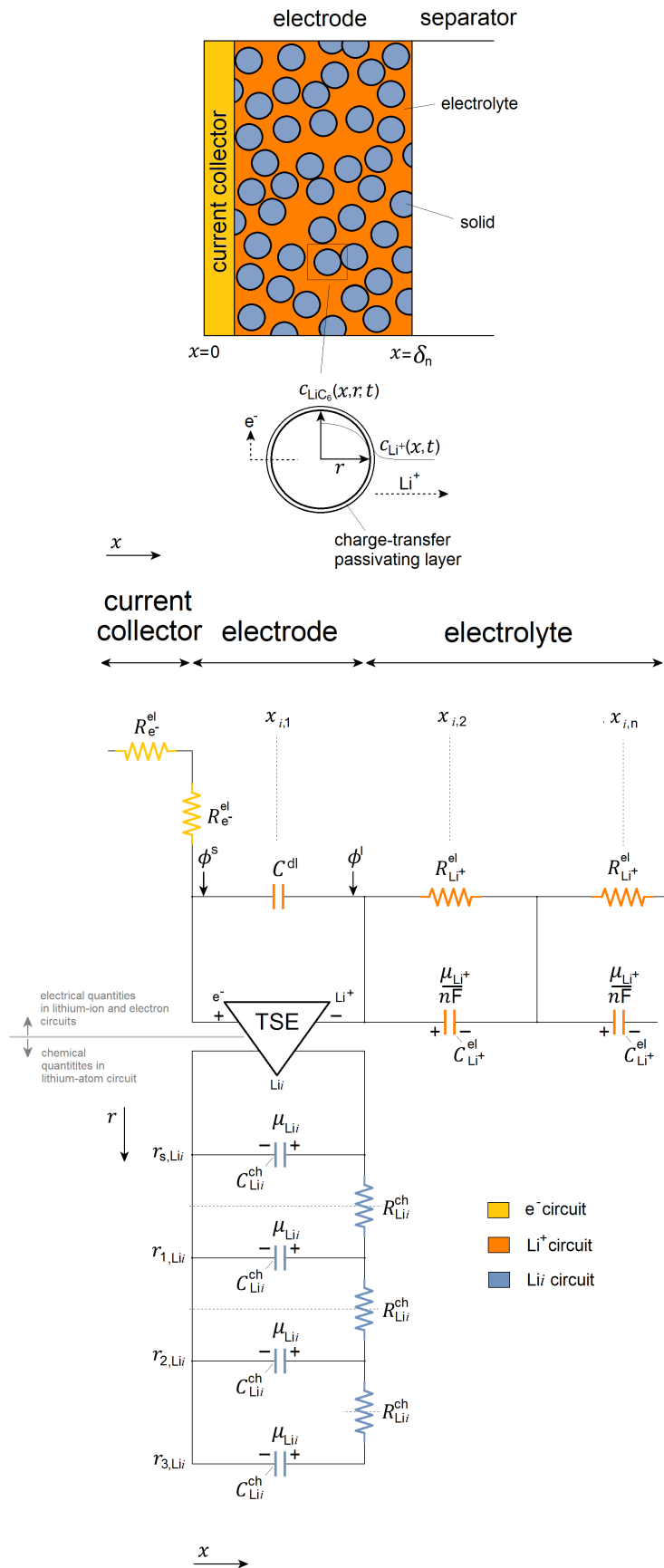
Figure 5.13: Triple Species Element (TSE) implementation with sample sub-circuits for electron, intercalated lithium and lithium-ion transport

5.9 Degradation through passivating layer growth

As discussed previously, one of the main reasons for cell degradation is through passivating layer growth due to side-reactions, leading to an increase in internal impedance and a loss in cyclable lithium. These unwanted side-reactions are observable as a passivating layer exchange current density i^{pl}. The total exchange current density i_{t} in $[\mathrm{A\,m^{-2}}]$ therefore has to be differentiated in exchange current density from useful electrochemical reaction i_{int} and from the parasitic side-reaction i^{pl} leading to the growth of the passivating layer.

$$i_{\mathrm{t},i} = i_{\mathrm{int},i} + i_i^{\mathrm{pl}} \tag{5.69}$$

The assumption is made that the process of passivating layer growth is irreversible, as it has been shown that the reverse reaction contributes less than 1% of exchange current density [175].

Under this assumption the current-overpotential equation for the side-reaction exchange current density i_i^{pl} for the passivating layers on each electrode simplifies according to the Tafel equation [73]:

$$i_i^{\mathrm{pl}} \;=\; -i_i^0 a_{\mathrm{s},i} \exp\left(\frac{\mathrm{F}}{2\mathrm{R}T}\eta_i^{\mathrm{pl}}\right). \tag{5.70}$$

It is often assumed in the literature that the passivating layer growth at the cathode is negligible [180]. For generality and versatility of the model, however, both anode and cathode layer growths are included although their rate of growths are likely to differ greatly.

The side-reaction exchange current density through the passivating layer leads to a potential drop η_i^{pl} and therefore a reduction of useful potential. As could be seen previously from its definition in Equation 5.36, η_i^{pl} is a function of reaction interface area a_{s}, passivating layer resistance R^{pl} in $[\Omega]$ and the total exchange current density. The total current effectively causes passivating layer growth and yields the side-reaction exchange current, while a fraction (determined by the value of a_{s}) of the total current is lost in the side-reaction. The rate of passivating layer growth can be expressed according to [141]:

$$\frac{d}{dt}R_i^{\mathrm{pl}} \;=\; \frac{1}{\kappa_i^{\mathrm{pl}} S_i}\frac{d}{dt}\delta_i^{\mathrm{pl}}, \tag{5.71}$$

where

$$S_i = 3\varepsilon_{\mathrm{s},i}\delta_i^{\mathrm{pl}}\frac{a_{\mathrm{s},i}}{r_{\mathrm{s},i}} \tag{5.72}$$

The rate of growth of the passivating layer thickness is related to the magnitude of the side-reaction current density, the layer's density ρ_i^{pl} in $[\mathrm{kg\,m^{-3}}]$ and the molar weight of the new precipitate M_i^{pl} in $[\mathrm{kg\,mol^{-1}}]$.

$$\frac{d}{dt}\delta_i^{\mathrm{pl}} = -\frac{i_i^{\mathrm{pl}}}{2\mathrm{F}}\frac{M_i^{\mathrm{pl}}}{\rho_i^{\mathrm{pl}}} \tag{5.73}$$

This integral of passivating layer side-reaction current density represents the amount of cumulative capacity lost due to electroactive material being tied up in the interface region. It no longer participates in the electrochemical shuttle between anode and cathode and presents a quantifiable capacity loss to the system.

$$Q_i^{\mathrm{pl}} = -\int\limits_0^t \int\limits_0^{\mathrm{L}} i_i^{\mathrm{pl}} dx\, dt \tag{5.74}$$

5.10   Heat generation

The electrochemical processes inside the cell cause various types of heat generation and absorption leading to a local temperature change, which in turn affects material properties. The temperature dependence of reaction rates is commonly formulated with an Arrhenius law:

$$\Psi = \Psi_{\mathrm{ref}}\exp\left[\frac{E_{\mathrm{act}}^{\Psi}}{\mathrm{R}}\left(\frac{1}{T_{\mathrm{ref}}}-\frac{1}{T}\right)\right] \tag{5.75}$$

Each property Ψ at temperature T is a function of its reference value Ψ_{ref} at its reference temperature T_{ref} in $[\mathrm{K}]$, while activation energy E_{act}^{Ψ} in $[\mathrm{J\,mol^{-1}}]$ represents the temperature sensitivity of the property.

Heat generation and absorption in a cell during operation is due to a combination of reaction heat (q_{r}), ohmic heat from ionic transport though the electrode and electrolyte phase (q_{j}), ohmic heat due to the contact resistance between the electrodes and the respective current collectors (q_{c}) and entropic heating due to phase changes of the electrode matrices during intercalation/de-intercalation, (q_{e}) all in $[\mathrm{J}]$. Conservation of thermal energy in the cell therefore dictates a balance between heat accumulation, convective dissipation and heat generation terms:

$$\rho C_{\mathrm{p}}\frac{\partial T}{\partial t} = \frac{\partial}{\partial t}\left(k\frac{\partial T}{\partial x}\right) + \left(q_{\mathrm{r}} + q_{\mathrm{j}} + q_{\mathrm{c}} + q_{\mathrm{e}}\right), \tag{5.76}$$

with boundary conditions $[\mathrm{W\,m^{-2}\,K^{-1}}]$

$$\left.\frac{\partial T}{\partial x}\right|_{x=0} = \left.\frac{\partial T}{\partial x}\right|_{x=L} = \frac{h}{k} A_{\text{o}} \left(T - T_{\text{amb}}\right), \tag{5.77}$$

where ρ is the density of the respective domain in $[\text{kg m}^{-1}]$, C_{p} is the specific heat capacity in $[\text{J kg}^{-1}\,\text{K}^{-1}]$, k is the thermal conductivity in $[\text{W m}^{-1}\,\text{K}^{-1}]$, h is the convective heat transfer coefficient between free air in $[\text{W m}^{-2}\,\text{K}^{-1}]$, A_{o} is the convective surface area exposed to the cooling medium and T_{amb} is the free stream temperature of the surrounding space.

The process of the electrochemical reaction is associated with a heat generation term, referred to as the reaction heat, which is due to the total reaction current overcoming the cell charge-transfer overpotential. This heat generation term includes the contribution from the passivating layers, as these are part of the charge-transfer overpotentials. As there is no reaction taking place in the separator domain, this equation does not apply here.

$$q_{\text{r}} = a_{\text{s}} \int\limits_{x}^{x+dx} i_{\text{t}} \left(\phi^{\text{s}} - \phi^{\text{l}} - E_i^{\text{eq}}\right) dx \tag{5.78}$$

Local ohmic heat dissipation arises from the current in each domain with finite conductivity. The first term on the right hand side of Equation 5.79 represents the ohmic heat dissipation in the electrodes; the second and third terms represents those in the electrolyte phase. Note that while the first and second terms are always positive, the third term is generally negative, since the transport of lithium-ions in the electrolyte leads to a reduction of ionic current in that domain.

$$q_{\text{j}} = a_{\text{s}} \int\limits_{x}^{x+dx} \left[\sigma_{\text{Li}i}^{\text{eff}} \left(\frac{\partial \phi^{\text{s}}}{\partial x}\right)^2 + \kappa_{\text{Li}^+}^{\text{eff}} \left(\frac{\partial \phi^{\text{l}}}{\partial x}\right)^2 + \kappa_{\text{D}}^{\text{eff}} \left(\frac{\partial \ln c_{\text{Li}^+}}{\partial x}\right) \left(\frac{\partial \phi^{\text{l}}}{\partial x}\right)\right] dx \tag{5.79}$$

The contact resistance between electrodes and current collectors, including the effect of binders, gives rise to a further heat term which is applicable only at those locations in the electrode pair.

$$q_{\text{c}} = \left(I_{\text{bat}}\right)^2 \frac{R_{\text{ic}}}{A_{\text{ic}}} \tag{5.80}$$

Host material phase transitions during lithiation and de-lithiation to both electrodes gives rise to a reversible heating term, the entropic heat. It is the only heat term which in itself is a function of temperature.

$$q_{\text{e}} = a_{\text{s}} i_{\text{t}} T \frac{\partial E_i^{\text{eq}}}{\partial T} \tag{5.81}$$

5.11 Assembly of the model

The complete electrochemical model is illustrated diagrammatically in an example implementation of a $LiNi_xCo_yMn_zO_2$ cathode and a LiC_6 anode electrode pair in Figure 5.14, as comprising of three particles in each electrode and three discretisation elements in the separator. All circuit equations are implemented as derived above, including a temperature dependency of the following parameters and functions according to an Arrhenius law: exchange current densities i^0, diffusion coefficients in the electrolyte D_{Li+}, diffusion coefficient in the electrodes D_{Lii}, ionic conductivities κ_{Lii} and double layer capacitances D_i^{dl}.

Circuit layout: The cathode is shown on the right hand side of the model, the anode is shown on the left hand side with the separator region in-between. In this arrangement the anode particle closest to the separator is discharged first, followed by the particles further away. Similarly, the cathode particles closest to the separator are charged first, followed by the particles further away. This allows for the prediction of concentration gradients across the electrode thickness and consequently gradients of all other electrochemical and thermal properties. The electrolyte domain is discretised at each particle location and through the separator, again allowing for species concentration gradients due to mass transport limitations to be predicted across the cell. Ohmic contact resistances R_{e-}^{el} represent the electronic ohmic loss though the cathode aluminium current collector and the anode copper current collector as well as the electronically conducting additives of both electrodes.

Modelling domains: The sub-circuits governing the transport of uncharged species i.e. intercalated lithium is modelled in the chemical modelling domain. Intercalated lithium has a chemical (rather than electrical) potential as it has not yet participated in an electrochemical reaction. Inside the electrodes, resistances oppose the species flux to or from each particle shell to the next and to the electrode/electrolyte interface where the reaction takes place. The potential contained in each shell is represented by capacitances. The intercalated lithium sub-circuits therefore govern the transport and conservation of chemical quantities, such as chemical potential in $[J\,mol^{-1}]$, chemical flux in $[mol\,sec^{-1}]$, chemical resistance in $[J\,s\,mol^{-2}]$ and chemical capacitance in $[mol^2\,J^{-1}]$.

The sub-circuits governing the transport of charged species i.e. (negative) electrons and (positive) lithium-ions are modelled in the electrical modelling domains as these species are the result of the electrochemical reactions. The resistance to lithium-ion flux in the electrolyte from one electrode to the other though the separator is modelled by resistors, while the potential stored in each discretised volume is represented by a capacitor. The lithium-ion and the electron sub-circuits therefore govern the transport and conservation of electrical quantities, such as electrical potential in $[V]$, electrical flux (current) in $[A]$, electrical resistance in $[\Omega]$ and electrical capacitance in $[F]$. The chemical and the electrical domains are linked with a conversion factor of $1/nF$, where n is the number of atoms of each species participating in each reaction (in this model equal to unity).

Special model features: Local electrode surface passivating layers establish and grow during operation due to parasitic side-reaction taking place during reactions. The subsequent build-up of the layer's thickness and its resistance leads to lithium-ions being tied up locally and no longer participating in the redox shuttle; manifesting itself in the form

Figure 5.14: Example implementation of a pseudo 2-D equivalent circuit network implementation. Note, that all capacitance and resistance values in the sub-systems are functions not only of the local states but also of location in the x- and r- directions

of capacity fade. Furthermore, the passivating layer increase progressively leads to an increase of internal impedance observable as power fade.

<u>Triple Species Elements</u> link the chemical sub-circuit (governing uncharged species prior to the reaction taking place i.e. intercalated lithium) and the electrical sub-circuits (governing charged species after the reaction has taken place). Information of the local electrode potential and chemical species flux are coupled to the local electrolyte potential and electron flux just between the electrodes by the TSE. The top edge of each TSE therefore represents the electrical potential of the electrochemical species inside an electrode particle (i.e. the real electrode potential at the interface where the reaction takes place) while the bottom corner represents the chemical potential of the species.

A capacitor representing <u>double-layer capacitance</u> is arranged in parallel with each TSE element and depends on local electrochemistry and temperature. This allows the prediction of local concentrations affecting diffusion to and from the interface and its impact on dynamic cell behaviour. In this parallel arrangement, lithium-ions can only cross over to become intercalated lithium when they participate in a reaction. As described by Equation 5.58, the resistances to chemical fluxes in the electrolyte and electrode are functions of the already stored species concentration. As a result, in a volume with higher concentration a further addition of species requires a higher potential than if it had a low concentration. Local concentration imbalances in either domains therefore lead to chemical fluxes re-balancing though the resistances leading to diffusion overpotential losses. The direction of current flow is indicated for a charge situation resulting in concentration gradients and species fluxes in the radial directions, the direction of which is also indicated. In this case, intercalated lithium de-lithiates from the negative electrode (as indicated by the chemical flux arrow direction) and lithiates into the cathode (again shown by the flux arrow direction) into the particles of the positive electrode.

Sub-circuit layout: As indicated by the schematic of the TSE, each corner is figuratively connected to one of the three species linked by it. While the left-hand side is connected to the electron transport circuit, the right-hand side is connected to the electrolyte transport system and the bottom corner is connected to the transport network inside the electrode. Species transport inside the electrodes and the electrolyte is modelled by RC ladder networks.

Overall cell potential: Recalling the formulation of the electrode/electrolyte interface potentials of each electrode (Equation 5.38) the overall battery operating voltage V_{bat} is obtained as the sum of all the potential drops across the cell. In the order of cathode to anode current collector ohmic loss this can be expressed as

$$
\begin{aligned}
V_{\text{bat}} \quad = \quad & -R_{\text{e}^-}^{\text{el,c}} I_{\text{bat}} && \rightarrow \text{cathode current collector ohmic potential drop} \\
& + \left(\phi_{\text{c}}^{\text{s}} - \phi_{\text{c}}^{\text{l}} \right) && \rightarrow \text{cathode electrode/electrolyte interface potential difference} \\
& - \left(\phi_{\text{c}}^{\text{l}} - \phi_{\text{a}}^{\text{l}} \right) && \rightarrow \text{electrolyte potential difference} \\
& - \left(\phi_{\text{a}}^{\text{s}} - \phi_{\text{a}}^{\text{l}} \right) && \rightarrow \text{anode electrode/electrolyte interface potential difference} \\
& - R_{\text{e}^-}^{\text{el,a}} I_{\text{bat}} \, . && \rightarrow \text{anode current collector ohmic potential drop}
\end{aligned}
$$

Information on electrode equilibrium potential and overpotential contributions can be obtained in the form of a virtual voltmeter. The potential drop and flux at every element

in the circuit retains a physical meaning. In this implementation both electrodes are modelled with the same discretisation, but comprising different parameters. Therefore, although the circuit elements are denoted with the same variable names within each sub-circuit in the figure, their value during operation will deviate due to local operating conditions and a different parametrisation.

5.12   Interim conclusion

The model presented in this section addresses the majority of aspects previously identified as areas of further development

1. In the presented methodology the model is structured into clearly defined physics-based sub-circuits governing individual species' phenomena. Each can be observed separately and parameter evolution compared to other model predictions or, where possible, to experimental data.

2. An electrical analogy is derived for the complex electrochemical reaction process which links the sub-systems of individual species. This allows for a straightforward comparison of electrochemical parameters such as charge-transfer resistance to EIS experimental data. The newly presented phenomenological equivalent circuit network:

   (a) allows for locally variable passivating layer thickness, resistance and capacitance, depending on local electrochemistry and temperature, and

   (b) allows for locally variable double-layer capacitance and potential, depending on local electrochemistry and temperature

3. Previous developments have been extended to include phenomena thus far omitted. These are:

   (a) local temperature variation and the subsequent dependency of local electrochemical processes,

   (b) capacity fade through loss of cyclable lithium, and

   (c) power fade through increase of internal impedance

4. In this model implementation, the dependency on an empirical relation governing the equilibrium potential of each electrode (due to its standard reduction potential and concentration variation) has not been removed yet; however, an approach in order to do so has been provided. The simplicity of the experiments required in order to extract these two functions rendered this method superior for the purpose of automotive applications compared to the detailed half-cell testing and atomic physics analysis that would be required for a fundamentally derived function. This is the only design criterion which has not been fully resolved as was initially anticipated. (Note: the vast majority of models in the literature make the same adaptation of an empirically obtained function to describe electrode equilibrium potential)

5. All phenomenological analogies are linked to local thermal effects and are therefore allowed to vary locally. The resulting local gradients of concentrations, potentials, fluxes and temperatures form additional contributors to the complex electrochemical system.

6. Previous work has been extended upon in terms of visual representation and layout of the network. This allows for straightforward future adaptations, modifications, extension and system-level implementation by system designers.

Chapter 6

Model application and results

Overview

This chapter describes the parametrisation of the model and provides several study outcomes and comparisons between the model, professional desktop modelling software and experimental measurements. Shortcomings in the accuracy of both, the parametrisation and the model outputs, are discussed. The model's capability to simulate cell behaviour under dynamic events from 0% to 100% State-of-Charge conditions is demonstrated with various test procedures. Examples for model output are given for several standard battery testing procedures as well as realistic automotive drive cycle loads.

6.1 Parametrisation of the model

The ultimate goal of the model presented in this work is real-time (or faster) performance prediction of a cell using the already existing basic infrastructure of current, voltage and temperature measurements only. This is with the aim to quantify state of health, level of degradation and remaining battery capacity. Figure 6.1 shows the process of model derivation, parametrisation and simulation and demonstrates the ease of adaptation of the model presented in this work. Bold system variables denote the commonly sole two states monitored on a battery management systems level. The wealth of additional information which can be obtained using this methodology is also shown. This allows the observer to make accurate predictions of current and past cell performance characteristics as well as monitor thermal conditions while in operation. The aim of the implementation in this form is to allow an easy modification by control engineers, BMS designers and vehicle system platform engineers without costly experimental work and macroscopic analysis. For battery materials commonly used by the automotive and portable electronics industry, the parameters required tend to be easily available in the academic literature.

Although an iterative process of parameter optimisation is indicated in the figure, the model and results presented in this thesis are obtained as stand-alone. This means no

fitting to experimental data is performed to optimise the model predictions. The ability to predict battery behaviour based on fundamental phenomenological battery modelling as opposed to empirical methodologies is therefore demonstrated.

Further optimisation of the model's predictions beyond what is demonstrated in this thesis might be achieved by accounting for further chemical and electrical phenomena and processes (see Future work).

Figure 6.1 shows the parameter set required for the model and classifies the variable set into

1. The model parameters which characterise the cell response

2. The input which is measured live and represents the running input variable to the model

3. The output variable set

All of which can be classified according to the circuit network they describe, electron, lithium-ion, lithium-atom and thermal network, as shown in the figure.

The parameters used in the model are obtained from various literature sources, as indicated in Table 6.1. Like in other phenomenological methodologies the model predictions depend highly on the quality of the initial model parameters. Their accuracy and availability is influenced by many factors, such as the actual ability to experimentally measure them (access), the boundary conditions under which they were obtained as well as the age, quality and usage history of the test specimen. Furthermore, material chemical modifications may be trade-secrets, meaning the values obtained from the academic literature might not reflect the true material properties.

The level of discretisation, structure and arrangement of circuit elements in the model may be a further cause of discrepancies between model predictions and experimental data as will be discussed for each study.

6.2   Model implementation

In the following, the phenomenological equivalent circuit model described in Chapter 5 is implemented in Matlab/Simulink in a single-particle and a three-particle configuration. It is compared to solutions provided by a multi-physics modelling solution proposed by Doyle, Newman *et al.* [181, 101] which was implemented by COMSOL Ltd. in the commercial modelling software [182, 183]. Furthermore, model predictions are compared to experimental data, the sources of which are acknowledged accordingly. Different operating regimes are investigated: charge/discharge under constant current (CC), transient regimes and relaxation under pulse load, standard test procedures and a real-world drive cycle in a vehicle application. The cell evaluated in this study is a commercial $LiNi_{1/3}Co_{1/3}Mn_{1/3}O_2$

chemical
description of
battery processes

Modification of chemical description

mathematical
description of
considered processes

Modification of mathematical description

Model modification

Electron transport network

Passivating layer resistance R_i^{pl}
Current collector resistance R_i^c $R_c^{e^-}$

Lithium transport in electrode network

Stoichiometric extremes $x_{0,i}$, $x_{100,i}$
Maximum electrode lithium concentration $c_{\text{Li}_{max},i}$
Electrode diffusion coefficient $D_{s,i}$
Lithium insertion rate constant $k_{0,i}$
Charge transfer coefficient $a_{a,i}$, $a_{c,i}$
Reference exchange current density $i_i^{0,ref}$
Active particle surface area $a_{s,i}$
Solid phase conductivity $\sigma_{s,i}$
Active material volume fraction $\varepsilon_{s,i}$
Particle radius $r_{s,i}$

Lithium transport in electrolyte network

Equilibrium electrolyte lithium concentration c_{Li^+}
Electrolyte diffusion coefficient $D_{\text{Li}^+,i}$
Conductive filler volume fraction $\varepsilon_{f,i}$
Electrolyte phase volume traction $\varepsilon_{e,i}$

Thermal network

Activation energies E_{i0}, E_D, E_{ka}
Specific heat capacities $C_{p,i}$

Modification of parameter values

Parameter optimization

running input (live measurements)
Current I_{bat}

cross check (live measurements)
Cell operating voltage V_{bat}
Local temperature T_j

Simulation

Comparison of simulation outputs with measurements

Cell operating voltage V_{bat}
State of Charge SoC

Lithium concentration bulk $c_{\text{Li}^+,b,i}$
Lithium concentration surface $c_{\text{Li}^+,s,i}$
Stoichiometry x_i
Equilibrium potential E_i^{eq}
Debye length λ_i
Double layer capacitance C_i^{dl}
Exchange current density i_i^o
Electrochemical reaction rate j_i

Electrode potential ϕ_i^s
Electrolyte potential ϕ_i^l

Passivating layer overpotential η_i^{pl}
Activation overpotential η_i^{act}
Lithium-ion diffusion overpotential $\eta_{\text{Li}^+}^d$
Intercalated lithium diffusion overpotential $\eta_{\text{Li},i}^d$
Charge transfer overpotential η_i^{ct}

Electrode lithium concentration $c_{\text{Li},i,i}$
Electrolyte lithium concentration $c_{\text{Li}^+,i}$

Local temperature T_i
Reaction heat $q_{r,i}$
Ionic ohmic heat $q_{j,}$
Entropic heat $q_{e,}$
Contact ohmic heat $q_{c,i}$

Figure 6.1: Schematic demonstrating model parametrisation and optimisation iteration

graphite pouch cell SLPB 11043140H (5 Ah) by Dow Kokam. A single-particle imple-
mentation and a three-particle implementation are shown in Figure 6.2 and Figure 6.17
respectively.

Figure 6.2: Example implementation of a single-particle implementation example of the
new phenomenological model. Note, that all capacitance and resistance values in the
sub-systems are functions not only of the local states but also of location in the x- and
r- directions. Each particle has been discretised into four concentric shells while the
electrolyte has been discretised into three segments in the separator and one segment in
each electrode

In this model an initially healthy cell is assumed in a like-for-like comparison with the

cell parameters from the literature assumed to be accurately reflecting the Kokam cell chemistry. The parameter values of the real cell are also common to both simulations and are listed in Table 6.1. As mentioned previously, it is technically possible to refine these values by numerical optimisation in order for the simulation results to fit closer to experimental data, although this is not part of the scope of this thesis.

The thermodynamic potential as a function of the anode stoichiometry is obtained from the literature [184, 142], whereas the equation for the cathode is obtained as the difference of a near-OCV experiment (conducted at C/20 on the same cell) and the anode thermodynamic potential (Figure 6.3). Note the Kokam 5 Ah battery stoichiometric range from $x_{0\%} = 0.98$ and $x_{100\%} = 0.363$ [184]. This specified range indicates that the cyclable range, meaning the rated nominal capacity of the cell overall, is only about 50% of the total capacity of the positive electrode for this cell. Some of this 'over-engineered' weight of 50% could perhaps be accessed in a non-degradation inducing way by optimising the cell's charging and discharging strategy and by avoiding specific degradation-inducing battery states. The phase transition points on the positive electrode can also clearly be seen in Figure 6.3 at around $x = 0.95$ and $x = 0.65$ (where the equilibrium potential curve exhibits a change in slope).
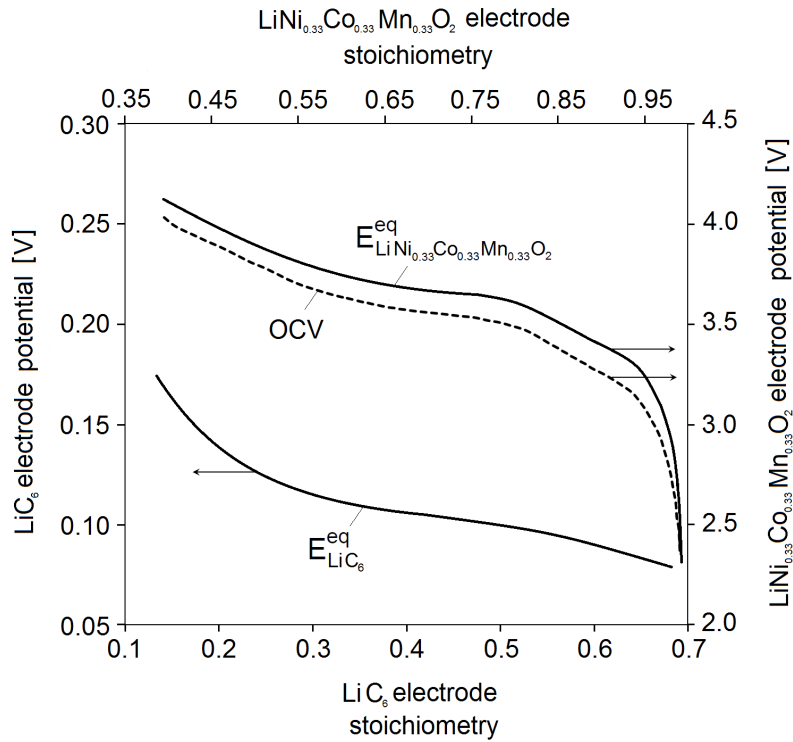
Figure 6.3: Thermodynamic potential equations for anode and cathode over their stoichiometric ranges [7]

A further feature of the positive and negative electrode potentials is their respective potential ranges. While the anode equilibrium potential ranges from $0.08\,\mathrm{V} - 0.175\,\mathrm{V}$ during discharge the cathode equilibrium potential ranges from $4.28\,\mathrm{V} - 2.875\,\mathrm{V}$ and exhibits a rapid drop in potential at low SoC. The flat nature of the resulting OCV curve means that predictions at the middle of the SoC range have to be obtained under tight error tolerances (as a small voltage deviation may lead to a large SoC error), and

that on-line predictions at high SoC have to be made fast to avoid over-discharge during operation. These arguments highlight the importance of the accurate parametrisation of equilibrium potential equations of both electrodes (but especially the cathode) as the basis of the model to avoid estimation errors.

6.3   Constant discharge/ constant charge

The C/2, 1C, 2C, 10C and 20C discharge and C/2, 1C and 2C charge test procedures were conducted in a thermally controlled environment at room temperature using a potentiostat (HCP/1005 Bio-Logic) with a 100 Ampere booster. The procedure before each experimental procedure was a full charge (4.2 V; SoC=100%) or a full discharge (2.4 V; SoC=0%) with a constant current of 1C, followed by a Constant Voltage (CV) charge until the charge current reached C/20, and by a rest period of two hours.

ECN simulation predictions and experimental data of these procedures can be seen in Figure 6.4. The simulation results show good agreement with the experimental data. Overall errors amount to less than 9% for the case of a 20C discharge, which was deemed sufficiently accurate for automotive applications. It can be seen that in both the model predictions and the experimental data, the visible phase transition features fade away at increasing C-rate, which is attributed to the shorter duration of the charge/discharge processes leading to a more gradual transition between phases and the more frequent occurrence of co-existing phases over the whole operating range. Only accounting for diffusion overpotentials resulting from two species (of Li$^+$ and Lii) might not suffice at high C-rates, but the transport of species in various other phases might have to be accounted for as this perhaps impacts on local diffusion coefficients.

The simulation error encountered during charge appears to be slightly larger than during discharge. One possible reason for this could be that the charge-transfer coefficients (α) describing the rate of the electrochemical forwards and backwards reactions are not exactly equal in reality.

The deviations occur predominantly at the higher charge C-rates. Although the model allows for heat generation and is thermally coupled at each spacial discretisation, the heat dissipation to the outside might be the reason for the slight deviation from experimental data at high C-rates.

In addition, errors in model parameters might cause a slight overestimation of temperature increase as will be shown in Section 6.4. This temperature overestimate leads to an overestimation of the rate of electrochemical reactions, meaning the model allows a current at a lower charge transfer resistance than the real cell. Furthermore the increasing error at low SoC may be attributed to an inaccurate cathode equilibrium potential, the significance of which becomes most visible at a high cathode stoichiometry. Similarly, during charge the charge-acceptance is overestimated slightly, which again may be attributed to errors in the equilibrium potential equations or external cell cooling effects by convection which might have been underestimated in the model.

Design Specifications	Symbol	Unit	Anode current collector	Anode	Separator	Cathode	Cathode current collector
Particle radius [142]	$r_{p,Lii}$	m	-	1.0e-6	-	1.0e-6	-
Active material fraction [185]	ε_s	-	-	0.58	0.55	0.50	-
Conductive filler volume fraction [185]	ε_b	-	-	0.33	0.55	0.33	-
Polymer phase volume fraction [185]	ε_{Li+}	-	-	0.04	-	0.06	-
Maximum electrode lithium intercalation concentration [186]	$c_{Lii,max}$	$\mathrm{mol\,m^{-3}}$	-	16.10	-	23.9	-
Stoichiometry at 0% SOC [142]	$x_{0\%}$	-	-	0.126	-	0.978	-
Stoichiometry at 100% SOC [142]	$x_{100\%}$	-	-	0.676	-	0.393	-
Equilibrium electrolyte concentration [168]	c_{Li+}^{eq}	$\mathrm{mol\,m^{-3}}$	-	1.2e3	1.2e3	1.2e3	-
Kinetic and transport properties							
Charge-transfer coefficient [168]	α_a, α_c	-	-	0.5	-	0.5	-
Passivating layer resistance (initial) [187]	R^{pl}	$\Omega\,\mathrm{m}^{-2}$	-	1.0e-4	-	1.0e-5	-
Passivating layer ionic conductivity [188]	κ^{pl}	$\mathrm{S\,m^{-1}}$	-	5.0e-6	-	5.0e-6	-
Passivating layer molar mass [188]	M^{pl}	$\mathrm{kg\,mol^{-1}}$	-	0.162	-	0.162	-
Passivating layer density [188]	ρ^{pl}	$\mathrm{kg\,m^{-3}}$	-	1690	-	1690	-
Electrode diffusion coefficient Lii [189]	D_{Lii}	$\mathrm{m^2\,s^{-1}}$	-	4.0e-14	-	8.0e-18	-
Electrode electronic conductivity [142]	σ_{Lii}	$\mathrm{S\,m^{-1}}$	-	100	1.3	10	-
Bruggeman porosity exponent [142]	Brugg	-	-	1.5	1.5	1.5	-
Electrolyte diffusion coefficient [189]	D_{Li+}	$\mathrm{m^2\,s^{-1}}$	-	1.7e-10	1.7e-10	1.7e-10	-
Electrolyte activity coefficient [142]	$f_\pm$	-	-	1.0	1.0	1.0	-
Li$^+$ transference number [142]	t_+^0	-	-	0.363	0.363	0.363	-
Exchange current density activation energy [168]	$E_{i_{Lii}^0}$	$\mathrm{J\,mol^{-1}}$	-	3.0e4	-	3e4	-
Electrode diffusion activation energy [168]	$E_{D_{Lii}}$	$\mathrm{J\,mol^{-1}}$	-	4.0e3	-	2.0e4	-
Electrolyte diffusion activation energy [168]	$E_{D_{Li+}}$	$\mathrm{J\,mol^{-1}}$	-	1.0e4	1.0e4	1.0e4	-
Electrolyte conductivity activation energy [168]	E_{κ_a}	$\mathrm{J\,mol^{-1}}$	-	2.0e4	2.0e4	2.0e4	-
Geometric parameters							
Domain thickness [142]	δ	m	1.2e-5	40e-6	20.32e-6	29.12e-6	2.1e-5
Electrode plate area [142]	A_f	$\mathrm{m^2}$	-	-	1.0452	-	-
Area specific current collector resistance [190]	R_c	$\Omega\,\mathrm{m}^2$	1.0e-3	-	-	-	1.0e-3
x-direction length of cell [191]	L_x	m	-	-	0.140	-	-
z-direction length of cell [191]	L_z	m	-	-	0.041	-	-
Thermal parameters							
Thermal conductivity [192]	k_t	$\mathrm{W\,m^{-1}\,K^{-1}}$	398	1.04	0.334	1.58	238
Density [192]	ρ	$\mathrm{kg\,m^{-3}}$	8440	1347	1009	2329	2610
Heat capacity [192]	C_p	$\mathrm{J\,kg^{-1}\,K^{-1}}$	385	1438	1979	1269	904

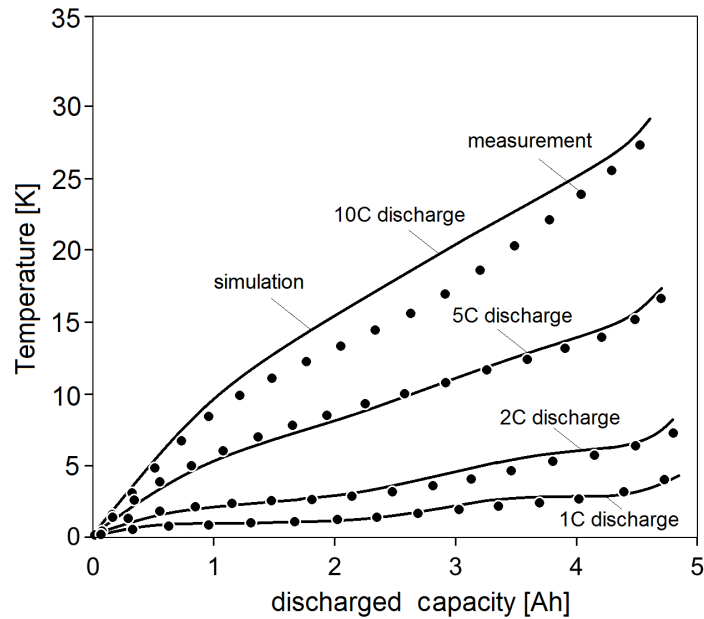Table 6.1: *Battery simulation parameters resembling the Kokam 5 Ah cell*

Figure 6.5: Comparison of model predictions against experimental data of temperature increase from a homogenous 20C starting temperature for 1C, 2C, 5C and 10C discharge procedures. Experimental data collected by Yu Merla
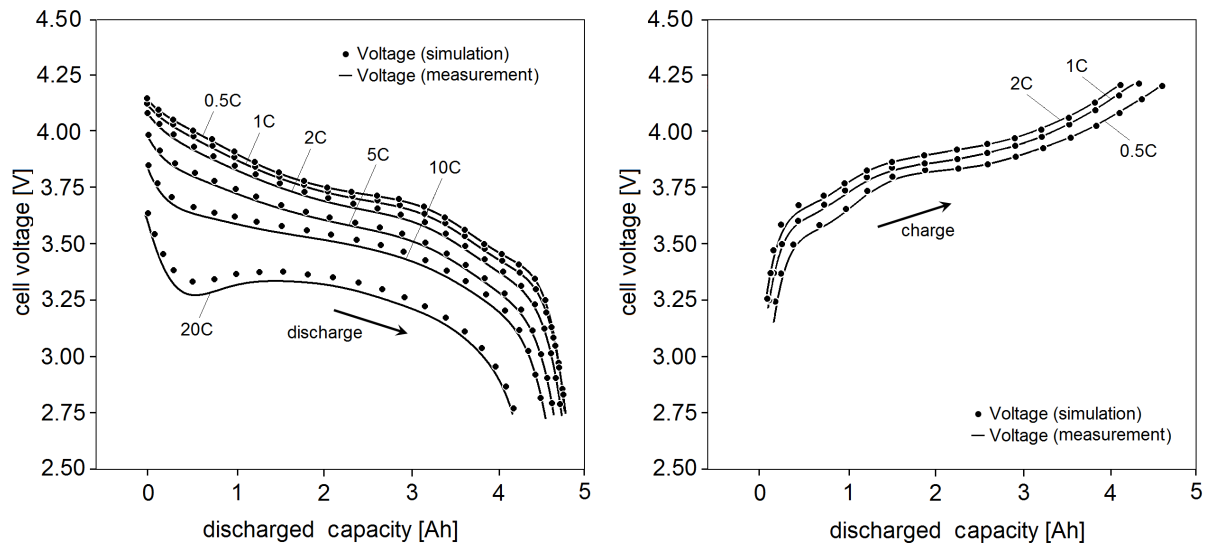

Figure 6.4: Comparison of model predictions and experimental data of various discharge (left) and charge (right) C-rates. Experimental data collected by Yu Merla

6.4   Temperature increase during constant charge

The temperature increase encountered during the 1C, 2C, 5C and 10C discharge procedures is shown in Figure 6.5 with experimental data shown in comparison.

All data traces exhibit non-linear temperature increases which are partly due to entropic heat contributions as well as the non-linear increase of charge transfer resistances, as

will be shown later. The overestimations at higher discharge rates could be due to the difficulty in maintaining the same thermal boundary conditions in the experimental test set-up and in the model. Furthermore, it is expected that the heat generation inside the cell will differ in reality as there are many electrode pairs stacked rather than just one (like in this model configuration).

6.5 Overpotential contributions

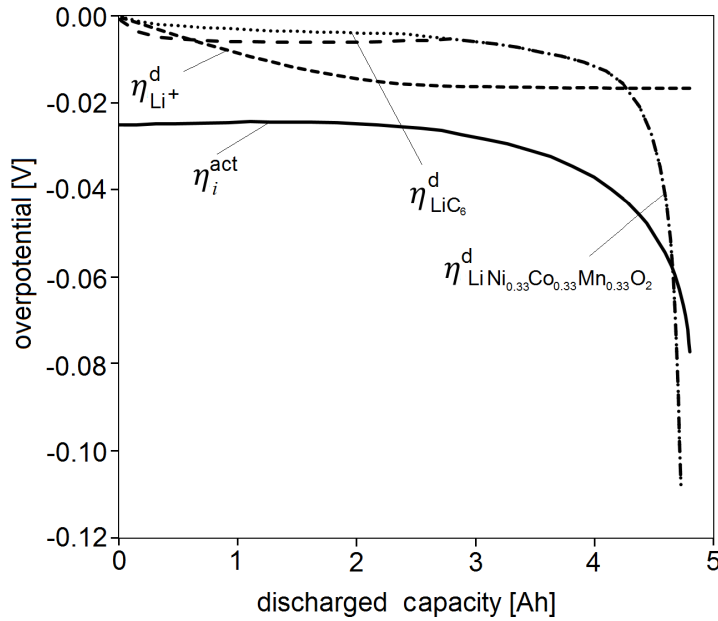The various diffusion overpotential contributions during a full 1C discharge are shown in Figure 6.6.

Figure 6.6: Model predictions of activation overpotential (solid line) and diffusion over-potentials (dotted lines) during a 2C discharge

It can be seen that, during most of the discharge, total overpotential is dominated by the activation potential between Li^+ and Li*i* and the diffusion overpotential of Li^+ in the electrolyte. The diffusion overpotential contributions due to Li*i* mass transport in the electrodes are relatively insignificant at high to medium SoC. These become very significant at low SoC. This is in line with the very high internal impedance observed at low states of charge (see Figure 6.9).

6.6 Heat generation terms

The heat generation associated with the overpotentials during a 2C discharge is shown in Figure 6.7. The entropic heat contributions from anode and cathode can clearly be seen to take a negative value, which is due to energy being consumed in the endothermic processes

during lithiation and de-lithiation. Both reaction heat contributions (anodic/cathodic) are always positive and sharply increase towards zero SoC which is due to the sharp increase of the electrode charge transfer overpotentials (as previously seen in Figure 6.6). Upon discharge, as more lithium is extracted from the negative electrode and more lithium is pushed into the already nearly full positive electrode, the more difficult this process becomes as nearly all lattice sites are already occupied.
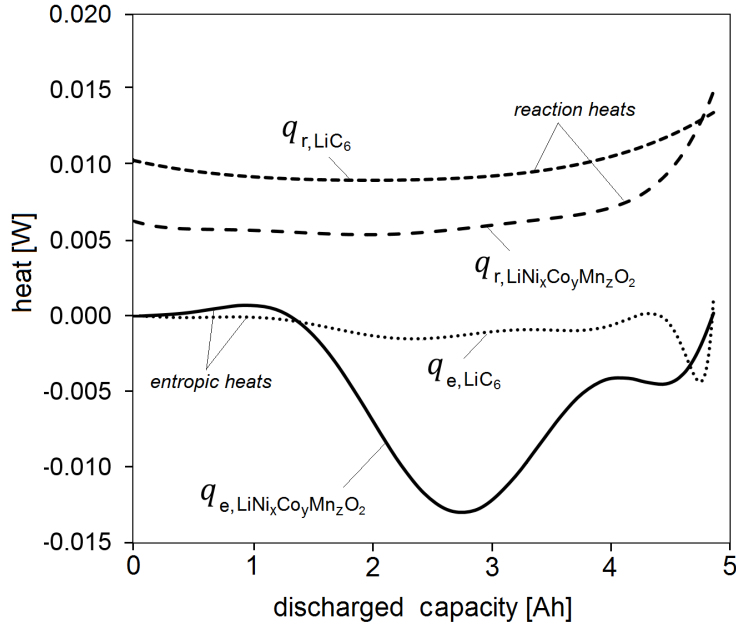

Figure 6.7: Model prediction of heat generation during a 2C discharge: entropic heat generation q_e and reaction heat q_r generation in the anode and cathode. Experimental data collected by Yu Merla

6.7 Phase transitions DTV

More details of the underlying phase transition phenomena in the positive and negative electrode can be revealed with a technique called differential thermal voltammetry [167]. A galvanostatic charge/discharge is performed while measuring cell temperature and voltage. For low C-rates, when overpotentials are relatively small, the ratio of temperature differential and voltage differential $dT.dV^{-1}$ reveals locations of phase transitions, which affect entropic heat generation. A large $dT.dV^{-1}$ value indicates that a small change in voltage leads to a large change in temperature, which has been shown to be an inherent characteristic exhibited by a phase transition in the electrode intercalation matrix [191]. For more detail on this technique the reader is referred to [167, 191]. Both the experimental and the simulation data were generated at 2C and show quite good agreement.
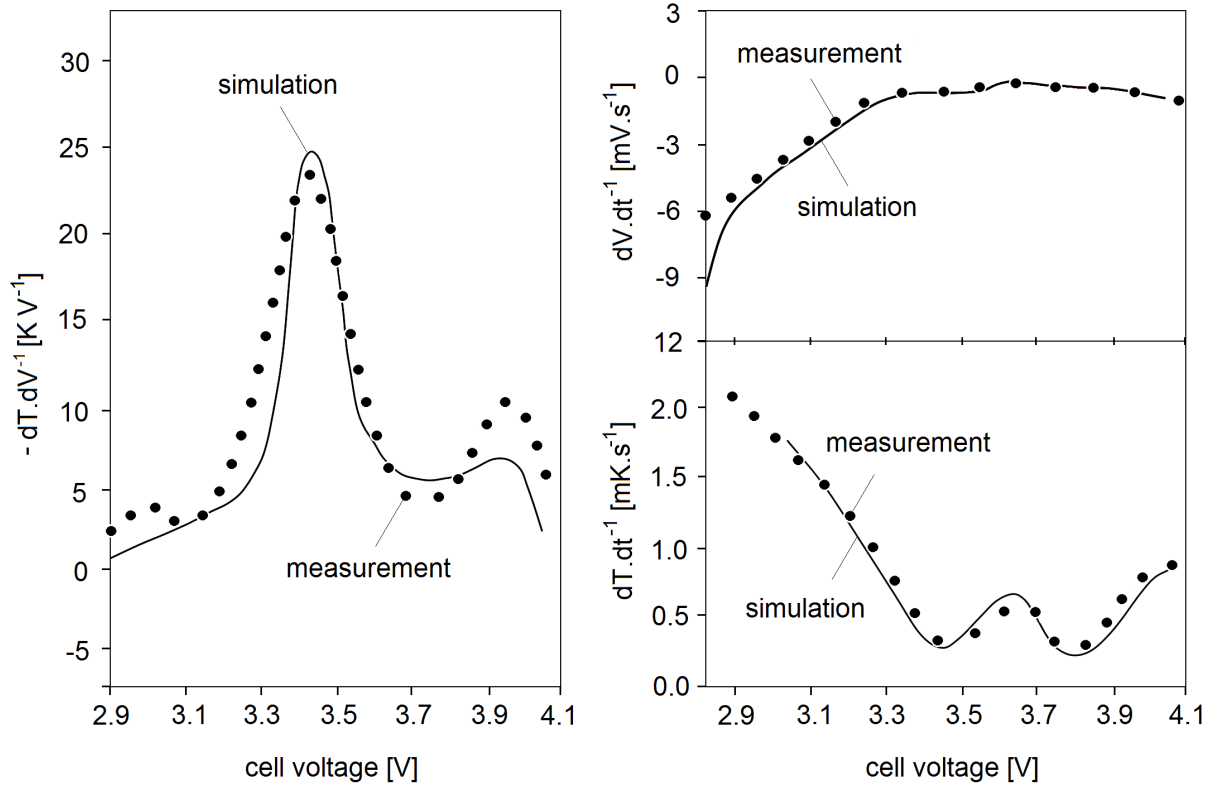
Figure 6.8: Comparison of model predictions and experimental data of differential thermal voltammetry at 2C. Experimental data collected by Yu Merla

6.8 Electrochemical Impedance Spectroscopy

An Electrochemical Impedance Spectroscopy analysis at various SoC levels was carried out to capture the dynamic impedance characteristics of the Kokam cell. These measurements were performed with a Biologic VSP potentiostat with a 200 mA RMS AC current sine oscillation. This amplitude of 200 mA was deemed to be large enough to reduce signal noise and small enough to maintain a linear system. The analysis frequency range was chosen to capture all physical phenomena of interest, which from previous work on lithium-ion impedance characterisation was found to be 100 kHz to 0.01 Hz [193, 194]. Further to this, the data was processed to extract circuit fitted parameters. The circuit used is shown in Figure 6.9.
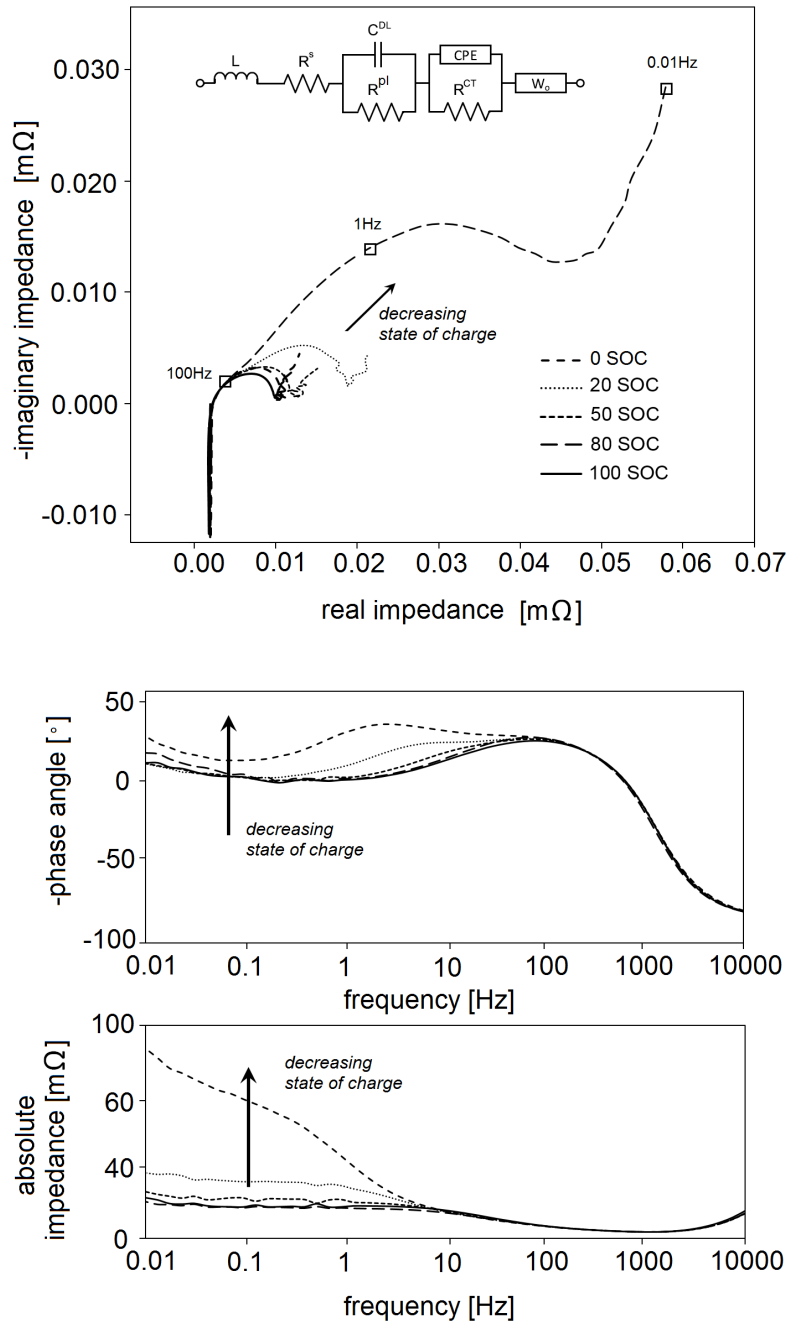
Figure 6.9: EIS data of the Kokam 5 Ah cell under load and the equivalent circuit used for parameter fitting in order to allow a comparison of various parameters in this chapter. Experimental EIS data collected by Yu Merla, the fitted EIS equivalent circuit parameters used in several studies in this section are derived from these measurements and are hereby acknowledged [8]

This circuit was adopted from [195, 196] with each circuit parameter aiming to encapsulate a different (and if possible distinctive) electrochemical phenomenon. The circuit parameters were extracted using the curve fitting algorithm in ZView by Scriber Associates, the numerical parametrisation techniques of which are detailed in [197]. The large impedance increase between 20% SoC and 0% SoC stemming from the sharp overpotential

increases discussed earlier can be clearly seen.

A comparison of the experimental data fitted ECN parameters and the simulated data is shown below for several resistance parameters.
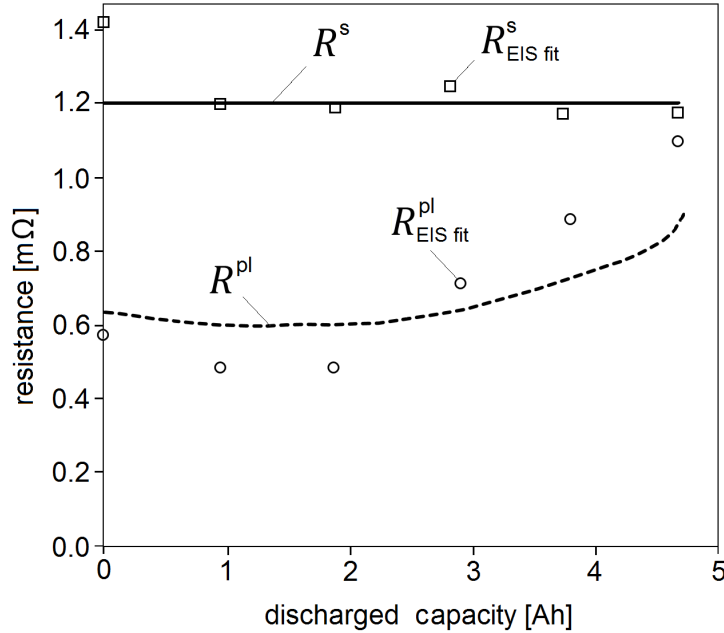

Figure 6.10: Comparison of (lines) model predictions and (symbols) EIS fitted equivalent circuit parameters of the cumulative effect of passivating layer and series resistances. The model enables the prediction of passivating layer and series resistance for each electrode separately. The contributions of each electrode are subsequently added (as they occur in series) to allow for a comparison with the EIS predictions

In Figure 6.10 the simulated series resistance R^s is compared to that of the ECN fitted to the EIS data $R^s_{EIS\,fit}$ over the whole discharge range. Given the very small change in series resistance, this parameter was set to be constant in the model. In future modifications of this model, a gradual increase of internal impedance could be accounted for to account for degradation mechanisms like corrosion, interface resistances etc. affecting shelf life, as will be highlighted in Section 6.13. Similarly the simulated passivating layer R^{pl} (of both anode and cathode lumped) is compared to the of the EIS fitted ECN $R^{pl}_{EIS\,fit}$. It can be seen to increase over discharged capacity. This is due to the continuous growth of the passivating layer as a function of exchange current and side-reaction exchange current. The discrepancies between model prediction and EIS data might be due to contributing factors to passivating layer growth which have so far not been accounted for, such as passivating layer break-down and re-formation. A further source of discrepancy could be the EIS circuit fit.

The contributions to diffusion resistance leading to the diffusion overpotentials are shown in Figure 6.11. As mentioned previously, the resistance to further intercalation and de-intercalation increases progressively towards zero SoC which is apparent in the very high total internal impedance at that point, as shown in Figure 6.12. The effect is further exaggerated by the sharply increasing overall activation overpotential towards zero SoC.
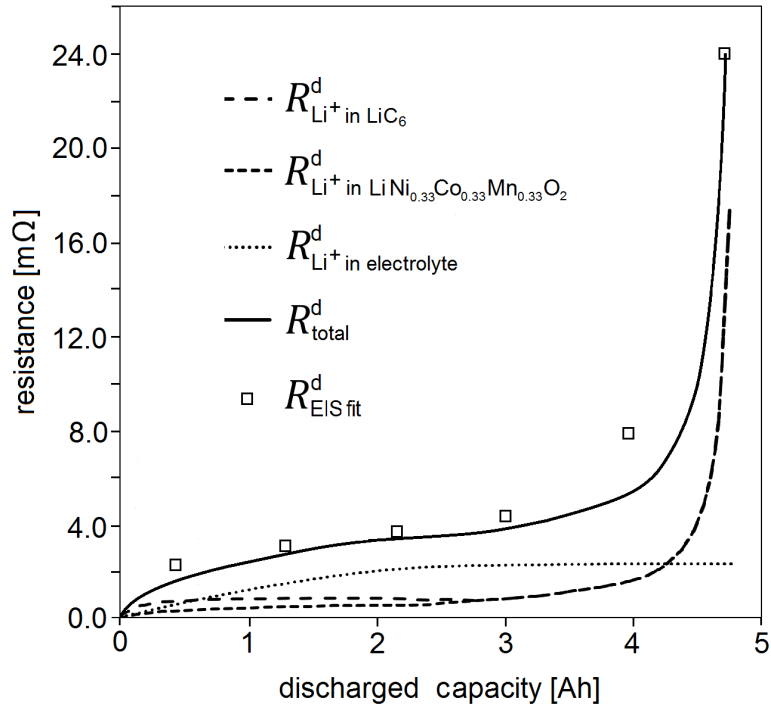
Figure 6.11: Comparison of (lines) model prediction and (symbols) EIS fitted data of diffusion resistances from lithium transport in anode, cathode and electrolyte

The total internal impedance is never zero which is due to the never-zero passivating layer resistances, series resistances and activation overpotentials. Furthermore, it can be seen that the simulation overestimates both charge-transfer resistance and total internal impedance at high to medium SoC, while predicting these two parameters with greater accuracy at low SoC. This, again, might be attributed to slight inaccuracies in the model parameters, a non-perfectly symmetrical forward and backwards reaction or errors in the EIS element fitting. Since an erroneous prediction of cell characteristics at low SoC can potentially have the more detrimental effect of allowing over-discharge, a better fit for low SoC is preferred to a better fit at high SoC.
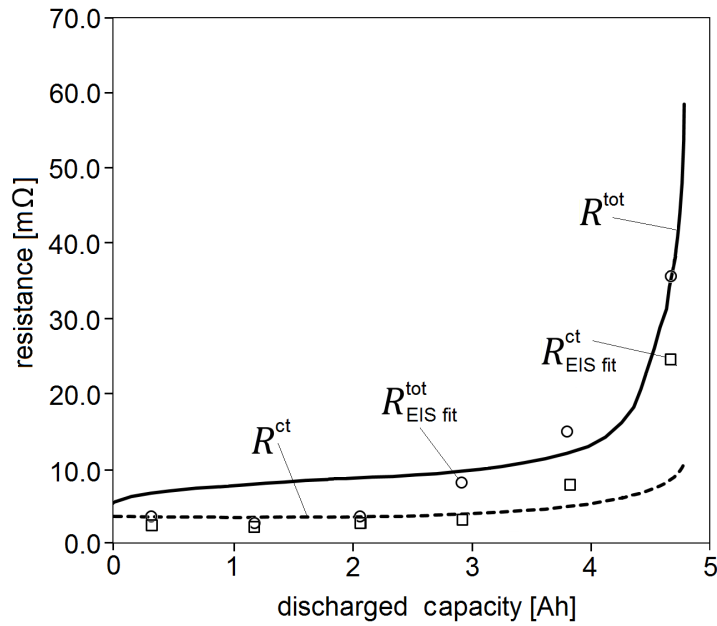
Figure 6.12: Comparison of model prediction and EIS fitted data of (dotted) charge transfer resistance and (solid) total resistance

As can be deduced from the equivalent circuit in Figure 6.9 used for fitting, there is only one circuit branch. Accordingly, only one exchange current trace may be obtained from this circuit where anodic and cathodic phenomena are 'lumped' into one. The newly proposed ECN is able to predict anode and cathode exchange current densities as separate quantities, shown in Figure 6.13.

Figure 6.13: Comparison of (solid) model prediction and (symbols) EIS fitted data of exchange current at anode and cathode

The evaluation of exchange current density at anode and cathode separately is important

for the further calculation of side reaction current densities which result in the accumulation of lost cyclable material in the passivating layer (discussed in Section 5.6). It therefore allows the prediction of capacity fade as a function of lost active material which no lon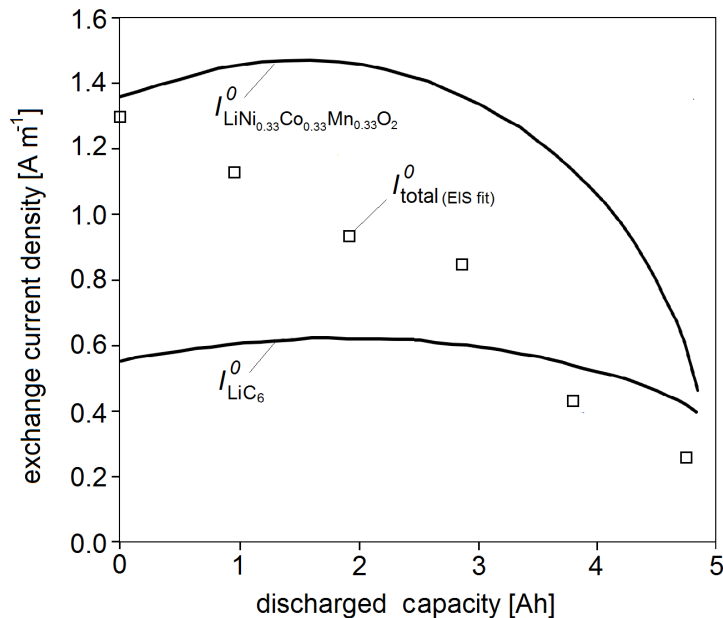ger shuttles between anode and cathode. Figure 6.14 shows a comparison between experimentally obtained capacity fade over 800 cycles and simulated data.

The cell was subjected to a 6C discharge followed by a 2C charge for 800 cycles including a log cycle at 1C discharge every 50 cycles. Furthermore, the cell tab temperature was maintained at 25^0C by clamping it between two continuously PID controlled Peltier elements. The results presented are obtained by applying the same input and boundary to the model as to the experimental test cell. For a detailed description of the test rig the reader is referred to Troxler *et al.* [198].
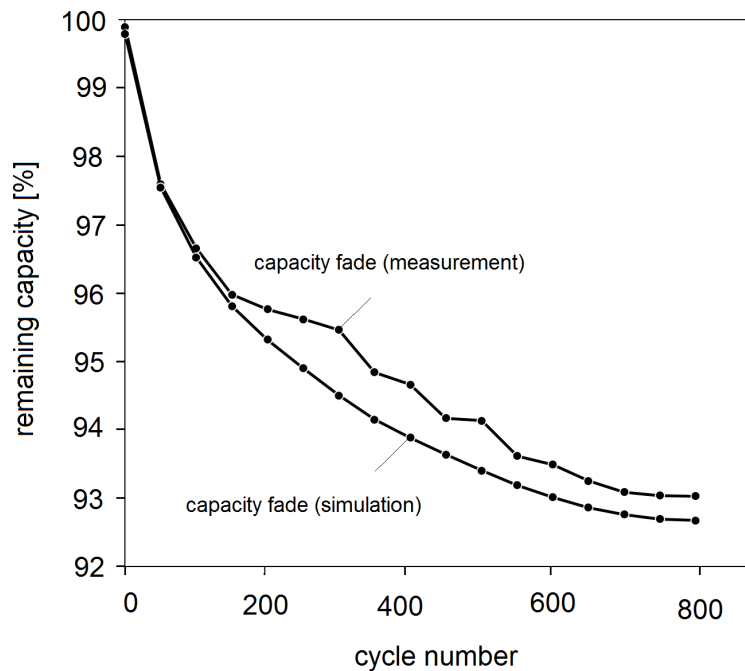

Figure 6.14: Comparison of model prediction and experimental data of cell capacity fade over 800 cycles. Experimental data obtained by Yan Zhao, publication in process [9]

The comparison is made under the assumption that this form of degradation is the only one present in the real cell. Many others may have affected capacity fade although the good agreement between simulated and experimental data gives confidence that this is indeed the main degradation mechanism. The experimental data was collected using a fresh off-the-shelf cell, allowing a like-for-like comparison. The underestimation of the onset of capacity fade might be due to an underestimation of the significance of temperature gradients between individual electrode pairs. Since the model used in this chapter reflects the behaviour of a single electrode pair, the temperature gradient though each material segment thickness brought on by a neighbouring electrode pair (or the position of the electrode pair within the cell) might be underestimated.

Accordingly, a further discretisation and the addition of multiple electrode pairs might yield a better fit of capacity fade prediction of the model and experimental data, and is hence suggested future research.

Furthermore, heat might dissipate away from the surface better than predicted by the model. A consequently higher heat generation in the model results in an acceleration of the electrochemical reactions during cycling, and consequently speed up the onset of degradation. This might yield a better fit of capacity fade predictions, especially for cycling regimes including more aggressive C-rates than the ones included in this test procedure.

6.9 CC-CV charge procedure

Figure 6.15 shows simulation data of a CC-CV charging procedure as well as experimental data under the same conditions. This charging regime is very common in battery applications and commonly forms the procedure at the end of charge regime. As the cell is charged with a constant current (CC) and the cell terminal voltage reaches a threshold, a variable ('trickle') current is applied in order to maintain a constant voltage (CV) at which the cell remains even once the charging current is removed and the cell has relaxed to equilibrium. As this procedure is usually initiated towards 100% SoC it is important to be able to predict and avoid overcharging.
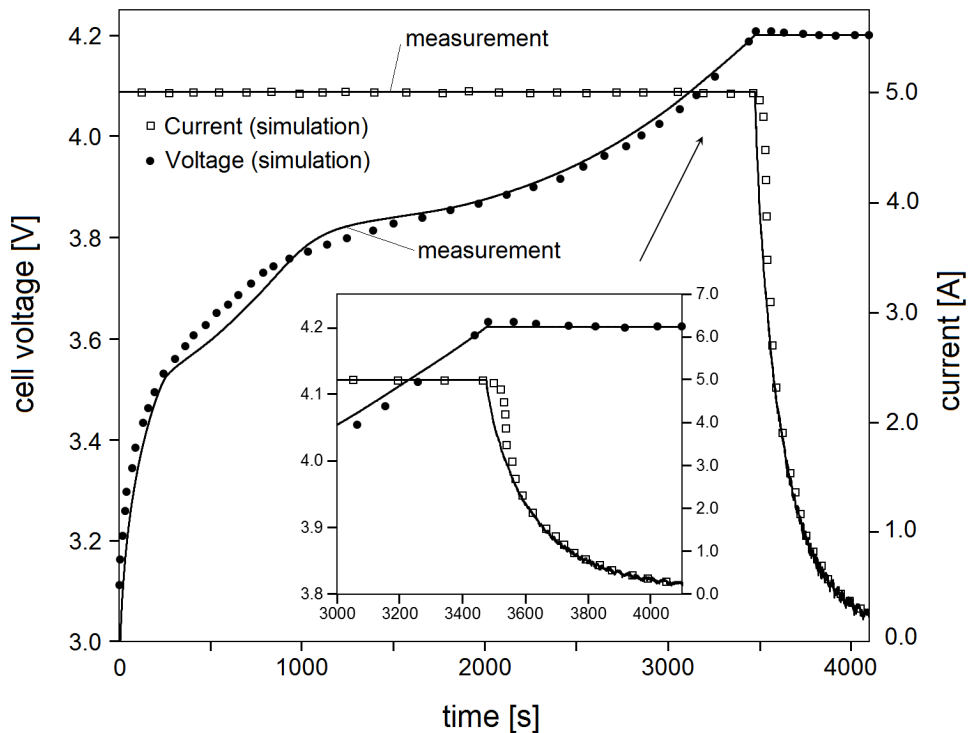
Figure 6.15: Comparison of model prediction and experimental data (solid symbols) of cell terminal voltage for a 1 C CC charge followed by a 4.2 V CV procedure at room temperature allowing free heat dissipation. The load applied to the test cell (dashed line) is compared to the current calculated from the predicted cell voltage and the predicted internal impedance $I = V_{\mathrm{bat}}/R_{\mathrm{int}}$

The figure shows a good fit of simulation versus experimental data. The overshoot at the end of the CC regime may be attributed to potentially different thermal conditions

of the test cell and the model. At the end of the charge the experimental cell might have accumulated more heat, accelerating the electrochemical processes and making it more responsive to a change in applied load. The model, on the other hand, is less responsive as it over-estimates heat dissipation. The electrode pair therefore appears to be cooler, making its electrochemical kinetics slower.

6.10 Pulse discharge/charge procedure

The simulation results and experimental data of a charge/discharge pulse test procedure pulse of 170 s duration is shown in Figure 6.16: a 5C discharge (20 s) is followed a by an open-circuit relaxation period (90 s), a 5C charge (20 s) and an open-circuit relaxation period (30 s). The results of the ECN can be seen to be in relatively good agreement with the experimental data.
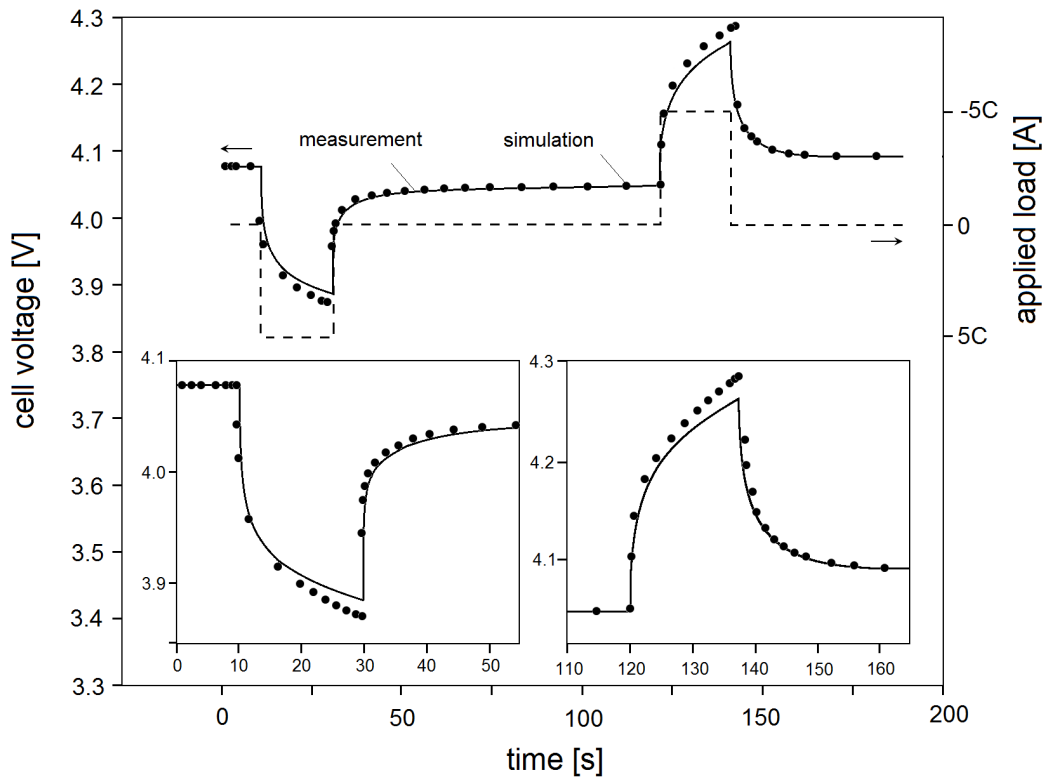

Figure 6.16: ECN model predictions of cell voltage compared to experimental data

The ability to predict lithium concentration and distribution through the system under application of the pulse regime (Figure 6.16) is demonstrated in Figures 6.18 - 6.19 in a 3-particle anode/3-particle cathode configuration which was shown previously in Chapter 5 (but is here reprinted for convenience).
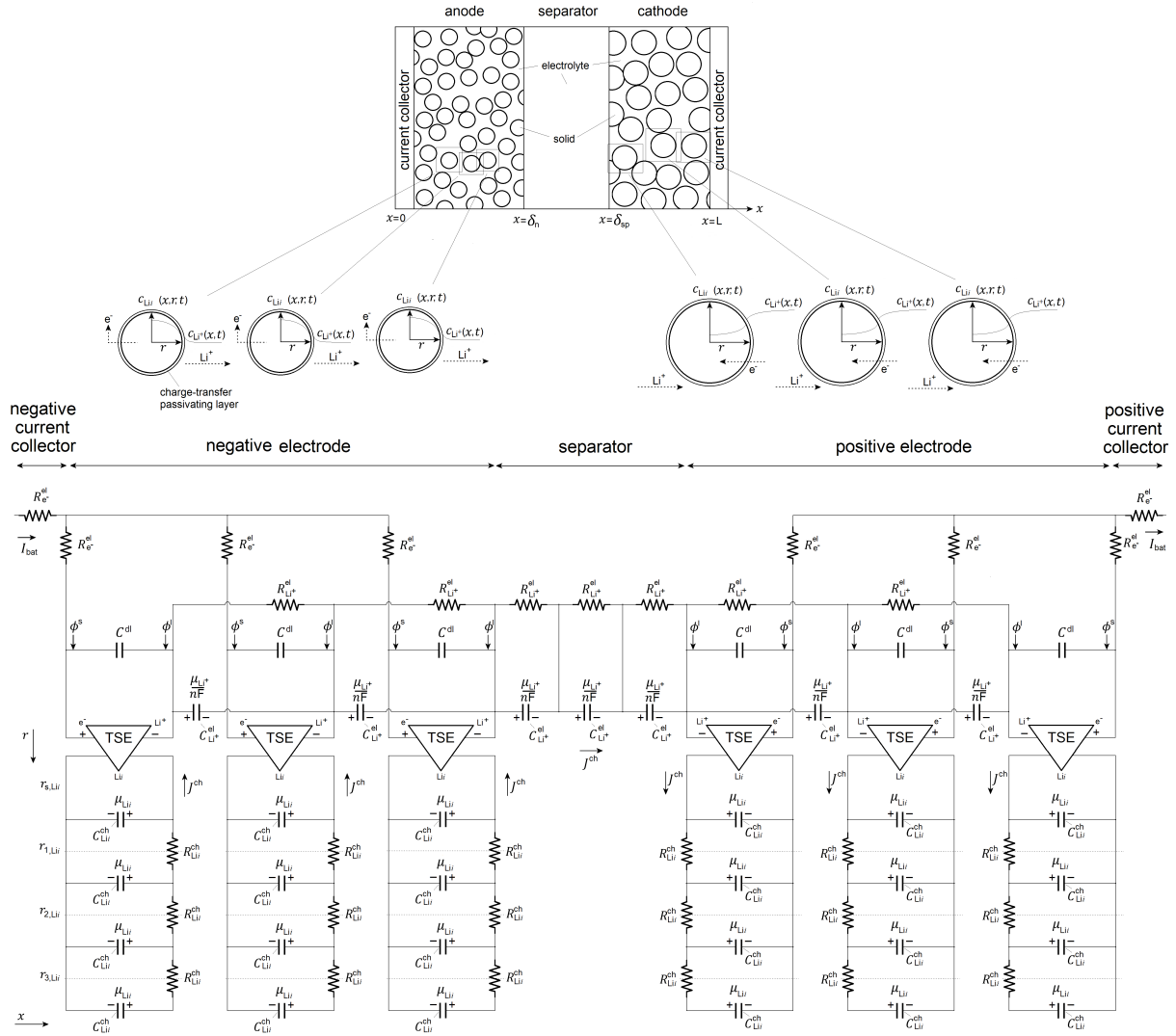
Figure 6.17: Example implementation of a three-particle network. Note, that all capacitance and resistance values in the sub-systems are functions not only of the local states but also of location in the x- and r- directions

The simulation is compared to model outputs of a COMSOL model implementation or experimental data (where parameters can be physically measured). Both simulations were run with the same discretisation and initial conditions, using the same computational power/capability (Intel i5-3317U CPU@ 1.7GHz, 8.00GB RAM). Given the accuracy demonstrated at this level of discretisation (discussed in the following studies), no further sensitivity analysis on particle number was performed; leaving an area for future work. Figure 6.18 shows the evolution of lithium-atom concentration in the electrode particles closest to the current collectors. Each particle is discretised into five concentric shells.

Lithium concentration balances out upon load removal due to diffusion and the inner regions replenish the surface region in both anode and cathode. As can be seen, the model predicts well the relaxation of the cell towards equilibrium conditions upon load-removal. The discrepancy between the model prediction and experimental data may, again, be attributed to the possible difference in thermal boundaries applied to the model and the
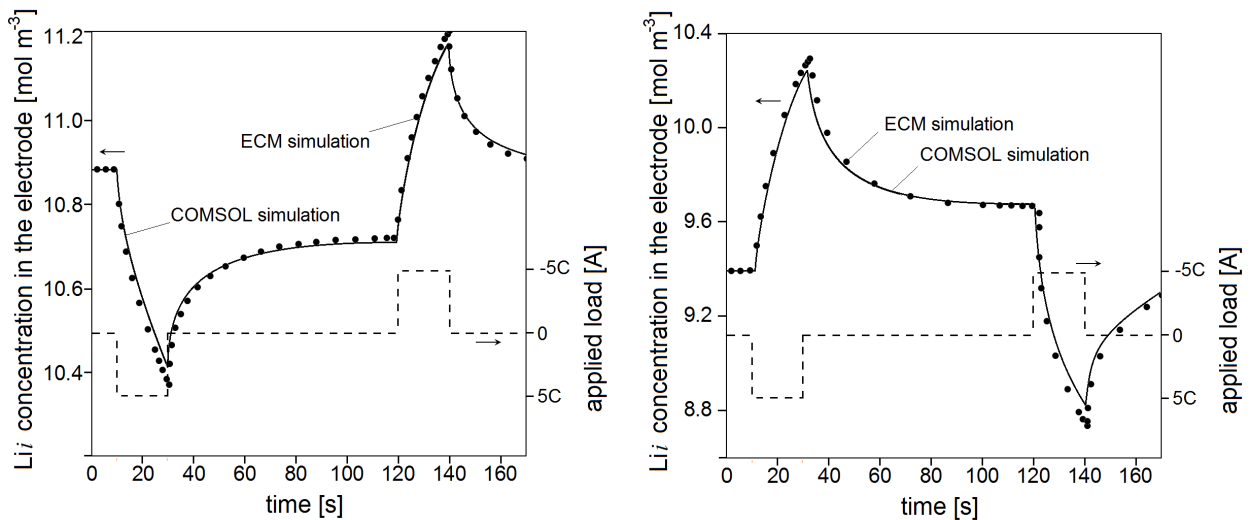
Figure 6.18: Time evolution of lithium concentration inside an electrode particle of a) anode and b) cathode under application of pulse regime shown in comparison with COMSOL results

test cell. While the model electrode pair was allowed to develop heat freely, heat in the test cell is likely to have been dissipated differently in the full test cell. The combination of many electrode pairs in parallel accumulating heat within and the challenges with uncontrolled heat dissipation from the surface of the cell are difficult to replicate in the model in its current set-up. The combination of multiple electrode pairs and through thickness heat accumulation is therefore suggested as a topic of future work.
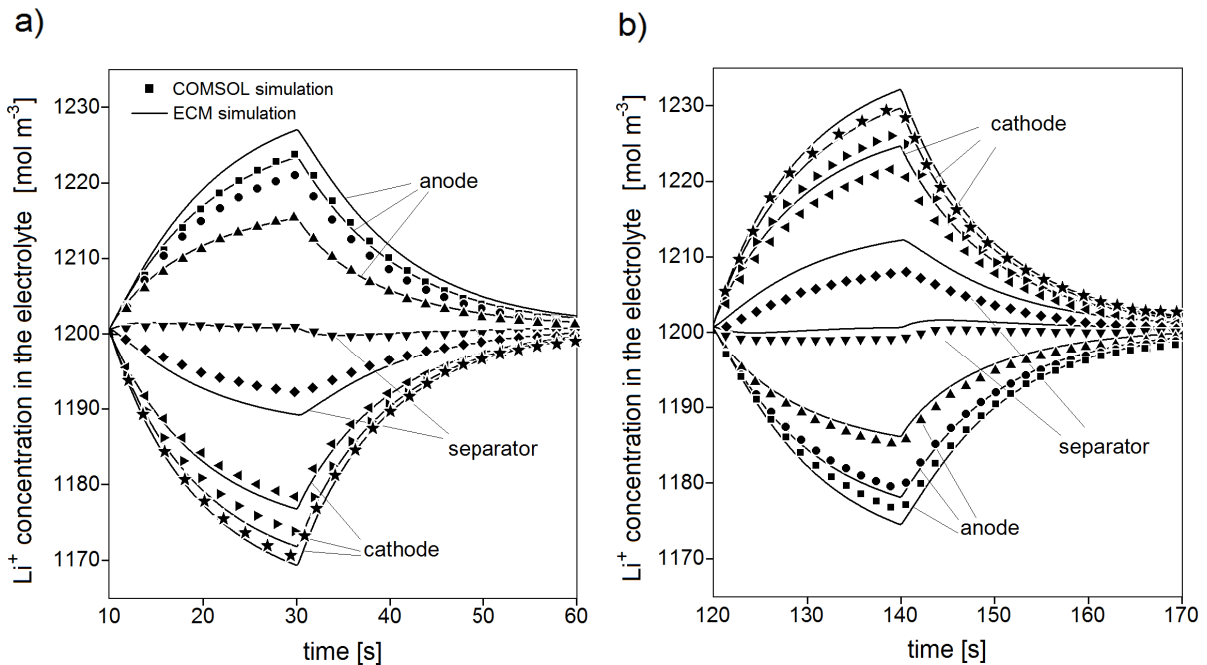
Figure 6.19: Electrolyte concentration during a) the discharge pulse section and b) the charge pulse compared to COMSOL results

Employing the same pulse test (Figure 6.16) and discretisation, lithium-ion concentra-

tion in the electrolyte was investigated and compared to results obtained from COM-SOL; Concentration evolution in this 3-particle/2-separator discretisation configuration is shown Figure 6.19. During the $5\,\mathrm{C}$ discharge pulse lithium concentration deviated by $2.75\,\mathrm{mol\,m^{-3}}$ from the COMSOL prediction, cathode concentration predictions by $2.59\,\mathrm{mol\,m^{-3}}$ and separator by $5.12\,\mathrm{mol\,m^{-3}}$. Similarly during the charge pulse lithium concentration deviations of $3.82\,\mathrm{mol\,m^{-3}}$ (anode), $1.52\,\mathrm{mol\,m^{-3}}$ (cathode) and $6.35\,\mathrm{mol\,m^{-3}}$ (separator) were found. When compared to the initial (equilibrium) conditions of $1200\mathrm{mol\,m^{-3}}$ these are very small, at less than 0.5% error.

6.11 Custom testing procedure

The detailed electrochemical response in terms of overpotentials was investigated in the following by applying the custom testing procedure shown in Figure 6.20a) at 80% SoC and observing the evolution of the various overpotentials at different time steps. The variation of lithium-ion concentration in the electrolyte $c_{\mathrm{Li^+}}$, seen in Figure 6.20b), varies locally for most time steps. Immediately upon load application, concentration gradations can be seen to establish in both the electrolyte and the electrodes. These local concentration gradients balance upon load removal and the cell potentials return to equilibrium.
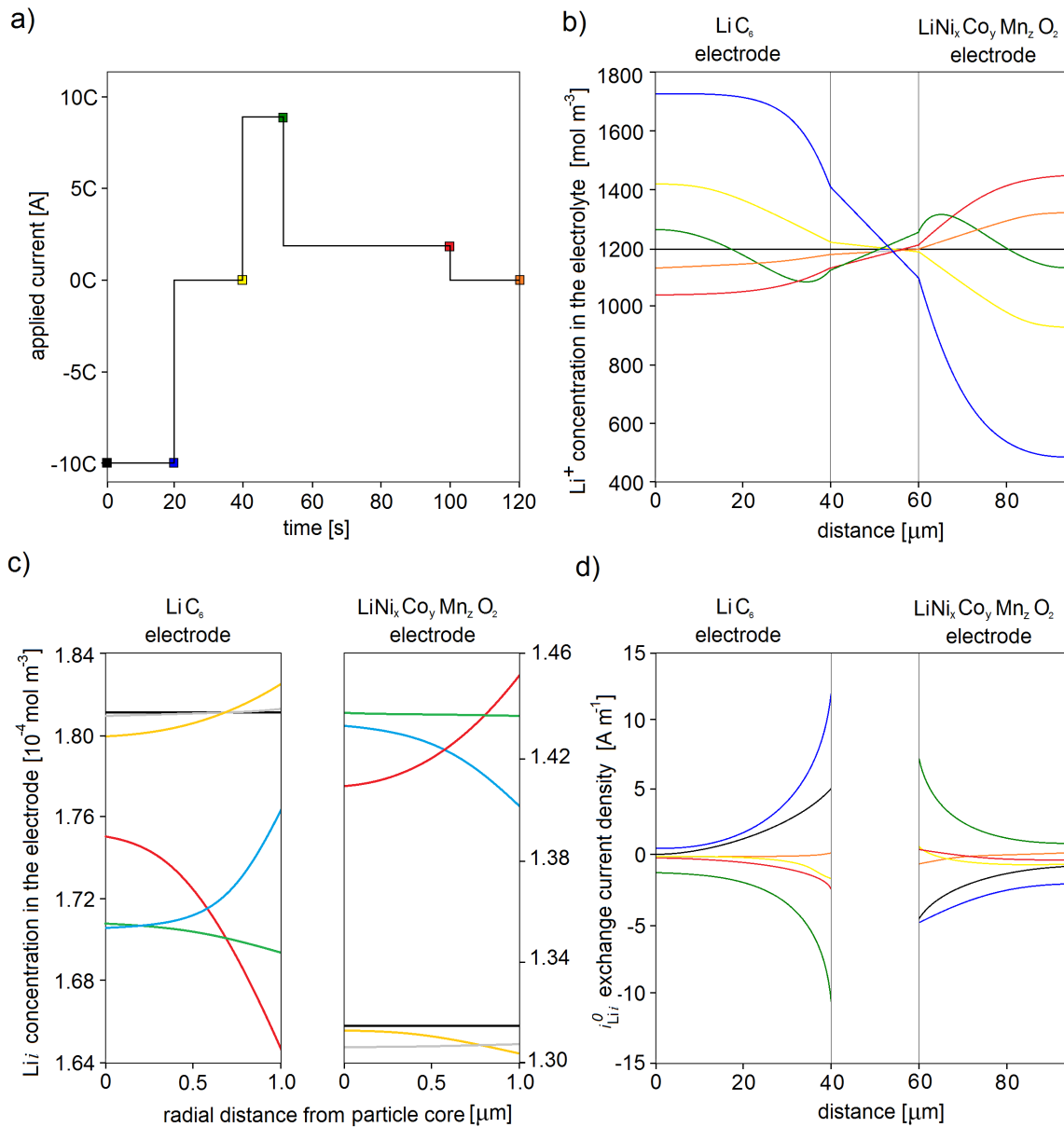
Figure 6.20: Cell voltage response under application of a custom load cycle application at 80% SoC with segregated overpotential contributions showing (a) applied load curve, (b) electrolyte lithium concentration, (c) solid electrode lithium concentration, and (d) exchange current density

In Figure 6.20c) it can be seen that the change in electrode intercalated lithium concentration in the positive electrode is larger than in the negative electrode, indicating a larger diffusion overpotential in the negative electrode. This is not surprising given the smaller solid electrode diffusion coefficient D_s of the anode material. The variation in local current density is shown in Figure 6.20d). It can be seen that variations are particularly extreme during the initial (strongest) discharge period, pointing towards the fact that it is very sensitive to mass transport limitations. This can also be observed in Figure 6.21a) over the same test period, where the contributions of all overpotentials are overlaid. When summing up the potential losses due to the various electrochemical and electric process contributions, and normalising them over the total overpotential during the cycle segment

(Figure 6.21b), the percentage contribution of each phenomenon in each domain can be observed separately in Figure 6.21b).
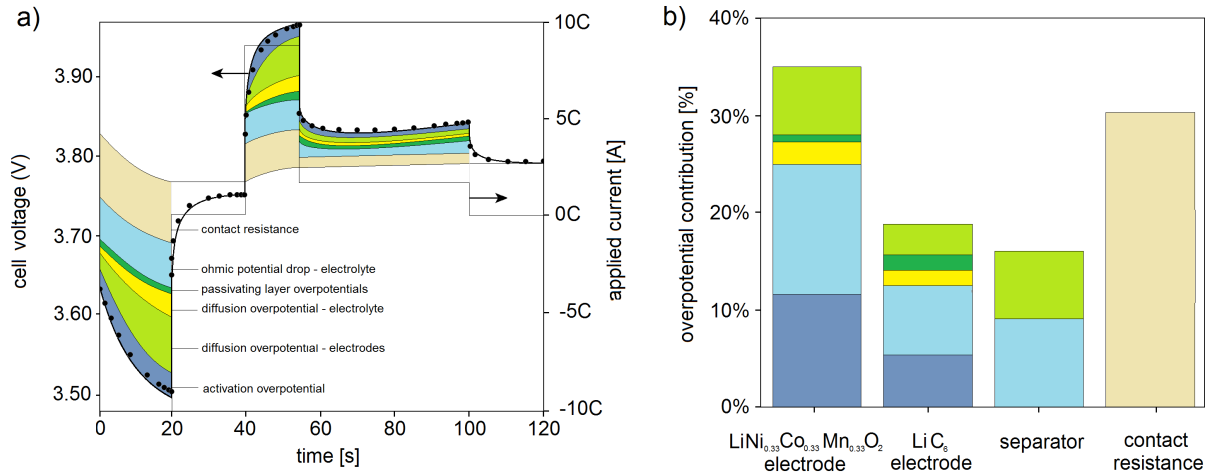
Figure 6.21: a) Comparison of model prediction of cell voltage and contribution overpotentials for the custom load cycle in Figure 6.20a) at 80% SoC model prediction (solid thick), experimental data (symbols), and applied C-rate (solid thin, right axis) b) normalised percentage overpotential contributions in each domain

It can be seen in Figure 6.21b) that the largest contribution to overall overpotential stems from contact resistance and an ohmic potential drop across the electrolyte $\left(\phi^{l}_{\text{LiMO}_2} - \phi^{l}_{\text{LiC}_6}\right)$, while electrolyte and electrode mass diffusion overpotentials, activation and passivating layer overpotentials present a relatively smaller contribution. Overall potential losses in the electrolyte amount to 34% during this cycle, while the remainder of overpotential losses occurs in the electrodes. It can be seen that significantly higher losses occur in the cathode than in the anode, which justifies the scientific interest in improving the properties of cathode materials.

The pulse procedure (Figure 6.16) was applied to the 5 Ah Kokam battery cell at various SoC levels (80%, 65%, 50%, 35% and 20% SoC); with the aim to compare the accuracy of the model predictions for dynamic inputs over the whole range of SoCs. Model predictions and experimental data of this procedure are shown in Figure 6.22.
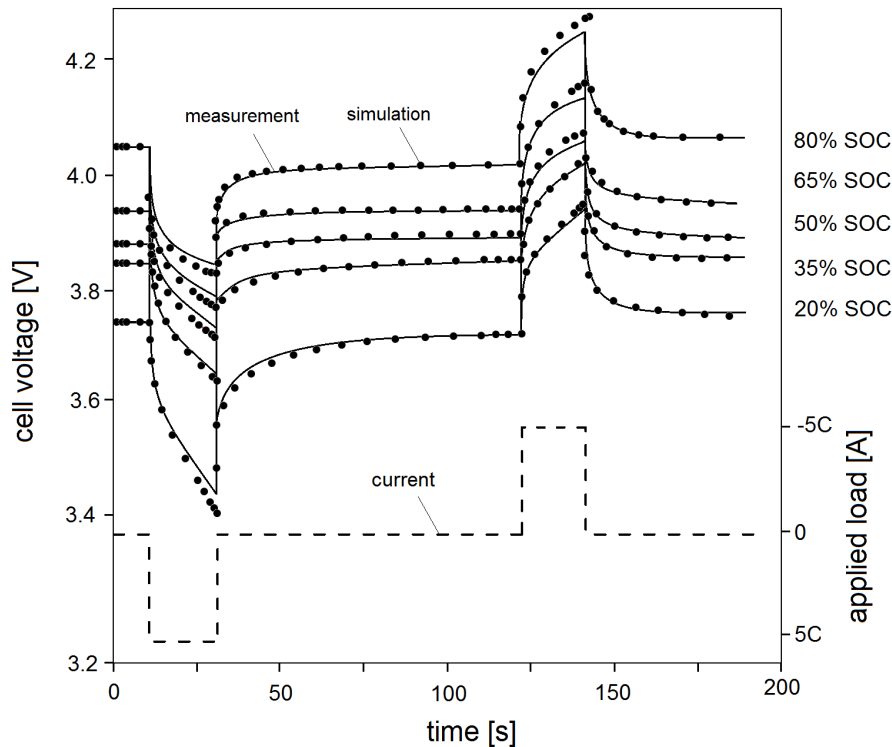
Figure 6.22: Comparison of model prediction and experimental of cell response to a pulse procedure at 20%, 35%, 50%, 65% and 80% SoC. SoC values outside this range were not tested as the cut-off voltages were reached during the charge/discharge pulse periods which terminated the tests

Expectedly, the largest deviations of the model predictions from the experimental data occurred at high SoC and low SoC: a maximum difference of 4.62 mV between the experimental data and the model predictions was found for the highest SoC pulse procedure (80% SoC) and a 11.44 mV difference was found for the lowest SoC pulse procedure (20% SoC). These errors can be attributed to inaccuracies in the values of stoichiometry at 100% SoC and 0% SoC in anode and cathode (Table 6.1). Slight variations of $x_{-,100\%}$, $y_{+,100\%}$, $x_{-,0\%}$, $y_{+,0\%}$, result in significantly different thermodynamic potentials at both extremes of SoC (see Figure 6.4). In principle, the initial values of stoichiometry depend on cycling and storage history of the cell.

To demonstrate the model's capabilities at an increased level of load complexity, a Northern European Driving Cycle (NEDC) load curve was scaled to suit the capacity and voltage range of the Kokam cell; the NEDC was chosen due to its popularity in industry despite being known to fall short in demonstrating the benefits of electrified vehicles. In Figure 6.23 the ECN cell voltage prediction is compared to experimental data. The largest deviation from the experimental data occurred at the higher C-rate event at 1115.1 s (51.5 mV difference, 1.29% error).
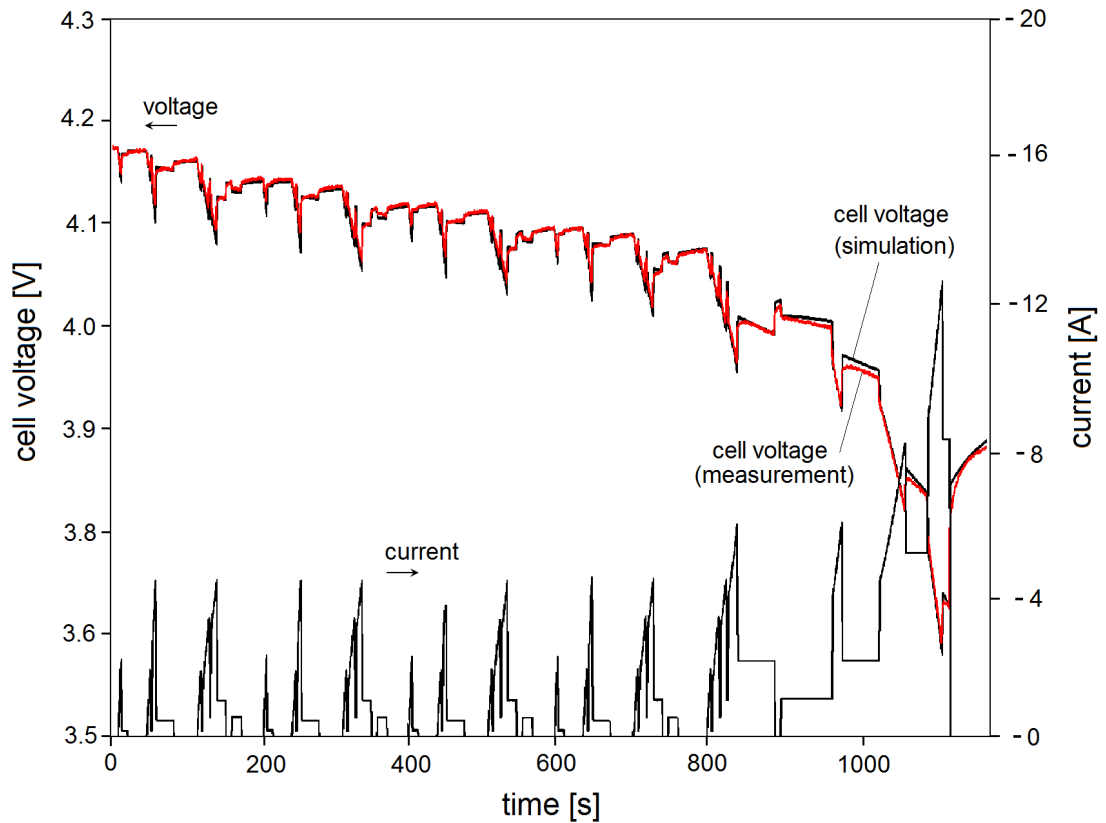
Chapter

Figure 6.23: Comparison of model prediction and experimental data of cell response to an NEDC derived load cycle

6.12 Real-life driving cycle

To demonstrate the model's capabilities in a real-world application, test data (current, voltage, time) was collected from a vehicle participating in the Future Car Challenge in 2012 [199]. Of this, a 25 min (Figure 6.24a) extract was used as input to the model and the results compared to the cell voltage recordings made during the run. The vehicle in this case was a PHEV with relatively low C-rates. The cell measurements ($\square$) were recorded from the BMS via the vehicle CAN bus at discrete time steps (0.1 s) with an associated allowable error ($|$) in Figure 6.24. This 'allowable error' stems from rounding of the delivered sensor measurements as the CAN communicates values rounded to four significant digits. The load to the battery was obtained via the CAN as well, such that the ability of the ECN in replacing the implemented simplistic battery state prediction algorithm could be demonstrated. Not only does the model inform of basic performance parameters (such as Voltage, SoC, SoF) but it does so by enabling access to a wealth of additional information which are all derived from the underlying electrochemical principles.
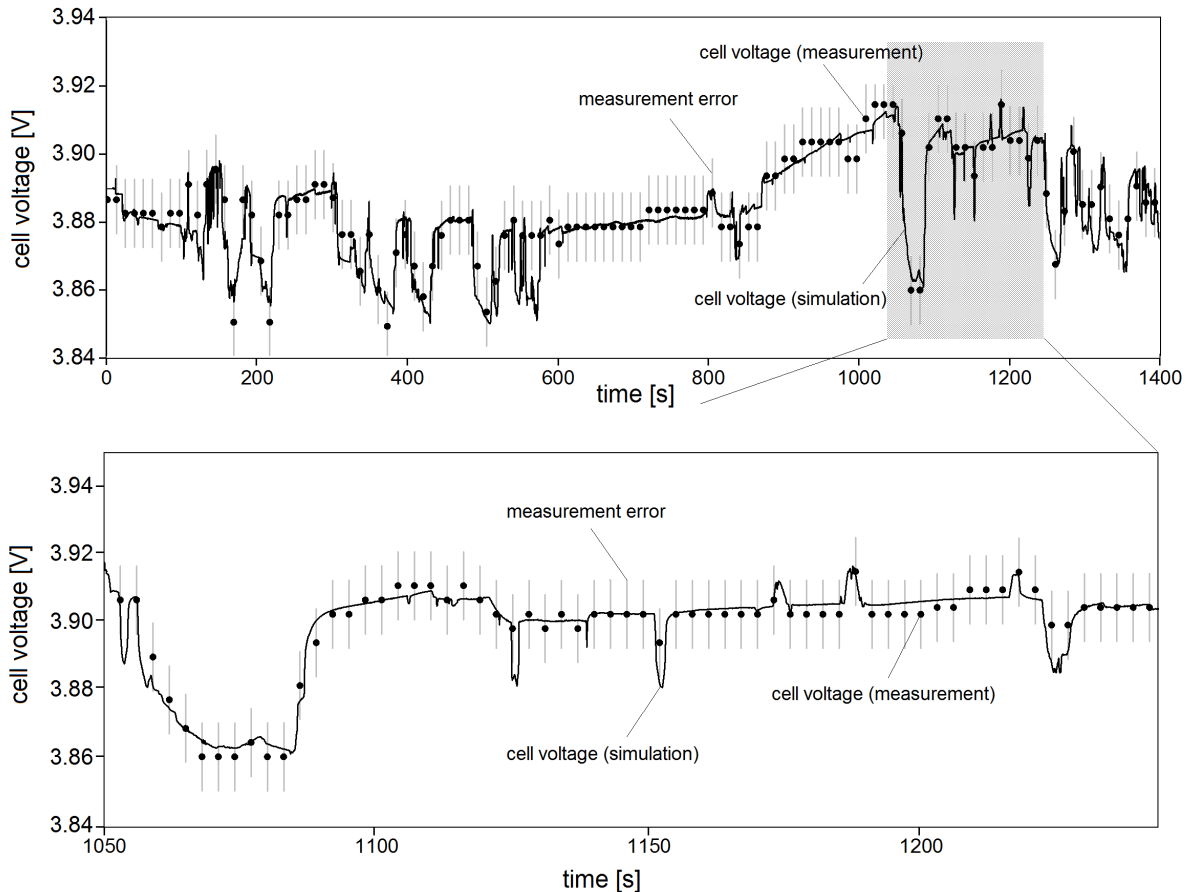
Figure 6.24: (top) Real drive cycle application to the ECN simulation in comparison with experimental data. (bottom) 200 s extract of the same load cycle

The cell in the vehicle is, of course, integrated in a pack and likely subject to unequal loading and cell balancing, while only the current/voltage at the pack connectors is conventionally measured for range estimation. Knowledge of the pack configuration allowed scaling of load and cell response to a single cell; however, hidden is information about cell imbalances, internal resistance variations and individual cell load balancing by the BMS. Assuming these are not dominant effects in the brand-new battery pack of the test vehicle under investigation, the error between test data and ECN results is attributed mostly to wire shielding (leading to errors in current/voltage recordings of the test data) and temperature impact, possibly from neighbouring cells (leading to errors in simulation results). The errors (average 2.35% - 91.65 mV) were found to be worst during the most aggressive 5% of discharge events (in terms of C-rate) whilst all remaining events were found to deviate by less than 0.12% from the collected data. Run-time of the simulation was 42.57 s for the whole 25 min load-cycle using the samronyme computation power available as previously mentioned.

6.13   Interim conclusion

The novel phenomenological electrical circuit network presented has been demonstrated to predict electrochemical systems under realistic operational conditions. It allows the

calculation of species concentration distribution for a given current load as a result of electrochemical reactions and species diffusion. It has been demonstrated that all variables have a direct physical interpretation and that there is direct access to all states of the cell via the model variables (species concentrations, potentials etc.).

This application example is an automotive system, in which results were obtained at a rate faster than real-time and within the accuracy requirements of the Battery Management System. Examples for model output were given for a constant and pulsed charge/discharge, as well as a standard and a realistic drive cycle load; all of which were shown do be in good agreement with test data and complex simulation software output.

Conclusion

The aim of this work was to develop a new phenomenological battery model able to capture the electrochemical and physical processes relevant in automotive applications under realistic operational conditions. The model was obtained by combining detailed knowledge of cell electrochemistry with the principles of electrical engineering. The mathematical equations describing the complex phenomena occurring during electrochemical reactions have been translated into electric circuit elements. The model has been demonstrated to serve as a purposive performance prediction tool for gaining insight into the electrochemical processes occurring during vehicle operation. It has been structured in order to allow for straightforward incorporation of further physical and electrochemical processes. Various examples of model predictions were given for constant and pulsed charge/discharge loads, as well as standard and real-world drive cycle loads; all of them were shown do be in good agreement with experimental data or commercial modelling software predictions. It has been shown that physical phenomena, electrochemical and electrical quantities are straightforward to monitor since the physical meaning of each circuit element in the model is apparent.

The model presented addresses the majority of aspects previously identified as areas of further development in the academic literature

1. In the presented methodology the model is structured into clearly defined physics-based sub-circuits governing individual species' transport. Each can be observed separately and their characteristic parameter evolution compared to other model predictions or, where possible, to experimental data

2. An electrical analogy is derived governing the electrochemical reaction process which links the sub-systems of the three species. The methodology allows for a straightforward comparison of electrochemical parameters (such as charge transfer and series) to experimental electrochemical impedance spectroscopy data. The newly presented phenomenological Equivalent Circuit Network allows for locally variable

   (a) lithium-ion and lithium-atom concentrations,

   (b) exchange current densities,

   (c) overpotentials due to reaction activation, diffusion of lithium-ions and intercalated lithium, passivating layers and double layers,

   (d) passivating layer thickness, resistance and capacitance,

   (e) double layer capacitance and overpotential, and

    (f) local temperature and the subsequent dependency of local electrochemical processes.

3. The Triple Species Element encapsulates the process of the electrochemical reaction and, as such, serves as the link between the electric and the chemical domains, connecting the three separate transport circuits of electrons, the reduced species (intercalated lithium) and the oxidized species (lithium-ions) in the electrodes and electrolyte.

4. Previous modelling efforts by Bergveld [4] have been extended to include the following degradation phenomena of

    (a) capacity fade through loss of cyclable lithium due to passivating layer growth, and

    (b) power fade through increase of internal impedance due to passivating layer growth.

5. A clear visual representation and layout of the network is developed, governing the electrochemical phenomena and transport of species. This allows for straightforward future adaptations, extensions and system-level implementations by system designers of the present framework.

In comparison to previous ECN modelling efforts presented in the literature, the presented phenomenological equivalent circuit network allows the extraction of a wealth of additional information on internal battery performance characteristics (e.g. concentrations, potentials, overpotentials, local temperatures etc.), enabling a more accurate real-time prediction of the states of the battery. Given the same measurement inputs as conventional 'black-box' models implemented in commercial vehicles today, this information allows the quantification of battery performance parameters (such as local heat generation and capacity/power fade), which have so far been inaccessible.

Although cast in a framework familiar to control engineers, the model benefits from many of the advantages of electrochemical battery models: all variables have a direct physical interpretation and there is direct access to all states of the cell via the model variables. As such, the model predicts performance for all combinations of operational conditions, takes account of their interplay and can track the causes of degradation without lengthy experimental testing.

Knowledge of the battery states ultimately allows the derivation of a compact battery performance estimator including the observation of internal processes for direct BMS implementation. The visibility of detailed variables allows for optimised cell control and safeguarding of the battery pack, while enabling a more accurate prediction of the onset of capacity and power fade.

The methodology is further applicable for electrochemical system performance evaluation and prediction in any kind of portable electronic device or application with limited computational power availability and fast solution requirements. Effects such as battery degradation can be predicted based on physical phenomena, rather than by empirical relations.

The proposed model therefore allows a significant enhancement of BMS capabilities while avoiding costly hardware modifications or experimental tests. This will not only enable designers to better estimate the lifetime of the product as a whole for warranty purposes, but will also render electric vehicles a compelling alternative to internal combustion engine propelled vehicles.

Future work

Within the time constraints of this PhD project, the author feels that a significant contribution has been made but acknowledges many areas of the modelling and experimental work could have benefited from more work given more time. The following suggested model extensions and future work recommendations are by no means exhaustive but aim to indicate a direction of research towards 1. the scaling of the presented model, 2. the accounting for additional operating conditions in automotive applications, 3. the modification to different cell chemistries and 4. the adaptation of the model code for BMS implementation. Furthermore, 5. model usage purposes and 6. model applications besides automotive battery state prediction are suggested.

1. Scaling of the presented model:

    (a) addition of multiple electrode pairs to build a multi-layered structure reflecting commercial cells

    (b) addition of a second and third discretised dimension to predict cell behaviour in 2D and 3D

    (c) modification of the electrode discretisation to allow for more realistic particle dispersions

    (d) modification of the electrode phase circuit equations to account for different particle shapes

    (e) addition of multiple cells to form cell assemblies and battery packs

    (f) addition of a thermal model accounting for heat propagation through the cell thickness and across cell assemblies

2. Battery electrochemistry modification:

    (a) modification of the parameter set accounting for different chemistries governed by the same electrochemical reaction laws

    (b) modification of the triple species element to allow for different electrochemical reaction laws

    (c) modification of the double layer model to account for different layer structures and electrode porosity

(d) extension to allow for further degradation mechanisms, such as lithium plating, passivating layer break down, dendrite formation etc.

(e) extension to allow for gas development during the reaction process

(f) extension to account for phase transition phenomena of the insertion electrode materials

(g) extension to account for self-discharge

(h) extension to account for material corrosion

(i) modification to enable a the calculation of electrode equilibrium potentials from fundamental principles

(j) extension to account for anions occurring as part of the reaction process

(k) extension to account for lithiation and de-lithiation stresses and tortuosity of electrodes

(l) extension to account for thermal run-away and uncontrolled reaction processes

3. Extension of operating conditions envelope:

   (a) extension of the thermal model accounting for external temperature variations (cell tab temperature control, surface temperature control, adverse operating temperature etc.)

   (b) extension to account for the effects of mechanical abuse (vibration, compression, nail penetration etc.)

   (c) extension for further modes of degradation (dendrites, passivating layer breakdown, electrode de-lamination, electrolyte decomposition etc.)

4. Adaptation of the model code for BMS implementation:

   (a) code transformation to fit BMS code

   (b) sensitivity study under automotive operational conditions to potentially fix certain parameters and subsequently reduce model complexity

   (c) assessment of in-use computational requirements of the optimised on-line code

5. Model usage purposes:

   (a) cell design

   (b) pack design

   (c) cooling system design

   (d) Battery Management System design

   (e) Energy Storage System design and optimisation of electric energy use in the powertrain

   (f) charging/discharging strategy development

6. Further model applications beyond batteries in automotive systems:

   (a) state prediction in small portable electronics systems

(b) state prediction in energy grid balancing and decentralised energy storage systems

(c) other electrochemical systems characterised by reactions of species at a reaction site (fuel cells, redox flow batteries)

Appendix

Derivation of apparent equilibrium potential $E_i^{\text{eq}*}$:

$$
\begin{aligned}
E_i^{\text{eq}*} \;=\;& E_i^0 + \frac{RT}{nF}\left[\ln\left(\frac{a_i^{\text{s}}}{a_{\text{Lii}}^{\text{s}}}\right) - U_i x_i + \zeta_i\right] + \frac{RT}{nF}\ln\left(\frac{a_{\text{Li}+}^{\text{s}}}{a_{\text{Li}+}^{\text{eq}}}\right) \\[2ex]
=\;& E_i^0 + \frac{RT}{nF}\left[\ln\left(\frac{a_i^{\text{s}} a_i^{\text{b}} a_{\text{Lii}}^{\text{b}}}{a_{\text{Lii}}^{\text{s}} a_i^{\text{b}} a_{\text{Lii}}^{\text{b}}}\right) - U_i x_i + \zeta_i\right] + \frac{RT}{nF}\ln\left(\frac{a_{\text{Li}+}^{\text{s}}}{a_{\text{Li}+}^{\text{eq}}}\right) \\[2ex]
=\;& E_i^0 + \frac{RT}{nF}\left[\ln\left(\frac{a_i^{\text{b}}}{a_{\text{Lii}}^{\text{b}}}\right) - U_i x_i + \zeta_i\right] + \frac{RT}{nF}\ln\left(\frac{a_i^{\text{s}} a_{\text{Lii}}^{\text{b}}}{a_{\text{Lii}}^{\text{s}} a_i^{\text{b}}}\right) + \frac{RT}{nF}\ln\left(\frac{a_{\text{Li}+}^{\text{s}}}{a_{\text{Li}+}^{\text{eq}}}\right) \\[2ex]
=\;& E_i^0 + \frac{RT}{nF}\left[\ln\left(\frac{1-x_{\text{Lii}}}{x_{\text{Lii}}}\right) - U_i x_i + \zeta_i\right] + \frac{RT}{nF}\ln\left(\frac{a_i^{\text{s}} a_{\text{Lii}}^{\text{b}}}{a_{\text{Lii}}^{\text{s}} a_i^{\text{b}}}\right) + \frac{RT}{nF}\ln\left(\frac{a_{\text{Li}+}^{\text{s}}}{a_{\text{Li}+}^{\text{eq}}}\right) \\[2ex]
=\;& E_i^{\text{eq}} + \frac{RT}{nF}\ln\left(\frac{a_i^{\text{s}} a_{\text{Lii}}^{\text{b}}}{a_{\text{Lii}}^{\text{s}} a_i^{\text{b}}}\right) + \frac{RT}{nF}\ln\left(\frac{a_{\text{Li}+}^{\text{s}}}{a_{\text{Li}+}^{\text{eq}}}\right) \\[2ex]
=\;& E_i^{\text{eq}} + \eta_{\text{Lii}}^{\text{d}} + \frac{RT}{nF}\ln\left(\frac{a_{\text{Li}+}^{\text{s}}}{a_{\text{Li}+}^{\text{eq}}}\right) \\[2ex]
=\;& E_i^{\text{eq}} + \eta_{\text{Lii}}^{\text{d}} + \eta_{\text{Li}+}^{\text{d}}
\end{aligned}
\tag{6.1}
$$

Tables 6.2 - 6.3 summarise the assessment of the most advanced phenomenological equivalent circuit models proposed in the literature against the design criteria and highlights areas of possible further developments.

Task: Translation of the relevant electrochemical phenomena into electric modelling analogy in the form of an equivalent circuit model over length and time scales relevant to automotive applications which capture the necessary physics phenomena of interest

Model design criteria	Have or have not been demonstrated by the most advanced phenomenological equivalent circuit models	Identified knowledge gap to be addressed in this work
· Each circuit element is to retain a physical meaning · Distinct circuit sections are to be associated with physical phenomena of individual chemical species · Individual domains and local phenomena are to be distinguishable · Variables are to be observable for later implementation of control algorithms; creation of a transparent model · Model extensions are to be easily added	has been demonstrated, although not all physics phenomena relevant to local heat generation and degradation have been included thus far, the separation between the circuits is not intuitive, and the process of extending the model to include those omitted phenomena is unclear	· extend previous work by proposing circuit elements for thus far omitted phenomena · capacity fade, power fade, local heat generation · structure the system in the form of separate sub circuits · include local heat generation · allow for easy model extensions
Prediction on the basis of on-board available live variables I_{bat}, V_{bat}, T (i.e no hardware modifications)	has been demonstrated to a limited extent, although the thermal dependencies have not been sufficiently demonstrated	demonstrate clearly the model dependency on the on-board available live variables
Development of a visual implementation allowing easy parametrisation/adaptation to different cell dimensions	has been demonstrated, although the visual distinction between different processes and species circuits could be clearer and a procedure of extending the model to account for missing phenomena could be provided	**improve on previous work in terms of visual representation/layout of the network and ability to extend to aid future adaptation/modifications and system-level implementation by system engineers**
Parametrisation through an external script with an easily modifiable parameter list	parametrisation and model extension procedure has not been reported	adopt a parametrisation through an external script with an easily modifiable parameter list to aid future adaptation/modifications and system-level implementation by system engineers
Prediction of the same phenomena as standard equivalent circuit models	has been demonstrated	-

Table 6.2: Literature assessment against model design criteria I

Task: Prediction of additional phenomena by developing a physics based electric equivalent circuit of the electrochemistry governing equations describing the processes in the battery:

Model design criteria	Have or have not been demonstrated by the most advanced phenomenological equivalent circuit models	Identified knowledge gap to be addressed in this work
· Passivating layer growth, with variable layer resistance and capacitance allowing for the prediction of loss of active cyclable material and capacity fade	· has been demonstrated by advanced phenomenological Equivalent Circuit Models	· **include passivating layer growth, with variable layer resistance and capacitance allowing for the prediction of loss of active cyclable material and capacity fade**
· Variable electrochemical double layer capacitance and potential dependency on local electrochemical and thermal conditions	· only demonstrated as constant capacitance, irrespective of local electrochemical and thermal conditions	· **allow for locally variable double layer capacitance and potential, depending on local electrochemistry and temperature**
· Variable charge-transfer resistance	· yes, but not locally temperature dependent	· allow for local temperature dependency
· Variable exchange current density as a function of local concentrations gradients	· yes, but not locally temperature dependent	· allow for local temperature dependency
· Local cell characteristics to be coupled to local temperature	· no	· **allow for local temperature variation and the subsequent dependency of local electrochemical processes**
· Electric potential of chemical species to be derived on the basis of Nernst equations and standard redox potentials, rather than empirical functions	· no, an intermediate method has been demonstrated, still representing a semi-empirical approach	· evaluate species electric potential from fundamental principles rather than adopting an empirical/semi-empirical approach
· Diffusion limitations to mass transport	· yes to some extent, mass transport limitations in the double layer have not been considered	· evaluate diffusion limitations of the species within their respective sub-circuits as well as in the double layer
· Activation overpotential for electrochemical reactions to take place	· has been demonstrated	-
Spatial discretisation to allow the distinction between local effects occurring at anode, cathode and separator	yes, but only under the assumption of homogeneous temperature profiles	allow for a full discretisation thermally as well as electrochemically
Demonstration of the model capabilities in predicting battery performance under typical automotive characteristic operating conditions	has been demonstrated to the extent of the respective model's abilities, where heat generation predictions and locally occurring electrochemical phenomena have to be taken with caution due to simplifications	demonstrate the models' capability in prediction of local phenomena as well as overall performance characteristics

Table 6.3: Literature assessment against model design criteria II

Bibliography

[1] K. C. Kinson and M. M. Doeff. Electrode Materials for Lithium Ion Batteries. *Material Matters*, 7(4), 2012.

[2] S. Brown. *Diagnosis of the Lifetime Performance Degradation of Lithium-Ion Batteries*. Doctoral thesis, Kungliga Tekniska Högskolan, Stockholm, 2008.

[3] M. Winter and R. J. Brodd. What Are Batteries, Fuel Cells, and Supercapacitors? *Chemical Reviews*, 104(10):4245–4270, October 2004.

[4] H. J. Bergveld. *Battery Management Systems Design by Modelling*. Doctoral thesis, University of Eindhoven, 2001.

[5] O. Tremblay, L. A. Dessaint, and A. I. Dekkiche. A Generic Battery Model for the Dynamic Simulation of Hybrid Electric Vehicles. In *2007 IEEE Vehicle Power and Propulsion Conference*, pages 284–289. IEEE, September 2007.

[6] W. Waag and D. U. Sauer. Adaptive Estimation of the Electromotive Force of the Lithium-Ion Battery after Current Interruption for an Accurate State-of-Charge and Capacity Determination. *Applied Energy*, 111:416–427, November 2013.

[7] K. A. Smith, C. D. Rahn, and C. Y. Wang. Model-Based Electrochemical Estimation of Lithium-Ion Batteries. In *2008 IEEE International Conference on Control Applications*, pages 714–719. IEEE, 2008.

[8] Y. Merla. *Segmented Fuel Cell-Battery Passive Hybrid Systems*. Year 4 individual project report, Imperial College London, 2013.

[9] I. Hunt and G. Offer. The Effect of Different Cooling Methods on Degradation of Lithium-Ion Batteries - in progress. 2015.

[10] C. Julien, A. Mauger, K. Zaghib, and H. Groult. Comparative Issues of Cathode Materials for Li-Ion Batteries. *Inorganics*, 2(1):132–154, March 2014.

[11] Robert Bosch GmbH. CAN Specification. 1991.

[12] Robert Bosch GmbH. *Bosch Autoelektrik und Autoelektronik*. Vieweg + Teubner, 2011.

[13] L. Leggett. Geneva Motor Show: Electric Cars No Longer the Exception?, March 2014.

[14] O. Bitsche and G. Gutmann. Systems for Hybrid Cars. *Journal of Power Sources*, 127(1-2):8–15, March 2004.

[15] R. F. Nelson. Power Requirements for Batteries in Hybrid Electric Vehicles. *Journal of Power Sources*, 91(1):2–26, November 2000.

[16] MarkLines Co. Branchenportal MarkLines 2015 - Automotive Industrial Portal, 2015.

[17] M. Anderman. *Assessing the Future of Hybrid and Electric Vehicles: The xEV Industry Insider Report*. Oregon House, California, US, 2014 edition, 2014.

[18] C. Pillot. The worldwide battery market 2012-2025. Technical report, Avicenne Energy, Nice, France, 2013.

[19] McKinsey & Co. A Portfolio of Power-trains for Europe: a Fact-based Analysis. Technical report, McKinsey & Co, 2012.

[20] Toyota Motors Corporation. Toyota Motors Corporation - Annual Report, 2014.

[21] H. D. Poetsch. Volkswagen - Driving Forward. Technical report, Volkswagen GmbH, Frankfurt, 2011.

[22] K. Hall. How 3D Printing Impacts Manufacturing, 2013.

[23] D. Keeble. The Culture of Planned Obsolescence in Technology Companies. Technical report, Oulu University of Applied Sciences, Oulu, 2013.

[24] A. D. Jr. Chandler. *Strategy and Structure: Chapters in the History of the American Industrial Enterprise*. MIT press, Cambridge, MA, 1962.

[25] E. Musk. All Our Patents Belong To You - Tesla Motors, 2014.

[26] M. Rutherford. Electric Cars: The Truth about the Cost and Range, 2012.

[27] Ricardo Plc. dSPACE - Ricardo Magazine. Technical report, dSPACE GmbH, Paderbon, Germany, 2010.

[28] Element Energy Ltd. Influences on the Low Carbon Market from 2020-2030. Technical report, Element Energy ltd., Cambridge, UK, 2011.

[29] BCG. Focus - Batteries for Electric Cars. Technical report, 2010.

[30] The Freedonia Group. World Batteries to 2016 - Demand and Sales Forecasts, Market Share, Market Size, Market Leaders. Technical report, Cleveland, OH, 2012.

[31] A. Peseran and T. Markel. Battery Requirements for Plug-In Hybrid Electric Vehicles - Analysis and Rationale. In *International Electric Vehicle Symposium (EVS-23)*, page 17, Anaheim, California, 2007. National Renewable Energy Laboratory.

[32] P. W. C. Northrop, B. Suthar, V. Ramadesigan, S. Santhanagopalan, R. D. Braatz, and V. R. Subramanian. Efficient Simulation and Reformulation of Lithium-Ion Battery Models for Enabling Electric Transportation. *Journal of the Electrochemical Society*, 161(8):E3149–E3157, May 2014.

[33] B. Scrosati. History of Lithium Batteries. *Journal of Solid State Electrochemistry*, 15(7-8):1623–1630, May 2011.

[34] N. Kipnis. Luigi Galvani and the Debate on Animal Electricity, 1791-1800. *Annals of Science*, 44(2):107–142, March 1987.

[35] M. Pera and J. Mandelbaum. *The Ambiguous Frog: The Galvani-Volta Controversy on Animal Electricity*. Princeton University Press, 2014.

[36] R. M. Dell and D. A. J. Rand. *Understanding Batteries*. Royal Society of Chemistry, Cambridge, 2001.

[37] K. Fisher, E. Wallén, P. P. Lieren, and M. Collins. Battery Waste Management Life Cycle Assessment. Technical report, Environmental Resources Management, 2006.

[38] G. Hollister-Short. *History of Technology*. A&C Black, 20 edition, 1999.

[39] W. Grove. On Voltaic Series and the Combination of Gases by Platinum. *Philosophical Magazine Series 3*, (24), 1839.

[40] A. K. Hjelm, T. Eriksson, and G. Lindbergh. Electrochemical Investigation of LiMn2O4 Cathodes in Gel Electrolyte at Various Temperatures. *Electrochimica Acta*, 48(2):171–179, November 2002.

[41] A. Nytén. *Low-Cost Iron-Based Cathode Materials for Large-Scale Battery Applications*. Doctoral thesis, Uppsala University, 2006.

[42] K. K. Lee, W. S. Yoon, K. B. Kim, K. Y. Lee, and S. T. Hong. Characterization of LiNi0.85Co0.10M0.05O2 (M = Al, Fe) as a Cathode Material for Lithium Secondary Batteries. *Journal of Power Sources*, 97-98:308–312, July 2001.

[43] H. Yang and J. Prakash. Determination of the Reversible and Irreversible Heats of a LiNi0.8Co0.15Al0.05O 2/Natural Graphite Cell Using Electrochemical-Calorimetric Technique. *Journal of The Electrochemical Society*, 151(8):A1222, August 2004.

[44] D. P. Abraham, E. M. Reynolds, E. Sammann, A. N. Jansen, and D. W. Dees. Aging Characteristics of High-Power Lithium-Ion cells with LiNi0.8Co0.15Al0.05O2 and Li4/3Ti5/3O4 Electrodes. *Electrochimica Acta*, 51(3):502–510, October 2005.

[45] W. A. van Schalkwijk and B. Scrosati. *Advances in Lithium-Ion Batteries*. Springer US, Boston, MA, 2002.

[46] D. Belov and M. Yang. Failure Mechanism of Li-ion Battery at Overcharge Conditions. *Journal of Solid State Electrochemistry*, 12(7-8):885–894, 2008.

[47] J. W. Fergus. Recent Developments in Cathode Materials for Lithium Ion Batteries. *Journal of Power Sources*, 195(4):939–954, February 2010.

[48] K. Kang, Y. S. Meng, J. Bréger, C. Grey, and G. Ceder. Electrodes with High Power and High Capacity for Rechargeable Lithium Batteries. *Science*, 311(5763):977–80, February 2006.

[49] G. G. Amatucci. Cobalt Dissolution in LiCoO2-based Non-aqueous Rechargeable Batteries. *Solid State Ionics*, 83(1-2):167–173, January 1996.

[50] G. G. Amatucci. CoO2 - The End Member of the LixCoO2 Solid Solution. *Journal of The Electrochemical Society*, 143(3):1114, March 1996.

[51] I. Belharouak, W. Lu, D. Vissers, and K. Amine. Safety Characteristics of LiNi0.8Co0.15Al0.05O2 and LiNi1/3Co1/3Mn1/3O2. *Electrochemistry Communications*, 8(2):329–335, 2006.

[52] D. Belov and M. Yang. Investigation of the Kinetic Mechanism in Overcharge Process for Li-ion Battery. *Solid State Ionics*, 179(27):1816–1821, 2008.

[53] C. H. Doh, D. H. Kim, H. S. Kim, H. M. Shin, Y. D. Jeong, S. I. Moon, B. S. Jin, S. W. Eom, K. W. Kim, D. H. Oh, and A. Veluchamy. Thermal and Electrochemical Behaviour of C/LixCoO2 Cell During Safety Test. *Journal of Power Sources*, 175(2):881–885, January 2008.

[54] Y. Takahashi, S. Tode, A. Kinoshita, H. Fujimoto, I. Nakane, and S. Fujitani. Development of Lithium-Ion Batteries with a LiCoO2 Cathode Toward High Capacity by Elevating Charging Potential. *Journal of The Electrochemical Society*, 155(7):A537, July 2008.

[55] H. Liu, Y. Yang, and J. Zhang. Reaction Mechanism and Kinetics of Lithium Ion Battery Cathode Material LiNiO2 with CO2. *Journal of Power Sources*, 173(1):556–561, November 2007.

[56] D. P. Abraham, R. D. Twesten, M. Balasubramanian, I. Petrov, J. McBreen, and K. Amine. Surface Changes on LiNi0.8Co0.2O2 Particles During Testing of High-Power Lithium-Ion Cells. *Electrochemistry Communications*, 4(8):620–625, August 2002.

[57] A. K. Padhi. Phospho-Olivines as Positive-Electrode Materials for Rechargeable Lithium Batteries. *Journal of The Electrochemical Society*, 144(4):1188, April 1997.

[58] S. P. Ong. *First Principles Design and Investigation of Lithium-Ion Battery Cathodes and Electrolytes*. Phd thesis, Massachusetts Institute of Technology, 2011.

[59] M. Wakihara. Recent Developments in Lithium-Ion Batteries. *Materials Science and Engineering: Reports*, 33(4):109–134, June 2001.

[60] Z. Chen, I. Belharouak, Y.K. Sun, and K. Amine. Titanium-Based Anode Materials for Safe Lithium-Ion Batteries. *Advanced Functional Materials*, 23(8):959–969, February 2013.

[61] A. H. Whitehead and M. Schreiber. Current Collectors for Positive Electrodes of Lithium-Based Batteries. *Journal of The Electrochemical Society*, 152(11):A2105, November 2005.

[62] UK National Standards Body (NSB). Secondary Cells and Batteries Containing Alkaline or Other Non-Acid Electrolytes. Secondary Lithium Cells and Batteries for Portable Applications, 2011.

[63] V. Srinivasan, D. Hafemeister, B. Levi, M. Levine, and P. Schwartz. Batteries for Vehicular Applications. In *AIP Conference Proceedings*, volume 1044, pages 283–296, Berkley, September 2008. AIP.

[64] C. Samaras and K. Meisterling. Life Cycle Assessment of Greenhouse Gas Emissions from Plug-in Hybrid Vehicles: Implications for Policy. *Environmental Science & Technology*, 42(9):3170–3176, May 2008.

[65] C. N. Shiau, S. B. Peterson, and J. J. Michalek. Optimal Plug-In Hybrid Vehicle Design and Allocation for Minimum Life Cycle Cost, Petroleum Consumption and Greenhouse Gas Emissions. In *Volume 4: 12th International Conference on Advanced Vehicle and Tire Technologies; 4th International Conference on Micro- and Nanosystems*, pages 183–195. ASME, January 2010.

[66] David Sandalow. Plug-in electric vehicles what role for Washington?, 2009.

[67] Ching-Shin Norman Shiau, Constantine Samaras, Richard Hauffe, and Jeremy J. Michalek. Impact of battery weight and charging patterns on the economic and environmental benefits of plug-in hybrid vehicles. *Energy Policy*, 37(7):2653–2663, July 2009.

[68] J. Neubauer and A. Pesaran. The Ability of Battery Second Use Strategies to Impact Plug-in Electric Vehicle Prices and Serve Utility Energy Storage Applications. *Journal of Power Sources*, 196(23):10351–10358, December 2011.

[69] J. Neubauer, A. Brooker, and E. Wood. Sensitivity of Battery Electric Vehicle Economics to Drive Patterns, Vehicle Range, and Charge Strategies. *Journal of Power Sources*, 209:269–277, July 2012.

[70] J. Neubauer, A. Brooker, and E. Wood. Sensitivity of Plug-in Hybrid Electric Vehicle Economics to Drive Patterns, Electric Range, Energy Management, and Charge Strategies. *Journal of Power Sources*, 236:357–364, August 2013.

[71] A. Sakti, J. J. Michalek, E. R. Fuchs, and J. F. Whitacre. A Techno-Economic Analysis and Optimization of Li-ion Batteries for Light-Duty Passenger Vehicle Electrification. *Journal of Power Sources*, 273:966–980, January 2015.

[72] P. Albertus, J. Couts, V. Srinivasan, and J. Newman. A Combined Model for Determining Capacity Usage and Battery Size for Hybrid and Plug-in Hybrid Electric Vehicles. *Journal of Power Sources*, 183(2):771–782, September 2008.

[73] A. J. Bard and L. R. Faulkner. *Electrochemical Methods - Fundamentals and Applications*. Wiley & Sons, New York, New York, USA, 2 edition, 2001.

[74] K. Tasaki. Solvent Decompositions and Physical Properties of Decomposition Compounds in Li-Ion Battery Electrolytes Studied by DFT Calculations and Molecular Dynamics Simulations. *The journal of physical chemistry. B*, 109(7):2920–33, February 2005.

[75] J. Christensen and J. Newman. Cyclable Lithium and Capacity Loss in Li-Ion Cells. *Journal of The Electrochemical Society*, 152(4):A818, April 2005.

[76] W. Waag, C. Fleischer, and D. U. Sauer. Critical Review of the Methods for Monitoring of Lithium-Ion Batteries in Electric and Hybrid Vehicles. *Journal of Power Sources*, 258:321–339, July 2014.

[77] Z. Cai, G. Liu, and J. Luo. Research State of Charge Estimation Tactics of Nickel-Hydrogen Battery. In *2010 International Symposium on Intelligence Information Processing and Trusted Computing*, pages 184–187. IEEE, October 2010.

[78] B. Pattipati, C. Sankavaram, and K. Pattipati. System Identification and Estimation Framework for Pivotal Automotive Battery Management System Characteristics. *IEEE Transactions on Systems, Man, and Cybernetics, Part C (Applications and Reviews)*, 41(6):869–884, November 2011.

[79] N. Watrin, B. Blunier, and A. Miraoui. Review of Adaptive Systems for Lithium Batteries State-of-Charge and State-of-Health Estimation. In *2012 IEEE Transportation Electrification Conference and Expo (ITEC)*, pages 1–6. IEEE, June 2012.

[80] K. Malinowski. *State of Charge Estimation for Advanced Batteries: Reduced Order Electrochemical Modeling with Error Compensation*. Phd thesis, Auburn University, November 2011.

[81] V. Prajapati, H. Hess, E. J. William, V. Gupta, M. Huff, M. Manic, F. Rufus, A. Thakker, and J. Govar. A Literature Review of State of-Charge Estimation Techniques Applicable to Lithium Poly-Carbon Monoflouride (LI/CFx) Battery. In *India International Conference on Power Electronics 2010 (IICPE2010)*, pages 1–8. IEEE, January 2011.

[82] Y. Zhu, H. Hu, G. Xu, and Z. Zhao. Hardware-in-the-Loop Simulation of Pure Electric Vehicle Control System. In *2009 International Asia Conference on Informatics in Control, Automation and Robotics*, pages 254–258. IEEE, February 2009.

[83] L. Maharjan, S. Inoue, H. Akagi, and J. Asakura. State-of-Charge (SOC)-Balancing Control of a Battery Energy Storage System Based on a Cascade PWM Converter. *IEEE Transactions on Power Electronics*, 24(6):1628–1636, June 2009.

[84] H. Dai, X. Wei, Z. Sun, J. Wang, and W. Gu. Online Cell SOC Estimation of Li-Ion Battery Packs Using a Dual Time-Scale Kalman Filtering for EV Applications. *Applied Energy*, 95:227–237, March 2012.

[85] A. Affanni, A. Bellini, G. Franceschini, P. Guglielmi, and C. Tassoni. Battery Choice and Management for New-Generation Electric Vehicles. *IEEE Transactions on Industrial Electronics*, 52(5):1343–1349, October 2005.

[86] K. Muramatsu. Battery Condition Monitor and Monitoring Method, July 1987.

[87] E. Yehuda, E. Peled, Y. Herzel, I. Reshef, D. Kelrich, and S. Rozen. Method and Apparatus for Determining the State-of-Charge of Batteries Particularly Lithium Batteries, February 1988.

[88] U. Kopmann. Method and Apparatus for Monitoring the State of Charge of a Battery. *US Patent 5,488,300*, 1996.

[89] V. Pop, H. J. Bergveld, P. H. L. Notten, and P. P. L. Regtien. State-of-the-Art of Battery State-of-Charge Determination. *Measurement Science and Technology*, 16(12):R93–R110, December 2005.

[90] M. Verbrugge and E. Tate. Adaptive State of Charge Algorithm for Nickel Metal Hydride Batteries Including Hysteresis Phenomena. *Journal of Power Sources*, 126(1-2):236–249, 2004.

[91] S. Drouilhet and B. L. Johnson. A Battery Life Prediction Method for Hybrid Power Applications. Technical report, National Renewable Energy Laboratory, Reno, Nevada, 1997.

[92] Y. Yamada, T. Sasaki, N. Tatsuda, D. Weingarth, K. Yano, and R. Kötz. A Novel Model Electrode for Investigating Ion Transport Inside Pores in an Electrical Double-Layer Capacitor: Monodispered Microporous Starburst Carbon Spheres. *Electrochimica Acta*, 81:138–148, October 2012.

[93] Y. H. Chiang and W. Y. Sean. Dynamical Estimation of State-of-Health of Batteries by Using Adaptive Observer. In *2nd International Conference on Power Electronics and Intelligent Transportation Systems*, pages 110–115, 2009.

[94] R. K. Jaworski. Effects of Nonlinearity of Arrhenius Equation on Predictions of Time to Failure for Batteries Exposed to Fluctuating Temperatures. In *INTELEC - Twentieth International Telecommunications Energy Conference (Cat. No.98CH36263)*, pages 289–296. IEEE, 1998.

[95] S. Piller, M. Perrin, and A. Jossen. Methods for State-of-Charge Determination and their Applications. *Journal of Power Sources*, 96(1):113–120, June 2001.

[96] V. Pop, H. J. Bergveld, J. H. G. Op het Veld, P. P. L. Regtien, D. Danilov, and P. H. L. Notten. Modeling Battery Behavior for Accurate State-of-Charge Indication. *Journal of The Electrochemical Society*, 153(11):A2013, November 2006.

[97] V. Pop, H. J. Bergveld, P. H. L. Notten, J. H. G. Op het Veld, and P. P. L. Regtien. Accuracy Analysis of the State-of-Charge and Remaining Run-Time Determination for Lithium-Ion Batteries. *Measurement*, 42(8):1131–1138, 2009.

[98] M. Doyle. Modeling of Galvanostatic Charge and Discharge of the Lithium/Polymer/Insertion Cell. *Journal of The Electrochemical Society*, 140(6):1526, June 1993.

[99] J. Newman and K. E. Thomas-Alyea. *Electrochemical Systems*. Wiley & Sons, New York; USA, 3 edition, 2004.

[100] P. M. Gomadam, J. W. Weidner, R. A. Dougal, and R .E. White. Mathematical Modeling of Lithium-Ion and Nickel Battery Systems. *Journal of Power Sources*, 110(2):267–284, August 2002.

[101] M. Doyle. Comparison of Modeling Predictions with Experimental Data from Plastic Lithium Ion Cells. *Journal of The Electrochemical Society*, 143(6):1890, June 1996.

[102] C. R. Pals. Thermal Modeling of the Lithium/Polymer Battery. *Journal of The Electrochemical Society*, 142(10):3274, October 1995.

[103] L. Song and J. W. Evans. Electrochemical-Thermal Model of Lithium Polymer Batteries. *Journal of The Electrochemical Society*, 147(6):2086, June 2000.

[104] W. B. Gu and C. Y. Wang. Thermal-Electrochemical Modeling of Battery Systems. *Journal of The Electrochemical Society*, 147(8):2910, August 2000.

[105] T. F. Fuller. Simulation and Optimization of the Dual Lithium Ion Insertion Cell. *Journal of The Electrochemical Society*, 141(1):1, January 1994.

[106] T. F. Fuller, M. Doyle, and J. Newman. Relaxation Phenomena in Lithium-Ion-Insertion Cells. *Journal of The Electrochemical Society*, 141(4):982–990, April 1994.

[107] V. R. Subramanian, V. D. Diwakar, and D. Tapriyal. Efficient Macro-Micro Scale Coupled Modeling of Batteries. *Journal of The Electrochemical Society*, 152(10):A2002, 2005.

[108] T. S. Dao, C. P. Vyasarayani, and J. McPhee. Simplification and Order Reduction of Lithium-Ion Battery Model Based on Porous-Electrode Theory. *Journal of Power Sources*, 198:329–337, January 2012.

[109] B. S. Haran, B. N. Popov, and R. E. White. Determination of the Hydrogen Diffusion Coefficient in Metal Hydrides by Impedance Spectroscopy. *Journal of Power Sources*, 75(1):56–63, September 1998.

[110] S. Santhanagopalan, Q. Guo, P. Ramadass, and R. E. White. Review of Models for Predicting the Cycling Performance of Lithium Ion Batteries. *Journal of Power Sources*, 156(2):620–628, June 2006.

[111] W. Peukert. Über die Abhängigkeit der Kapazität von der Entladestromstärke bei Bleiakkumulatoren. *Elektrotechnische Zeitschrift*, 18(1):287–288, 1897.

[112] C. C. Chan, E. W. C. Lo, and S. Weixiang. The Available Capacity Computation Model based on Artificial Neural Network for Lead-Acid Batteries in Electric Vehicles. *Journal of Power Sources*, 87(1-2):201–204, April 2000.

[113] D. Doerffel and S. A. Sharkh. A Critical Review of using the Peukert Equation for Determining the Remaining Capacity of Lead-Acid and Lithium-Ion Batteries. *Journal of Power Sources*, 155(2):395–400, April 2006.

[114] G. Wu, R. Lu, C. Zhu, and C. C. Chan. Apply a Piece-wise Peukert's Equation with Temperature Correction Factor to NiMH Battery State of Charge Estimation. *Journal of Asian Electric Vehicles*, 8(2):1419–1423, January 2010.

[115] H. He, X. Zhang, R. Xiong, Y. Xu, and H. Guo. Online Model-based Estimation of State-of-Charge and Open-circuit Voltage of Lithium-Ion Batteries in Electric Vehicles. *Energy*, 39(1):310–318, March 2012.

[116] S. Cho, H. Jeong, C. Han, S. Jin, J. H. Lim, and J. Oh. State-of-Charge Estimation for Lithium-Ion Batteries under Various Operating Conditions using an Equivalent Circuit Model. *Computers & Chemical Engineering*, 41:1–9, June 2012.

[117] G. L. Plett. Extended Kalman Filtering for Battery Management Systems of LiPB-based HEV Battery Packs Part 1. Background. *Journal of Power Sources*, 134(2):252–261, 2004.

[118] H. L. N. Wiegman. *Battery State Estimation and Control for Power Buffering Applications*. University of Wisconsin–Madison, 1999.

[119] K. Kurohane, A. Uehara, T. Senjyu, A. Yona, N. Urasaki, T. Funabashi, and C. H. Kim. Control Strategy for a Distributed DC Power System with Renewable Energy. *Renewable Energy*, 36(1):42–49, 2011.

[120] K. Bandara, T. Sweet, and J. Ekanayake. Photovoltaic Applications for Off-Grid Electrification using Novel Multi-Level Inverter Technology with Energy Storage. *Renewable Energy*, 37(1):82–88, 2012.

[121] A. Tofighi and M. Kalantar. Power Management of PV/Battery Hybrid Power Source via Passivity-Based Control. *Renewable Energy*, 36(9):2440–2450, 2011.

[122] C. Weng, J. Sun, and H. Pen. A Unified Open-Circuit-Voltage Model of Lithium-Ion Batteries for State-of-Charge Estimation and State-of-Health Monitoring. *Journal of Power Sources*, 258:228–237, July 2014.

[123] M. Chen and G. A. Rincon-Mora. Accurate Electrical Battery Model Capable of Predicting Runtime and I-V Performance. *IEEE Transactions on Energy Conversion*, 21(2):504–511, June 2006.

[124] Y. Hu, S. Yurkovich, Y. Guezennec, and B.J. Yurkovich. Electro-Thermal Battery Model Identification for Automotive Applications. *Journal of Power Sources*, 196(1):449–457, January 2011.

[125] G. L. Plett. Extended Kalman Filtering for Battery Management Systems of LiPB-based HEV Battery Packs Part 3. State and Parameter Estimation. *Journal of Power Sources*, 134(2):277–292, 2004.

[126] A. Szumanowski. Battery Management System Based on Battery Nonlinear Dynamics Modeling. *IEEE Transactions on Vehicular Technology*, 57(3):1425–1432, May 2008.

[127] Maxim Integrated Products Inc. Inaccuracies of Estimating Remaining Cell Capacity with Voltage Measurements Alone - Application Note. Technical report, 2002.

[128] V. Pop, H. J. Bergveld, P. P. L. Regtien, J. H. G. Op het Veld, D. Danilov, and P. H. L. Notten. Battery Aging and Its Influence on the Electromotive Force. *Journal of The Electrochemical Society*, 154(8):A744, August 2007.

[129] C. Unterrieder, M. Lunglmayr, S. Marsili, and M. Huemer. Computer-Aided Optimization for Predictive Battery State-of-Charge Determination. *Computer Aided Systems Theory - EUROCASY 2013*, 8111:476–482, 2013.

[130] C. Unterrieder, M. Lunglmayr, S. Marsili, and M. Huemer. Battery State-of-Charge Estimation Prototype using EMF Voltage Prediction. In *Circuits and Systems (ISCAS), 2014 IEEE International Symposium*, pages 622–625, 2014.

[131] M. Coleman and W.G. Hurley. State-of-Charge Determination From EMF Voltage Estimation: Using Impedance, Terminal Voltage and Current for Lead-Acid and Lithium-Ion Batteries. *IEEE Transactions on Industrial Electronics*, 54(5):2550–2557, October 2007.

[132] K. S. Ng, C. S. Moo, Y. P. Chen, and Y. C. Hsieh. Enhanced Coulomb Counting Method for Estimating State-of-Charge and State-of-Health of Lithium-Ion Batteries. *Applied Energy*, 86(9):1506–1511, September 2009.

[133] S. A. Ilangovan and S. Sathyanarayana. Impedance Parameters of Individual Electrodes and Internal Resistance of Sealed Batteries by a New Non-destructive Technique. *Journal of Applied Electrochemistry*, 22(5):456–463, May 1992.

[134] S. C. Hageman. "Simple PSpice Models let you Simulate Common Battery Types". *Electronic Design News*, pages 17 – 129, 1993.

[135] S. Hageman. PSpice Models Nickel-Metal-Hydride Cells, February 1995.

[136] G. Hunt and C. Motloch. PNGV Battery Test Manual. Technical report, U.S. Department of Energy, Idaho, 2001.

[137] V. H. Johnson, A. Pesaran, and T. Sack. Temperature-Dependent Battery Models for High-Power Lithium-lon Batteries. In *Annual Electric Vehicle Symposium*, number January, page 14, Montreal, Canada, 2000. National Renewable Energy Laboratory, Saft America.

[138] V. H. Johnson. Battery Performance Models in ADVISOR. *Journal of Power Sources*, 110:321–329, 2002.

[139] S. Raël and M. Hinaje. Using Electrical Analogy to Describe Mass and Charge Transport in Lithium-Ion batteries. *Journal of Power Sources*, 222:112–122, January 2013.

[140] E. Prada, D. Di Domenico, Y. Creff, J. Bernard, V. Sauvant-Moynot, and F. Huet. Simplified Electrochemical and Thermal Model of LiFePO4-Graphite Li-Ion Batteries for Fast Charge Applications. *Journal of the Electrochemical Society*, 159(9):A1508–A1519, August 2012.

[141] E. Prada, D. Di Domenico, Y. Creff, J. Bernard, V. Sauvant-Moynot, and F. Huet. A Simplified Electrochemical and Thermal Aging Model of LiFePO4-Graphite Li-ion Batteries: Power and Capacity Fade Simulations. *Journal of the Electrochemical Society*, 160(4):A616–A628, February 2013.

[142] K. Smith and C. Y. Wang. Solid-State Diffusion Limitations on Pulse Operation of a Lithium Ion Cell for Hybrid Electric Vehicles. *Journal of Power Sources*, 161(1):628–639, 2006.

[143] J. Kim and B. H. Cho. State-of-Charge Estimation and State-of-Health Prediction of a Li-Ion Degraded Battery Based on an EKF Combined With a Per-Unit System. *IEEE Transactions on Vehicular Technology*, 60(9):4249–4260, November 2011.

[144] J. Wang, B. Cao, Q. Chen, and F. Wang. Combined State of Charge Estimator for Electric Vehicle Battery Pack. *Control Engineering Practice*, 15(12):1569–1576, December 2007.

[145] G. Olivier, J. N. Patillon, and F. D'Alché-Buc. Neural Network Adaptive Modeling of Battery Discharge Behavior. *Proc. 7th Int. Conf. on Artificial Neural Networks (ICANN)*, 1327:541–546, 1997.

[146] A. J. Salkind, C. Fennie, P. Singh, T. Atwater, and D. E. Reisner. Determination of State-of-Charge and State-of-Health of Batteries by Fuzzy Logic Methodology. *Journal of Power Sources*, 80(1-2):293–300, July 1999.

[147] L. Bowen, R. Zarr, and S. Denton. A Microcontroller-Based Intelligent Battery System. *IEEE Aerospace and Electronic Systems Magazine*, 9(5):16–19, May 1994.

[148] E. P. Finger. Quiescent Voltage Sampling Battery State of Charge Meter, July 1984.

[149] Y. Tanjo, T. Nakagawa, H. Horie, T. Abe, K. Iwai, and M. Kawai. State of Charge Indicator. Technical report, October 2000.

[150] G. L. Plett. Extended Kalman Filtering for Battery Management Systems of LiPB-based HEV Battery Packs Part 2. Modeling and Identification. *Journal of Power Sources*, 134(2):262–276, 2004.

[151] G. L. Plett. Recursive Approximate Weighted Total Least Squares Estimation of Battery Cell Total Capacity. *Journal of Power Sources*, 196(4):2319–2331, 2011.

[152] D. U. Sauer and H. Wenzl. Comparison of Different Approaches for Lifetime Prediction of Electrochemical Systems-Using Lead-Acid Batteries as Example. *Journal of Power Sources*, 176(2):534–546, February 2008.

[153] S. W. Eom, M. K. Kim, I. J. Kim, S. I. Moon, Y. K. Sun, and H. S. Kim. Life Prediction and Reliability Assessment of Lithium Secondary Batteries. *Journal of Power Sources*, 174(2):954–958, December 2007.

[154] L. Serrao, Z. Chehab, Y. Guezennec, and G. Rizzoni. An Aging Model of Ni-MH Batteries for Hybrid Electric Vehicles. In *2005 IEEE Vehicle Power and Propulsion Conference*, pages 78–85. IEEE, 2005.

[155] R. B. Wright, J. P. Christophersen, C. G. Motloch, J. R. Belt, C. D. Ho, V. S Battaglia, J. A. Barnes, T. Q. Duong, and R. A. Sutula. Power Fade and Capacity Fade Resulting from Cycle-Life Testing of Advanced Technology Development Program Lithium-Ion Batteries. *Journal of Power Sources*, 119-121:865–869, June 2003.

[156] P. Singh, R. Vinjamuri, X. Wang, and D. Reisner. Fuzzy Logic Modeling of EIS Measurements on Lithium-Ion Batteries. *Electrochimica Acta*, 51(8-9):1673–1679, January 2006.

[157] P. Singh, R. Vinjamuri, X. Wang, and D. Reisner. Design and Implementation of a Fuzzy Logic-Based State-of-Charge Meter for Li-ion Batteries used in Portable Defibrillators. *Journal of Power Sources*, 162(2):829–836, November 2006.

[158] P. Ramadass, B. Haran, R. White, and B. N. Popov. Mathematical modeling of the capacity fade of Li-ion cells. *Journal of Power Sources*, 123(2):230–240, 2003.

[159] B. S. Bhangu, P. Bentley, D. A. Stone, and C. M. Bingham. Nonlinear Observers for Predicting State-of-Charge and State-of-Health of Lead-Acid Batteries for Hybrid-Electric Vehicles. *IEEE Transactions on Vehicular Technology*, 54(3):783–794, May 2005.

[160] C. Forgez, K. El Kadri Benkara, and G. Friedrich. Impedance Observer for a Li-Ion Battery Using Kalman Filter. *IEEE Transactions on Vehicular Technology*, 58(8):3930–3937, October 2009.

[161] W. Y. Chang. The State of Charge Estimating Methods for Battery: A Review. *ISRN Applied Mathematics*, 2013:7, 2013.

[162] E. Barsoukov and J. R. Macdonald. *Impedance Spectroscopy: Theory, Experiment, and Applications*. Wiley & Sons, New York, USA, 2005.

[163] P. Debye and E. Huckel. The Theory of Electrolytes I. The Lowering of the Freezing Point and Related Occurrences. *Physikalische Zeitschrift*, 24(1):206, January 1923.

[164] R. E. White, J. O. Bockris, and B. E. Conway. *Modern Aspects of Electrochemistry*. Springer US, Boston, MA, 1983.

[165] M. Doyle and Y. Fuentes. Computer Simulations of a Lithium-Ion Polymer Battery and Implications for Higher Capacity Next-Generation Battery Designs. *Journal of The Electrochemical Society*, 150(6):A706, June 2003.

[166] T. Ohzuku. Phenomenological Expression of Solid-State Redox Potentials of Li-CoO2, LiCoNiO2, and LiNiO2 Insertion Electrodes. *Journal of The Electrochemical Society*, 144(8):2780, August 1997.

[167] B. Wu, V. Yufit, Y. Merla, R. F. Martinez-Botas, N. P. Brandon, and G. J. Offer. Differential Thermal Voltammetry for Tracking of Degradation in Lithium-Ion Batteries. *Journal of Power Sources*, 273:495–501, January 2015.

[168] K. Smith and C. Y. Wang. Power and Thermal Characterization of a Lithium-Ion Battery Pack for Hybrid-Electric Vehicles. *Journal of Power Sources*, 160(1):662–673, September 2006.

[169] T. Reddy. *Linden's Handbook of Batteries*. McGraw-Hill professional, New York, USA, 4 edition, 2010.

[170] H. Helmholtz. Über einige Gesetze der Verteilung Elektrischer Ströme in Körperlichen Leitern mit Anwendung auf die Tierisch-Elektrischen Versuche. *Annalen der Physik und Chemie*, 165(6):211–233, 1853.

[171] M. Gouy. Sur la Constitution de la Charge Electrique à la Surface d'un Electrolyte. *Journal de Physique Théorique et Appliquée*, 9(1):457–468, 1910.

[172] K. B. Oldham. A Gouy-Chapman-Stern Model of the Double Layer at a (Metal) (Ionic Liquid) Interface. *Journal of Electroanalytical Chemistry*, 613(2):131–138, February 2008.

[173] O. Stern. Zur Theorie der Elektrolytischen Doppelschicht. *Zeitschrift für Elektrochemie und angewandte physikalische Chemie*, 30(21):508–516, November 1924.

[174] J. Newman and K. E. Thomas-Alyea. *Electrochemical Systems*. Wiley & Sons, New York, New York, USA, 3 edition, 2004.

[175] G. Ning and B. N. Popov. Cycle Life Modeling of Lithium-Ion Batteries. *Journal of The Electrochemical Society*, 151(10):A1584, October 2004.

[176] G. Ning, R. E. White, and B. N. Popov. A Generalized Cycle Life Model of Rechargeable LiIon Batteries. *Electrochimica Acta*, 51(10):2012–2022, February 2006.

[177] A. A. Kornyshev. Double-Layer in Ionic Liquids: Paradigm Change? *The journal of physical chemistry. B*, 111(20):5545–57, May 2007.

[178] A. Fick. Ueber Diffusion. *Annalen der Physik und Chemie*, 170(1):59–86, 1855.

[179] J. Horno, M. T. García-Hernández, and C. F. González-Fernández. Digital Simulation of Electrochemical Processes by the Network Approach. *Journal of Electroanalytical Chemistry*, 352(1-2):83–97, June 1993.

[180] B. Scrosati and J. Garche. Lithium Batteries: Status, Prospects and Future. *Journal of Power Sources*, 195(9):2419–2430, May 2010.

[181] M. Doyle. Modeling of Galvanostatic Charge and Discharge of the Lithium/Polymer/Insertion Cell. *Journal of The Electrochemical Society*, 140(6):1526, June 1993.

[182] R. Painter, S. Berryhill, L. Sharpe, and S. K. Hargrove. A Single Particle Thermal Model for Lithium Ion Batteries. Technical report, Tennessee State University, Nashville, TN, USA, 2014.

[183] L. Cai and R. E. White. Mathematical Modeling of a Lithium Ion Battery with Thermal Effects in COMSOL Inc. Multiphysics (MP) Software. *Journal of Power Sources*, 196(14):5985–5989, July 2011.

[184] K. Smith and C. Y. Wang. Power and Thermal Characterization of a Lithium-Ion Battery Pack for Hybrid-Electric Vehicles. *Journal of Power Sources*, 160(1):662–673, September 2006.

[185] K. A. Smith, C. D. Rahn, and C. Y. Wang. Control Oriented 1D Electrochemical Model of Lithium-Ion Battery. *Energy Conversion and Management*, 48(9):2565–2578, 2007.

[186] J. C. Forman, S. J. Moura, J. L. Stein, and H. K. Fathy. Genetic Parameter Identification of the Doyle-Fuller-Newman Model from Experimental Cycling of a LiFePO 4 Battery. 2010.

[187] D. Zhang, B. S. Haran, A. Durairajan, R. E. White, Y. Podrazhansky, and B. N. Popov. Studies on Capacity Fade of Lithium-IonBatteries. *Journal of Power Sources*, 91(2):122–129, December 2000.

[188] O. Borodin, G. D. Smith, and P. Fan. Molecular Dynamics Simulations of Lithium Alkyl Carbonates. *The journal of physical chemistry. B*, 110(45):22773–9, November 2006.

[189] J. M. Marcicki. *Modeling, Parametrization, and Diagnostics for Lithium-Ion Batteries with Automotive Applications*. Phd thesis, The Ohio State University, 2012.

[190] G. J. Offer, V. Yufit, D. A. Howey, B. Wu, and N. P. Brandon. Module Design and Fault Diagnosis in Electric Vehicle Batteries. *Journal of Power Sources*, 206:383–392, May 2012.

[191] B. Wu. *Fuel Cell Hybrid Electric Vehicle Powertrain Modelling and Testing*. Phd thesis, Imperial College London, 2014.

[192] S.C. Chen, C.C. Wan, and Y.Y. Wang. Thermal analysis of lithium-ion batteries. *Journal of Power Sources*, 140(1):111–124, January 2005.

[193] M. Itagaki, N. Kobari, S. Yotsuda, K. Watanabe, S. Kinoshita, and M. Ue. In-situ Electrochemical Impedance Spectroscopy to Investigate Negative Electrode of Lithium-Ion Rechargeable Batteries. *Journal of Power Sources*, 135(1-2):255–261, September 2004.

[194] D. Andre, M. Meiler, K. Steiner, H. Walz, T. Soczka-Guth, and D. U. Sauer. Characterization of High-Power Lithium-Ion Batteries by Electrochemical Impedance Spectroscopy II: Modelling. *Journal of Power Sources*, 196(12):5349–5356, June 2011.

[195] H. He, R. Xiong, and J. Fan. Evaluation of Lithium-Ion Battery Equivalent Circuit Models for State of Charge Estimation by an Experimental Approach. *Energies*, 4(12):582–598, March 2011.

[196] A. Rahmoun, H. Biechl, and A. Rosin. Evaluation of Equivalent Circuit Diagrams and Transfer Functions for Modeling of Lithium-Ion Batteries. *Electrical, Control and Communication Engineering*, 2(1):34–39, January 2013.

[197] J. H. Lee and W. J. Choi. Novel State-of-Charge Estimation Method for Lithium Polymer Batteries Using Electrochemical Impedance Spectroscopy. *Journal of Power Electronics*, 11(2):237–243, 2011.

[198] Y. Troxler, B. Wu, M. Marinescu, V. Yufit, Y. Patel, A. J. Marquis, N. P. Brandon, and G. J. Offer. The Effect of Thermal Gradients on the Performance of Lithium-Ion Batteries. *Journal of Power Sources*, 247:1018–1025, 2014.

[199] M.-T. von Srbik, B. Cussons, R. F. Martinez-Botas, and L. Lytton. The 2012 RAC Future Car Challenge: The Impact of Hybridisation on Energy Consumption. In *Hybrid and Electric Vehicles Conference 2013 (HEVC 2013)*, pages 8.1–8.1. Institution of Engineering and Technology, 2013.